TABLE OF CONTENTS

LIST OF FIGURES

LIST OF TABLES

CHAPTER 1

DEFINING THE PROBLEM

CHAPTER 1

DEFINING THE PROBLEM

1.1 INTODUCTION

Alloys are materials having metallic properties and are composed of two or more elements, at least one of which is a metal. In the case of aluminum alloys, most of them contain 90 to 96% aluminum. Aluminum alloys are divided into two categories, wrought alloys and cast alloys. Aluminum casting alloys are used in a large number of applications including automobiles, trucks, transmission of electricity, development of transportation infrastructures, and in the aerospace and defence industries. The fast growth of aluminum alloys in industrial applications is related to their high strength-to-weight ratio which improves the mechanical properties and performance of the products. Among different foundry alloys, aluminum casting alloys are very popular, as they have the highest castability ratings, possess good fluidity and comparably low melting points. Their light weight and high strength-to-weight ratio are the main reasons why cast iron and steel components are being increasingly replaced by aluminum alloys, particularly in the automotive industry. Choosing one casting alloy over another tends to be determined by the

relative ability of the alloy to meet one or more of the characteristics required for a specific application.[1-7]

The important alloying elements used to impart particular properties to aluminum are silicon, magnesium, manganese, copper and zinc. Silicon imparts good fluidity to the alloy. Magnesium, copper and zinc are hardening elements which strengthen the alloy following heat treatment through precipitation or age hardening. Manganese is used to control the type of iron phases formed in the alloy. Iron may be viewed as an impurity in the metal, where the source of the iron depends on the raw materials (alumina) and the electrolytic reduction process from which the aluminum is obtained. Most commercial alloys contain 0.1-0.4 percent iron by weight. Iron is occasionally used to give the material special qualities. For example, in the case of die casting alloys, iron is added to reduce die soldering. Other alloying elements used in combination with one or more of the major alloying elements include bismuth, boron, chromium, lead, nickel, titanium and zirconium. These elements are usually used in very small amounts (<0.1 percent by weight), although B, Pb and Cr levels may go up to 0.5 percent, in special cases, to enhance properties such as castability, machinability, heat- and corrosion-resistance, and tensile strength.[8]

Over the years, aluminum-copper (Al-Cu) cast alloys have been increasingly investigated, the reason being that copper has a significant impact on the strength and hardness of aluminum castings at both ambient and elevated service temperatures. Due to the presence of copper, the mechanical properties of these alloys may be improved via age hardening through the formation of Al_2Cu precipitates following aging treatment. Copper

also improves the machinability of such alloys by increasing the matrix hardness, making it easier to generate small cutting chips and fine machined finishes.

Alloying elements additions are used to enhance the structure and mechanical properties of aluminum casting alloys. Strontium (Sr) is added to Al casting alloys containing Si to modify the morphology of the Si particles, from coarse, brittle flakes to a finer spherical form. Also, the absorption of Sr by iron intermetallics, results in refining their morphology.[9-11] Titanium is added either individually or in combination with boron to refine the grain structure of the α-Al matrix, as it creates many nuclei in the melt, which encourages the formation of small equiaxed grains of α-Al, rather than the coarse, columnar grain structure that is produced in the absence of grain refinement. One of the important additions used in Al-Cu alloys, silver (Ag), is added to Al-Cu alloys to improve the alloy strength. Silver forms atom clusters with Mg that act as nucleation sites for the Ω-phase showing a composition of Al_2Cu.[12-14] Zirconium is used as a grain refiner, and additions of Zr and Sc to Al alloys have been reported to preserve the mechanical properties of the alloy at high temperature, where the precipitation of Al_3Zr and Al_3Sc dispersoids in the structure provides the means to maintain the strength at elevated temperatures.[15-16]

In this study, the hardness and tensile properties of an Al-2%Cu based alloy were investigated. This alloy was selected for study based on its promising potential for use in automotive applications. Coded alloy 220, and with a composition of Al-2%Cu-1.32%Si-0.425Mg-0.58%Fe-0.59%Mn-0.07%Ti, this base alloy was used to prepare other alloys by adding Sr, Ti, Zr, Ag, and Sc to the melt, individually or in different combinations.

Castings were made using the low-pressure die casting (LPDC) technique which provides several advantages, among them high productivity and reduced machining costs. The LPDC test bars were used for hardness and tensile testing.

1.2 OBJECTIVES

The present study was undertaken to investigate and understand the effects of alloying elements on the mechanical properties of Al-2%Cu based alloys produced by the low pressure die casting technique. This was accomplished by addressing the following objectives:

1- Examine select alloy microstructures of the various alloys prepared to determine the phases and precipitates obtained in the as-cast condition.

2- Determine the tensile properties in relation to the effects of alloying additions.

3- Analyze the data obtained in terms of the effects of alloying additions and heat treatment parameters on the UTS, YS and %El values, employing mathematical analysis.

4- Use the quality index to evaluate the quality of the alloys corresponding to the alloying element additions.

CHAPTER 2

SURVEY OF THE LITERATURE

CHAPTER 2

SURVEY OF THE LITERATURE

2.1 CAST ALUMINUM ALLOYS

Cast aluminum alloys are grouped into nine different series of alloys, namely, 1xx.x series, 2xx.x series, 3xx.x series, and so on. The principal alloying element or elements in each series characterizes that series, as shown in Table 2.1. [17]

The designation system is based on three digits to the left of the decimal point and one to the right. The first digit indicates the principal alloying element. The second and third digits are arbitrary numbers given to identify a specific alloy in the series. The number following the decimal point indicates whether the alloy is a casting (0) or an ingot (1or 2). A capital letter prefix indicates a modification to a specific alloy. Thus an Al-Cu alloy would belong to the 2xxx.x series, whereas an alloy containing Al-Si-Mg or Al-Si-Cu, or Al-Si-Cu-Mg would belong to the 3xxx.x series, as for example, the alloys 319, A319.2, B319.2, etc.[18-19]

Table 2.1 Cast aluminum alloy designation system.[17]

Alloy Series	Principal Alloying Element
1xx.x	Aluminum (99.000% minimum)
2xx.x	Copper
3xx.x	Silicon plus Copper and/or magnesium
4xx.x	Silicon
5xx.x	Magnesium
6xx.x	Unused series
7xx.x	Zinc
8xx.x	Tin
9xx.x	Other elements

Cast Al-Cu Alloys

Copper (Cu) has the single greatest impact of all alloying elements on the strength and hardness of aluminum casting alloys, in both as-cast and heat-treated conditions, and at ambient and elevated service temperatures. Copper improves the machinability of aluminum alloys by increasing the matrix hardness, making it easier to generate small cutting chips and fine machined finishes. On the downside, copper generally reduces the corrosion resistance of aluminum and, in certain alloys and tempers, it increases the stress corrosion susceptibility. Copper is generally used to increase the tensile strength and hardness through heat treatment. It also reduces the resistance to corrosion and hot cracking, or hot tearing.

A variety of alloys with copper as the major addition were developed.[21-22] Most of these alloys fall within one of the following groups:

- Cast alloys with 5% Cu, often with small amounts of silicon and magnesium.
- Cast alloys with 7-8% Cu, which often contain large amounts of iron and silicon and appreciable amounts of manganese, chromium, zinc, tin, etc.
- Cast alloys with 10-14% Cu. These alloys may contain small amounts of magnesium (0.1-0.3%), iron up to 1.5%, up to 5% Si and smaller amounts of nickel, manganese, chromium.
- Wrought alloys with 5-6% Cu and often small amounts of manganese, silicon, cadmium, bismuth, tin, lithium, vanadium and zirconium. Alloys of this type containing lead, bismuth, and cadmium exhibit superior machinability.
- Dural also called duraluminum (considered as one of the earliest types of age-hardenable aluminium alloys), main alloying constituents are copper, manganese, and magnesium, and sometimes with a low-silicon content which is typically less than 12%.[19-21]
- Copper alloys containing nickel, which can be subdivided in two groups: the *Y* alloy type, whose basic composition is 4% Cu, 2% Ni, 1.5% Mg; and the *Hyduminiums*, which usually have lower copper contents and in which iron replaces 30me of the nickel.[22]

In most of the alloys in this group, aluminum is the primary constituent and in the cast alloys the basic structure consists of cored dendrites of aluminum solid solution, with a variety of constituents at the grain boundaries or in the interdendritic spaces, forming a brittle, more or less continuous network of eutectics. Copper forms $(CuFe)Al_6$ and Cu_2FeA_{l7} with iron, and $(CuFeMn)Al_6$ and $Cu_2Mn_3Al_{20}$ with manganese. The amount of

silicon available to some extent controls the copper compounds formed. Silicon above 1% favors the formation of $FeSiAl_5$ phase, over the iron-copper compounds and $(CuFeMn)_3Si_2Al_{15}$. Similarly, but to a lesser extent, the available silicon is affected by iron and manganese contents. With the Cu:Mg ratio below 2 and the Mg:Si ratio well above 1.7 the $CuMg_4Al_6$compound is formed, especially if appreciable zinc is present. When Cu:Mg > 2 and Mg:Si > 1.7, $CuMgAl_2$ is formed. If the Mg:Si ratio is approximately 1.7, Mg_2Si and $CuAl_2$ are in equilibrium. With the Mg:Si ratio 1 or less, $Cu_2Mg_8Si_6Al_5$, is formed, usually together with$CuAl_2$. When the copper exceeds 5%, commercial heat treatment cannot dissolve it and the network of eutectics does not break up. Thus, in the 10-15% Cu alloys there is little difference in structure between the as-cast and heat treated alloys. Magnesium can combine with silicon and copper. When appreciable amounts of lead, bismuth or tin are present, Mg_2Sn, Mg_2Pb, Mg_2Bi_3 can be formed. Aluminum-copper alloys that do not also contain at least moderate amounts of silicon have relatively poor fluidity and resistance to hot tearing during solidification. The binary phase diagram for the Al-Cu system is shown below in Figure 2.1.[20] Adding Cu lowers the melting point of aluminum at the eutectic temperature, reaching maximum solid solubility in the binary alloy.[21-23]

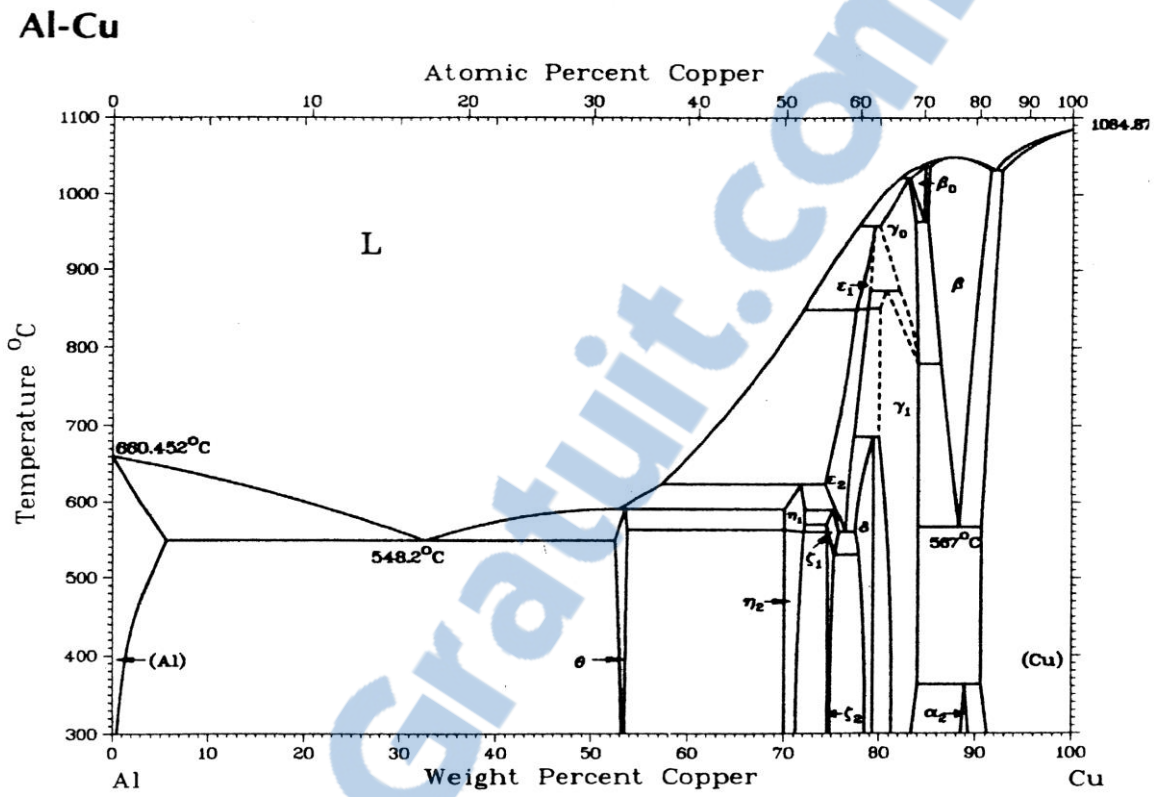

Figure 2.1 Al-Cu binary phase diagram.[20]

Some alloys may improve their strength and hardness by the formation of uniformly small dispersed particles within the original matrix when the solidified alloy is subjected to heat treatment. These particles are said to be second-phase particles, and the strengthening achieved through the precipitation of these particles is known as "*precipitation* (or *age*) *hardening*". These precipitates strengthen the heat-treated alloys by blocking the movement of dislocations. Al-Cu alloys are suitable for casting, as these alloys are heat treatable, that is, they can be age hardened. Figure 2.2 summarizes the range of temperatures used for the different stages in the heat treatment of aluminum-copper alloys.[24-25]

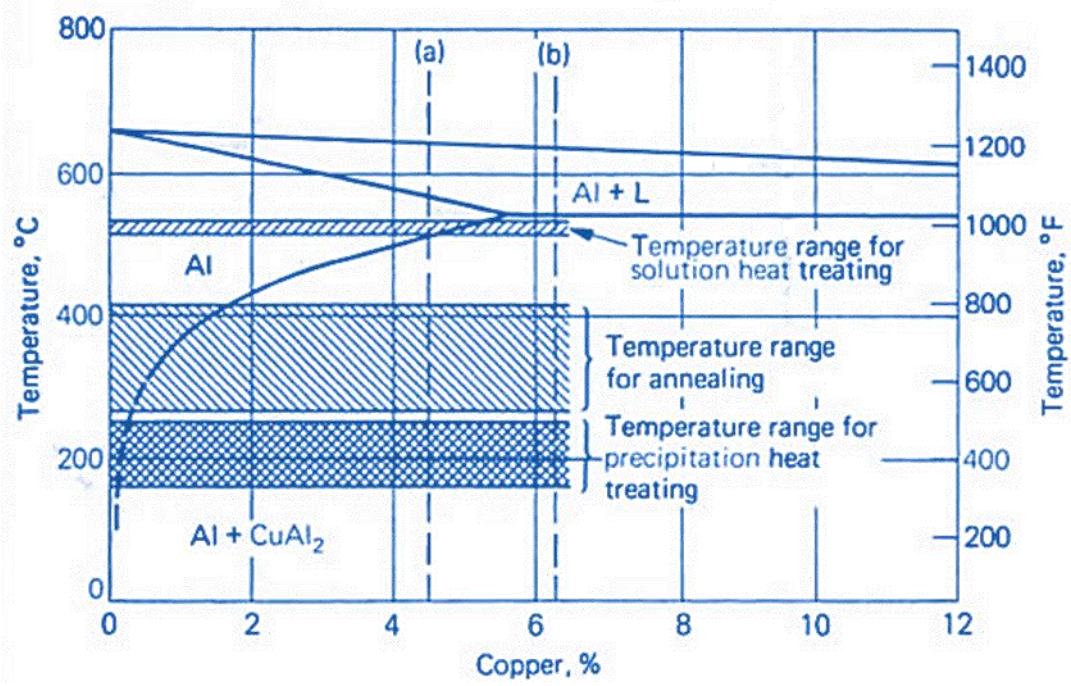

Figure 2.2 Temperature range for aluminum-copper alloys heat treatment.[24]

Figure 2.3, shows a decreasing solid solubility along the solvus between α and α + θ regions, as the temperature decreases. Taking Al-4%Cu alloy as example, it has a considerable degrease in the solid solubility of solid solution α in decreasing the temperature from 550°C to 75°C, it also shows the produced microstructure through the three steps in the age-hardening heat treatment.[25-26]

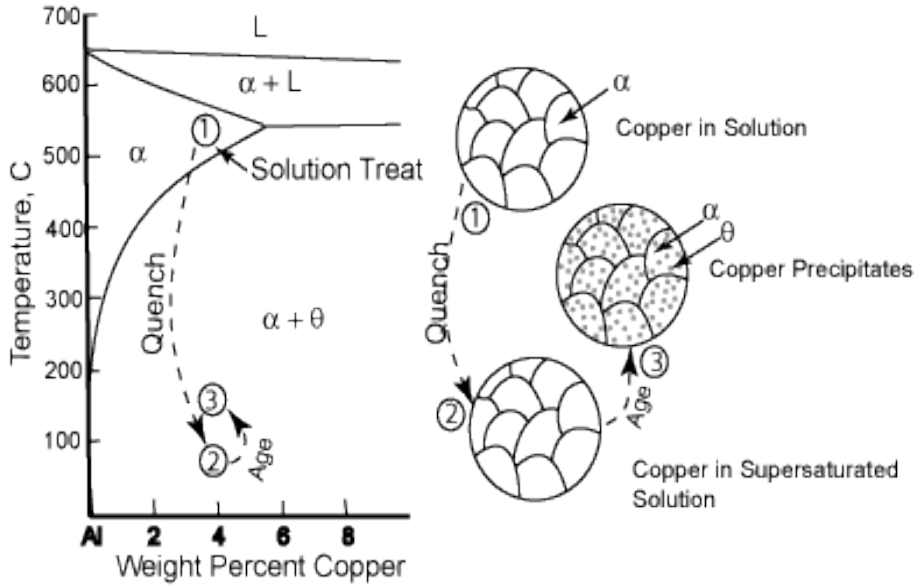

Figure 2.3 Aluminum-copper alloys diagram and microstructures showing the three steps in the age-hardening heat treatment .[26]

A typical T6 heat treatment consists of three steps:

(a) Solution heat treatment, where the alloy is heated to a temperature above its solvus temperature and maintained there for a period of time until a homogeneous solid solution is produced, and also to maximize the solid solubility of Cu in the matrix, dissolve the intermetallics formed during solidification, and to increase the uniformity of the microstructure. Solution heat treatment at 490°C for 8 hours is typically applied.[27-28]

(b) Quenching in warm water at ~60°C, where castings are rapidly quenched by cooling to lower temperatures in water, oil, or any other suitable quenching medium. The objectives of this step are: forming a supersaturated solid solution, preventing the precipitation of equilibrium phases such as Al_2Cu and Mg_2Si, and retaining the highest

amount of vacancies possible within the atomic lattice.[29-32] It is highly recommended that quenching be performed as soon as possible to minimize the time delay in quenching.[17, 29]

(c) Aging, where the alloy is heated below the solvus temperature at a specific temperature for a specified time. Depending on the aging conditions, the alloy proceeds through the underaged, peak aged, and overaged stages after various aging times.

During aging, a finely dispersed precipitate is produced. Atoms diffuse only a short distance, for the supersaturated α-Al is not stable, the extra copper atoms diffuse to several nucleation sites and precipitates grow. These finely dispersed precipitates in the alloy give rise to the precipitation hardening, for they prevent the movement of dislocations by forcing them to either cut through the precipitates or to go around them, so that the alloy is strengthened.[26]

Four structures of the precipitates can be recognized in age hardening of Al-Cu alloys: (i) GP-1 zones, (ii) GP-2 zones (also called θ"), (iii) θ’ phase, and (iv) θ-($CuAl_2$) phase. During the early stages of aging, many solute-rich clusters are formed, that are completely coherent, forming the fcc lattice as shown in Figure 2.4. As the atomic dimensions of the solute-rich regions are different from that of the lattice, strains occur in the lattice regions around the clusters. These regions that are deformed by the clusters are referred to as Guinier-Preston zones (GP zones).[24, 26, 33]

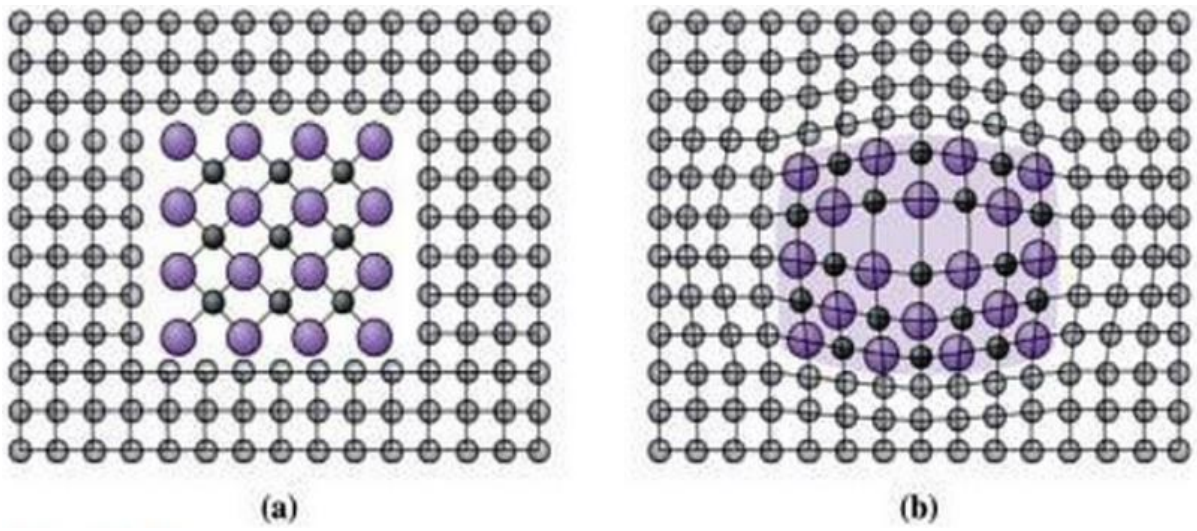

Figure 2.4 (a) A non-coherent precipitate that is not related to the crystal structure of the surrounding matrix. (b) A coherent precipitate that is related to the structure of the surrounding matrix.[26]

GP-1 zones grow rapidly up to a certain size, typical of the temperature of aging, and then growth stops. At room temperature they are 3-7 nm thick, and at 70-130°C the diameter is of the order of 10-15 nm. Hardening accompanies the formation and growth of the GP-1 zones; because of the distortion of the lattice which inhibits the movement of dislocations. The GP-1 zones are replaced by GP-2 zones as the aging progresses. They are larger than the GP-1 zones but smaller in number, as the amount of solvent in the zones does not change. These GP-2 zones (or θ" phase particles) are 10-100 nm in diameter, and 1-4 nm thick. The intermediate 'θ' phase will begin to form, causing recrystallization, and a decrease in strength with continued aging, termed "over-aging".

The size of the θ' phase depends on the aging time and temperature. Finally θ' phase is replaced by θ-($CuAl_2$) which has the same structure and composition as the θ phase

obtained upon solidification. Below 80°C, aging seldom advances beyond the GP-1 stage. Above 220°C the θ' phase appears within a certain time period, while temperatures above 280°C are needed for the θ phase to appear. On the contrary, at higher temperatures the early precipitation stages do not appear: the GP-1 zones are not observed above 180°C, and the θ" phase will not form above 230°C. Figure 2.5 shows the sequence of precipitation stages with the progress of aging time. The peak-aged condition corresponds to the maximum strength that the alloy can achieve. In the over-aged condition, the alloy strength decreases as the alloy begins to soften, and its ductility improves. Figure 2.6 shows examples of the microstructures of Al-4.5%Cu alloy samples in peak-aged and overaged conditions. [24, 26, 33-42]

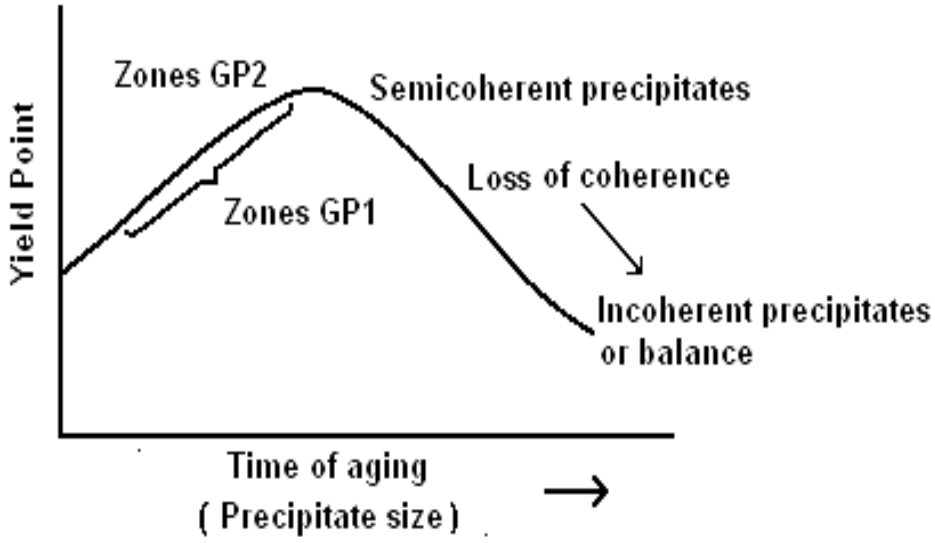

Figure 2.5 Precipitation stages with aging time.[33]

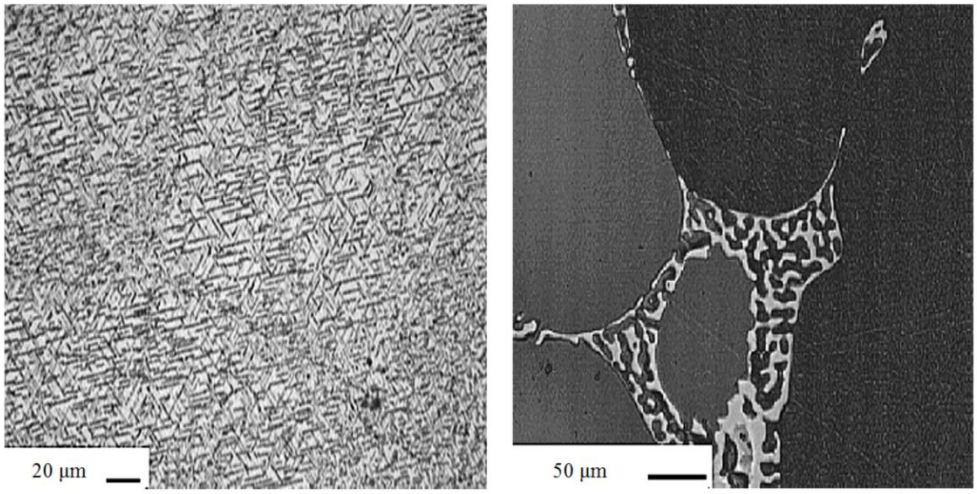

(a) (b)

Figure 2.6 Microstructures of Al-4.5wt%Cu alloy, showing (a) fine Al_2Cu precipitates in the age hardened condition, and (b) coarse Al_2Cu particles (white) in the overaged condition.[34]

2.2 HOT TEARING

Hot tearing is one of the major problems of casting technology, and has been investigated since the beginning of the 20th century. In 1936, Verö presented his study of the hot shortness of aluminum alloys and reported that hot tearing was caused during solidification of the alloy because of the stress developed from the contraction of the primary phase. In the first stage of solidification, a coherent network has not yet formed, and thus hot tears would not occur. During growth of the dendrites, the coherent network forms. Further solidification would produce stress when the alloy contraction is restrained by the mold. If the remaining eutectic liquid is sufficient, it would feed the incipient tears. Eskin and Pumphrey *et al.*[43, 44] reported that even though the strength of the metal increases with decreasing solidification temperatures, hot tears still could develop as long as a small

amount of residual liquid remained. A summary of mechanisms, conditions, and causes of hot tearing is shown in Figure 2.7.[43-45]

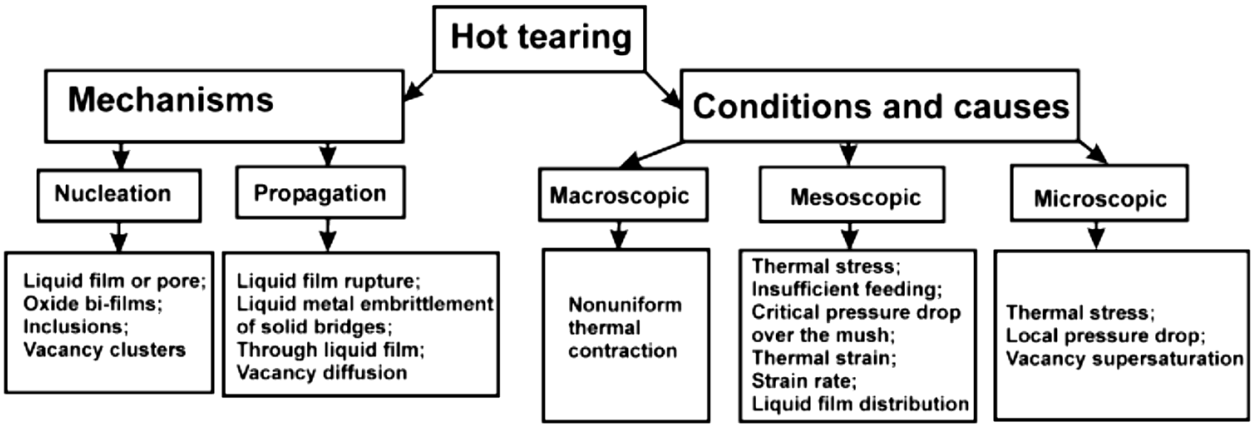

Figure 2.7 Summary of mechanisms, conditions, and causes of hot tearing.[43]

Early studies all considered that hot tearing was induced by the stress buildup in the metal during solidification and cooling due to the hindered contraction. In 1952, Pellini *et al.*[44] studied the initiation of hot tear by means of radiography and thermal analysis of solidifying castings and introduced the concept of liquid film. In Al-Cu alloys the hot tear started at a temperature between 93% and 96% solid.

In 1961, Saveiko[44, 45] developed a theory of hot tearing based on the interdendritic liquid film between dendrites. The surface tension of the liquid film was considered of great importance in his theory. The model demonstrating the hot tearing formation on a microscopic scale according to this theory is shown in Figure 2.8.[45]

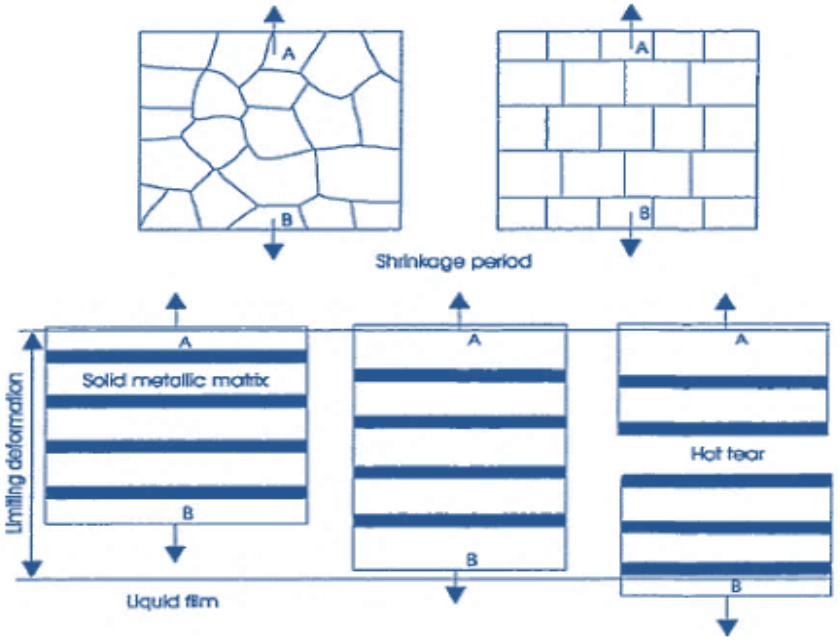

Figure 2.8 Hot tearing formation based on an interdendritic liquid film concept. [44, 45]

In the model the grains were simplified and assumed to be cubical in shape. As shrinkage progresses, the grains at A and B move along the arrowed directions as shown, and the extension between them increases. At a certain point during the movement, a tear may form along one of the liquid films. To separate the liquid film to form two new surfaces, work must be done to overcome the molecular adhesion force. The force required to tear apart the liquid film is:

$$P = (2\alpha F) / (1000\ bg)$$

where α is surface tension of the liquid in erg/cm. F is the area of contact between the plates and liquid in cm. b is the thickness of the liquid layer between the plates in cm, and g is gravitational acceleration constant in cm/s. The film thickness is considered to be more

important than surface tension since it varies to a greater extent than surface tension with the change of grain size. This explains why alloys with fine grains are more resistant to hot tearing. In ductile materials, most of the fracture energy is consumed at the root of the growing crack tip during plastic deformation.

Generally, the theories of hot tearing may be summarized into two groups: One group of theories is based on stress, strain, and strain rate, and these are related to the thermo-mechanical properties of the alloy. The other group is based on the liquid film concept and lack of feeding, which are related to metallurgical factors. It can be concluded that hot tearing is a complex phenomenon which combines metallurgical and thermo-mechanical interactions, and there is still no agreement on the controlling factor that causes its formation.

Over the years, different macroscopic and mesoscopic parameters, such as stress and strain, were considered as critical for the development of hot tearing. Today, the macroscopic strain rate is believed to be the most important factor and some modem models are based on it. The physical explanation of this approach is that semisolid material during solidification can accommodate the rearrangement, and filling of the gaps and pores with the liquid. All these processes require some time, and the lack of time will result in fracture, resulting: a maximum strain rate that the semisolid material can endure without fracture during solidification. On the mesoscopic and microscopic level, the important factor is believed to be the feeding of the solid phase with the liquid. Within this approach, the hot tear will not occur as long as there is no lack of feeding during solidification.

Katgemian and Eskin [43] used hindered feeding as a basis for their porosity and hot tearing criteria. The feeding depends on the permeability of the mushy zone, which is largely determined by the structure. Later, a two-phase model of the semisolid dendritic network, which focuses on the pressure depression in the mushy zone, was suggested to describe the hot tear formation.[44-46]

The pressure drop of the liquid phase in the mushy zone is considered as a cause of a hot tear. An extension of the two-phase model, which includes plasticity of the porous network, is also reported. These models do not distinguish between pore formation and crack initiation, the void being considered as the crack nucleus, although the pores should not necessarily develop into a crack. The crack may nucleate or develop from another defect and then propagate through a chain of pores. Logically, bridging and grain coalescence, which determine the transfer of stress and limit the permeability of the mushy zone, are the other important microscopic factors for the development of hot tearing.

It is obvious that the actual hot tearing mechanism includes phenomena occurring on two scales: microscopic (crack nucleation and propagation, stress concentration, structure coherency, wet grain boundaries) and mesoscopic (lack of feeding, stress, strain, or strain rate imposed on the structure). Figure 2.9 illustrates these scales during equiaxed dendritic solidification.[44-47]

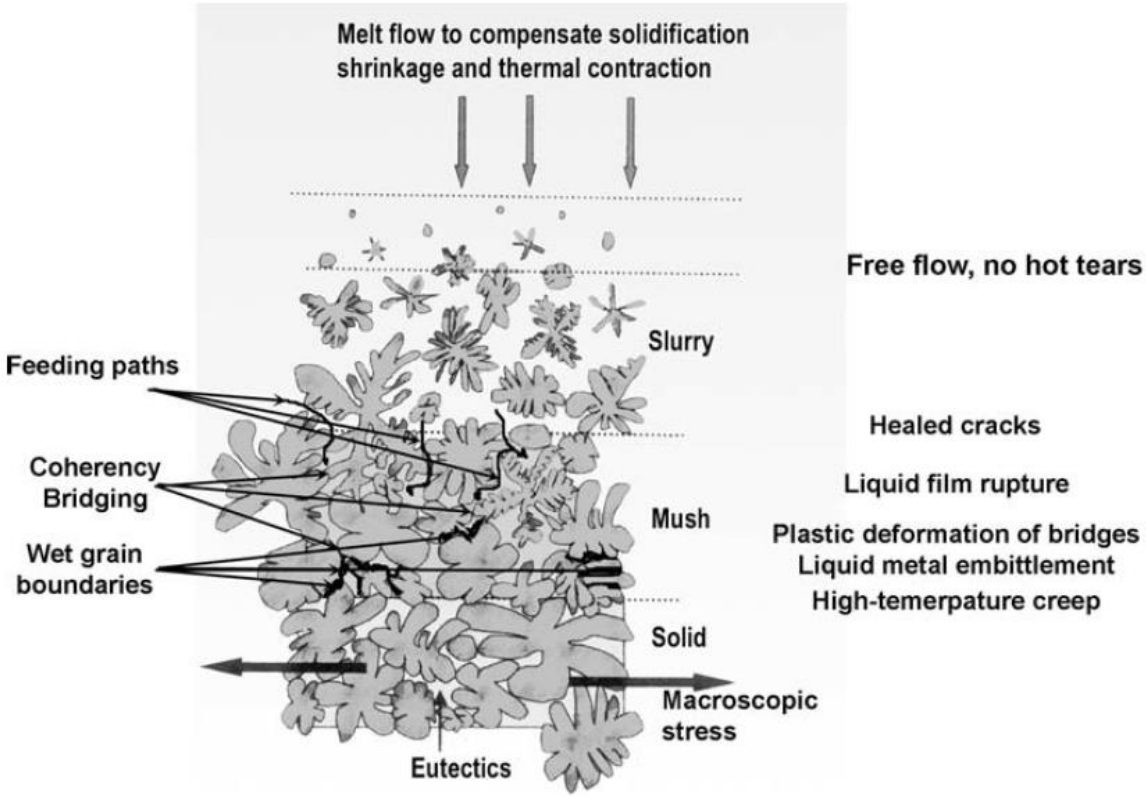

Figure 2.9 Length scales of equiaxed dendritic solidification.[45-47]

2.3 ROLE OF ALLOYING ELEMENTS

The role of the addition of alloying elements on the properties of materials is well documented in the literature. In the following subsections, the alloying elements used in this study, their characteristics and their effects on aluminum alloys will be presented.

Zirconium and Scandium

Zirconium (Zr) is a lustrous, grey-white, soft and malleable metal which is solid at room temperature, and highly corrosion resistant. It is added to increase the strength of aluminum alloys, based on the production of precipitates in the form of primary

intermetallic particles of Al_3Zr. Zirconium is also used in a wide selection of aluminum alloys to control the microstructure and mechanical properties. It has the smallest diffusion flux in aluminum of all the transition metals. Zirconium atoms have a high binding energy with the vacancies of aluminum.[48, 49] The Al_3Zr particles are resistant to dissolution and coarsening, and control the evolution of the grain and sub-grain structure, thus providing the means to enhance and maintain the alloy strength and ductility in the precipitation-hardened T6 condition or during subsequent processing operations. Figure 2.10 depicts the Al-Zr binary phase diagram. [19, 50]

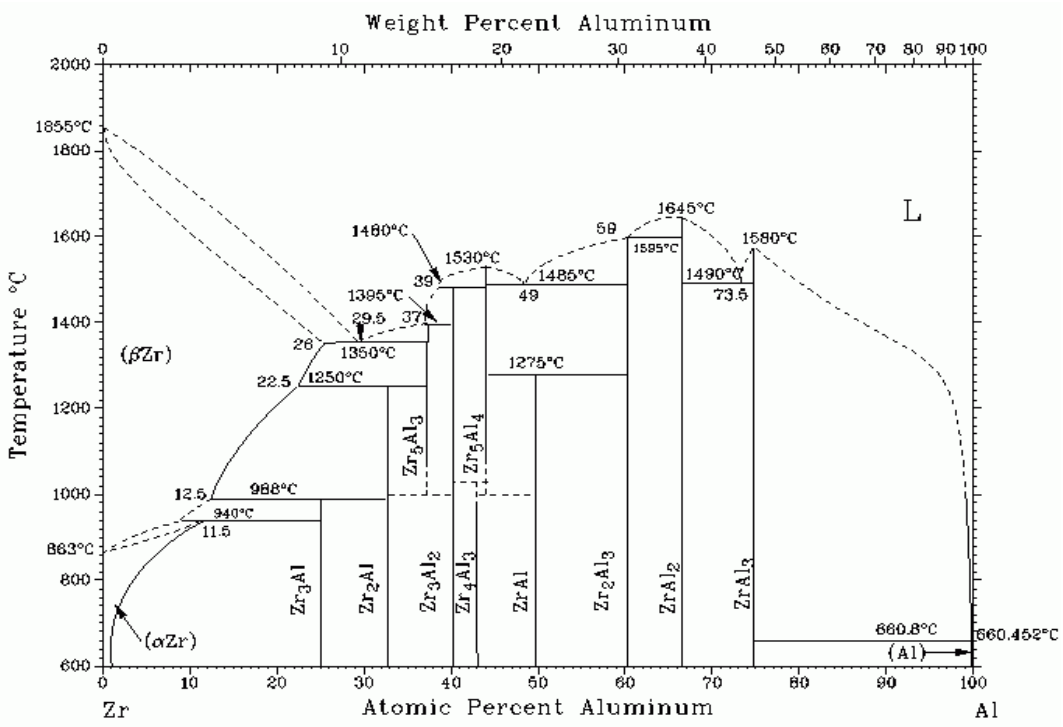

Figure 2.10 Al-Zr binary phase diagram.[19, 50]

The Al_3Zr phase exhibits two different crystallographic structures: the stable tetragonal DO_{23} structure which is body-centered with eight atoms per unit cell, and the coherent metastable Ll_2-type structure which is simple cubic with four atoms per unit cell, and having a slight lattice mismatch with the α-Al phase, Figure 2.11. [51, 52]

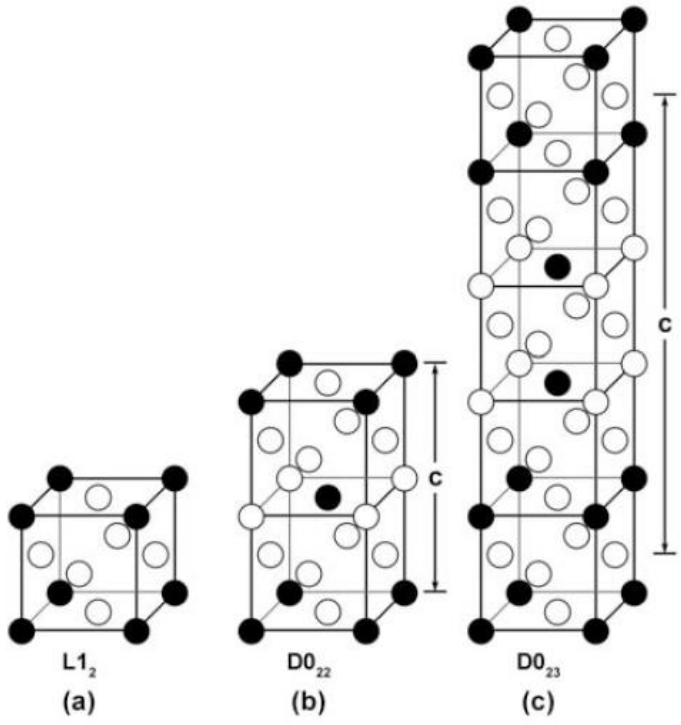

Figure 2.11 a) $L1_2$, b) DO_{22}, and c) DO_{23} structures.[51]

The body-centered tetragonal DO_{22} (or DO_{23} for Al_3Zr) structures, received a considerable attention for their high-strength, high-temperature structural materials. However, the low-symmetry tetragonal structure makes these phases intrinsically brittle. Both DO_{22} and DO_{23} structures are closely related to the cubic $L1_2$-type structure. A lot of

effort has been received on alloying this binary intermetallic to transform them to the $L1_2$-type structure, for improving their toughness.[51]

The structure of the Al_3Zr intermetallic phase is dependent on the level of Zr added to the alloy and on the cooling rate. Al_3Zr can dissolve up to 5 wt% Sc to form $Al_3(Zr_{1-x}Sc_x)$ phase particles; with a corresponding decrease in the lattice parameter of that phase. The $Al_3(Zr_{1-x}Sc_x)$ phase may also form upon decomposition of the solid solution or as a primary phase during solidification. The primary $Al_3(Zr_{1-x}Sc_x)$ phase has a greater grain refining efficiency than Al_3Zr phase. In addition, primary Al_3Zr phase particles may also act as nucleation sites for Al_3Sc particles. As the Al_3Sc phase nucleates on the surface of Al_3Zr phase particles, the grain refining capacity of the primary Al_3Zr phase particles for α-Al is improved, due to the small lattice misfit between the Al_3Sc phase and α-Al.[52-58]

The addition of scandium (Sc) to aluminum alloys has numerous advantages: it provides significant grain refinement, strengthens welds, and eliminates hot cracking in welds. Aluminum alloys containing Sc also exhibit a strong resistance to corrosion. The addition of Sc also improves fatigue life.[59, 64] Figure 2.12 illustrates the Al-Sc binary phase diagram. [50]

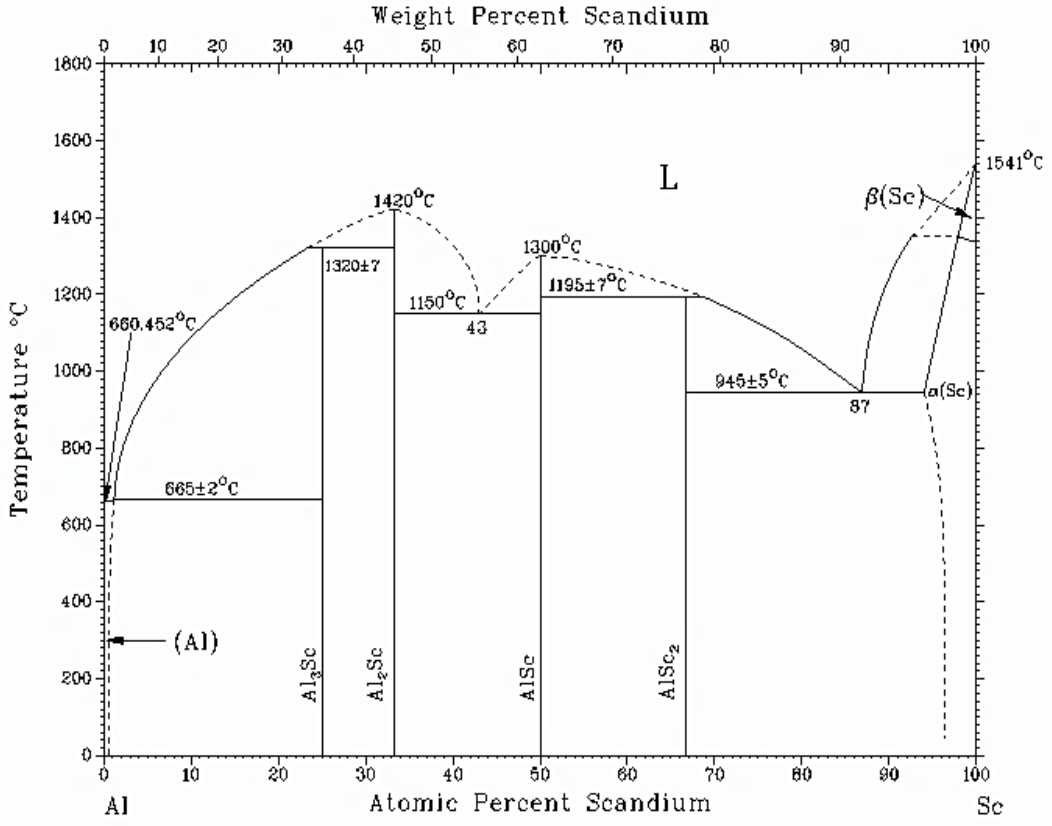

Figure 2.12 Al-Sc binary phase diagram. [50]

Transition metals such as zirconium, manganese, or titanium are not very effective at inhibiting recrystallization. Scandium increases the recrystallization of aluminum alloys. A small addition of scandium with zirconium is more effective than adding scandium alone; with Zr, a non-dendritic structure is formed with a Sc content as low as 0.2%; on the other hand, without Zr, more than 0.5% Sc is required to obtain a non-dendritic structure.

The synergistic interaction between Sc and Zr is effective in inhibiting recrystallization through the formation of extremely fine $Al_3(Zr_{1-x}Sc_x)$ particles. These particles are less prone to coagulation compared to Al_3Sc particles. [65-68] Scandium is a

strong modifier of the cast structure and the addition of scandium makes it possible to obtain continuously cast billets with a non-dendritic structure. For these advantages, Sc-modified aluminum alloys have a promising potential for automotive, transport systems, military and commercial aerospace applications.[69]

Strontium

Strontium (Sr) added to aluminum casting alloys containing silicon (Si) element to modify or change the morphology of the Si particles, from coarse flakes to a finer spherical form. Figure 2.13 shows the Al-Sr binary phase diagram.[50] Also, the absorption of strontium by iron intermetallics, refines their morphology.[9-11]

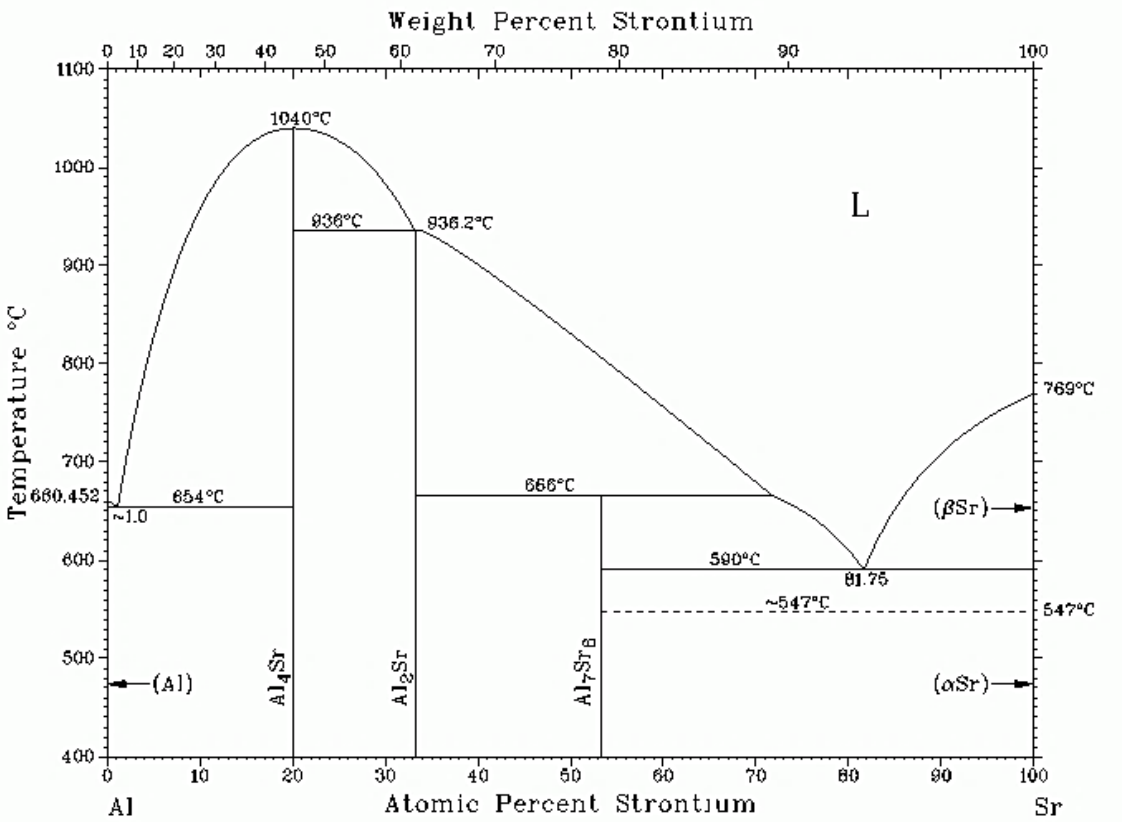

Figure 2.13 Al-Sr binary phase diagram.[50]

Strontium modification contributes to lowering the actual eutectic temperature. The lower the eutectic temperature, the greater the modification effect expected.[70]

Titanium

The melting point of the pure titanium (Ti) is 1668 °C (3034 °F), in solid state the titanium alloys are either hexagonal close-packed (α) or body-centered cubic (β) structure. Pure titanium undergoes an allotropic transformation from hexagonal close-packed (HCP) alpha titanium to body-centered cubic (BCC) beta titanium as its temperature is raised through 882 °C (1620 °F). Titanium is added individually or in combination with boron (B) is used to refine the grain structure of α-Al, as it creates many nuclei in the melt, which encourage the formation of small equiaxed grains of α-Al, which otherwise solidifies with a coarse, columnar grain structure. Titanium as a grain refiner is very effective in reducing the grain size.

The titanium-aluminum binary system provides a model for solution strengthening. In addition to that, it is the prototype of technical α alloys, as well as the components of α + β alloys. Figure 2.14 shows the Al-Ti binary phase diagram. It is well known that; the most widely used alloying element in titanium based alloys is aluminum.[56, 70]

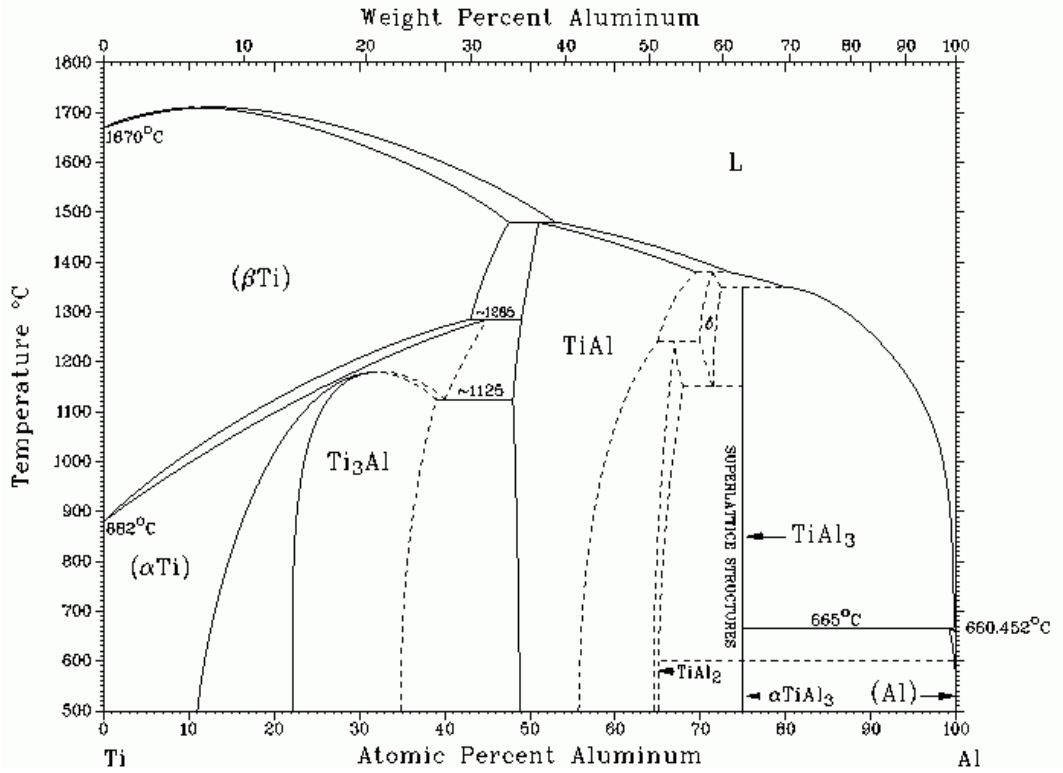

Figure 2.14 Al-Ti binary phase diagram.[50]

Both Ti_3Al phase (referred to as α_2) and TiAl (gamma) phases, which are apart from the alpha-Ti and beta-Ti phases, are of great technical importance.

Silver

One of the important additions used in Al-Cu alloys, silver (Ag) is added to Al-Cu alloys to improve the strength values. Addition of silver to alloys of Al-Cu-Mg has been known to form a hexagonal-shaped Ω-strengthening phase.

The Ω phase, is a variant of the equilibrium θ (Al_2Cu) phase, and is mostly found in Al-Cu-Mg-Ag alloys and improves high-temperature strength because of its thermal stability. Figure 2.15 illustrates the Al-Ag binary phase diagram. The Ag-rich terminal solid

solution (Ag), has a maximum solubility of about 20.4 at % Al. at about 450 ^{o}C, were the Al-rich terminal solid solution (Al), has a maximum solubility of about 23.5 at % Ag. at about 567 ^{o}C.

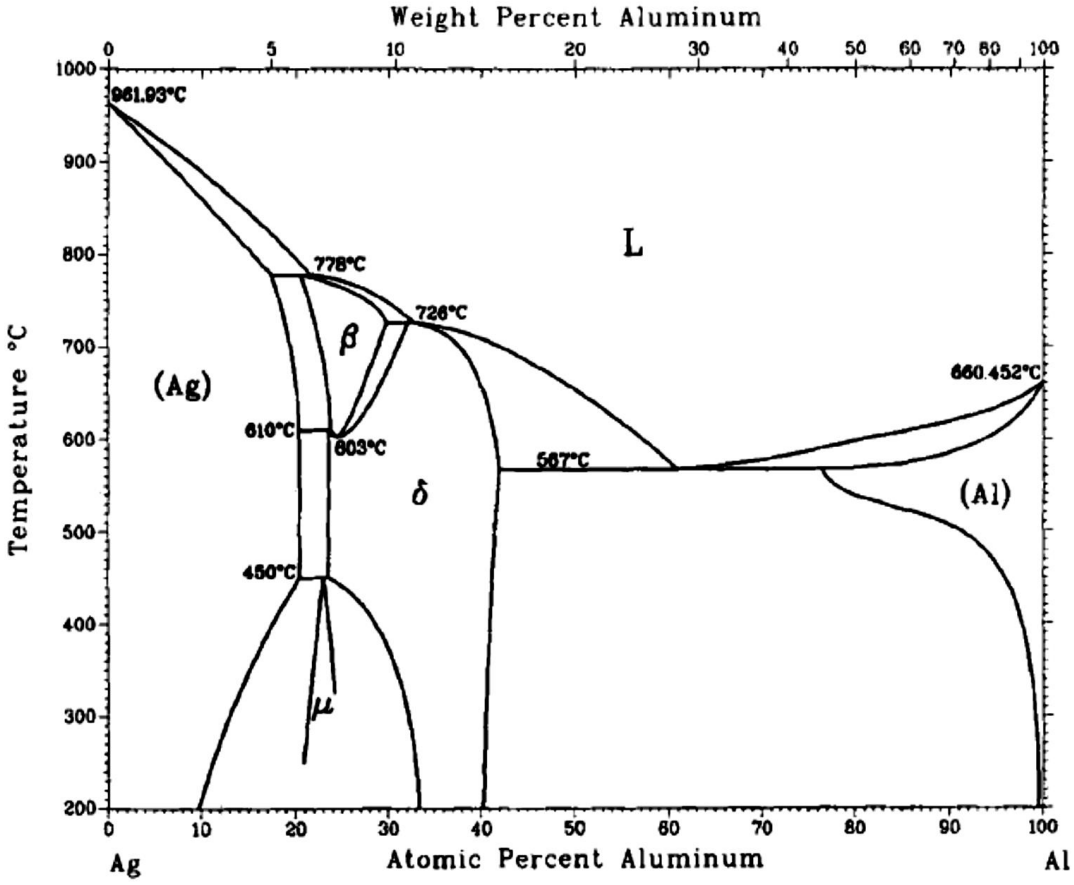

Figure 2.15 Al-Ag binary phase diagram.[12-14, 50]

Silver significantly reduces the width of precipitate-free zones (PFZ) which suppresses the inter-granular fracture and therefore improves the ductility of the alloys.[12-14]

Silicon

Silicon increases the strength in cast alloys, mainly by increasing the castability and thus the soundness of the castings, but with some loss of ductility and fatigue resistance, especially when it changes the iron-bearing compounds from FeM_2SiAl_8 or Cu_2FeAl_7, to $FeSiAl_5$.[71-73] Magnesium increases the strength and hardness of the alloys, but, especially in castings, with a decided decrease in ductility and impact resistance. Iron has some beneficial strengthening effect, especially at high temperature and at the lower contents (< 0.7% Fe), it also tends to form insoluble compounds which affect the alloy properties. Negative effects of iron in aluminum cast alloys can be minimized by applying any of the following techniques:

1. Rapid solidification.
2. Addition of neutralizing elements.
3. Melt superheating.
4. Strontium modification.
5. Non-equilibrium solution heat treatment.

As may be noted from the Al-Si binary phase diagram in Figure 2.16, the melting points of Al and Si are 660.45°C and 1414^{o}C, respectively, while the eutectic reaction occurs at 12.2 wt. % Si and 577 ^{o}C. The maximum solubility of Si in Al occurs at the eutectic temperature and is 1.65 wt. %. At least up to the late 1950's, the eutectic was believed to be at 11.6 wt. % Si. Solubility of Si in aluminum can be greatly extended by splat quenching of the liquid.

Al-Si alloys have not been reported to form metastable intermetallic compounds or glassy alloys. Metastable extensions of the equilibrium boundaries and T_0 curves of equal Gibbs energies are of interest in interpreting the results of rapid solidification experiments.[50, 70]

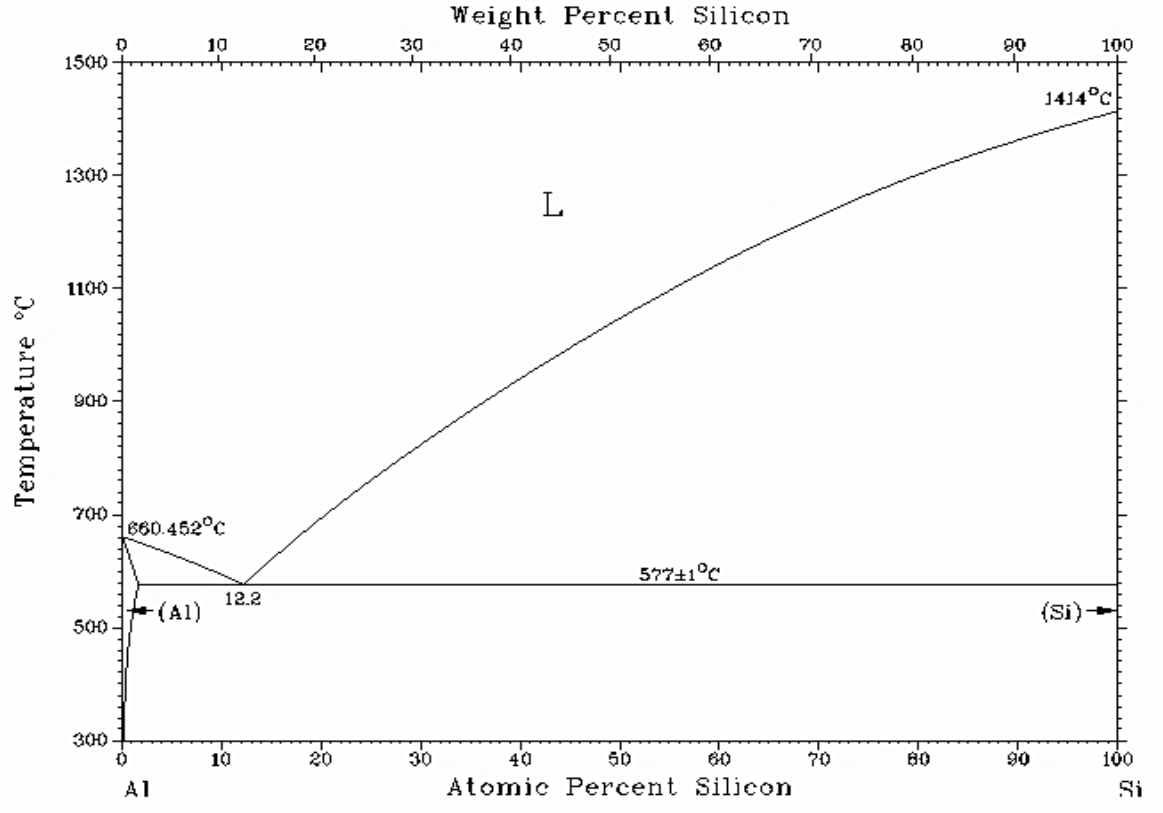

Figure 2.16 Al-Si binary phase diagram.[50]

2.4 INTERMETALLIC PHASES

Iron Intermetallic Phases

Particle types of AlFeSi can generally be divided into three different categories by morphology: polyhedral crystals (primary α-phase), Chinese script (α-phase), and thin

platelets (β-phase), Figure 2.17. Crystallization and volume fraction of the three different AlFeSi particle morphologies depends on the ratio of Fe:Mn, the cooling rate, and the melt holding temperature. The main intermetallics observed in aluminum alloys are the α-Fe and β-Fe intermetallic phases. The composition of the α-Fe phase is Al_8Fe_2Si (31.6%Fe, 7.8%Si) and $Al_{12}Fe_3Si_2$ (30.7%Fe, 10.2%Si). These phases are dominant in slowly-cooled castings, whereas the metastable phases Al_6Fe (orthorhombic) and α-$Al_{20}Fe_5Si_2$ (cubic) occur in the rapidly quenched condition.[9-11]

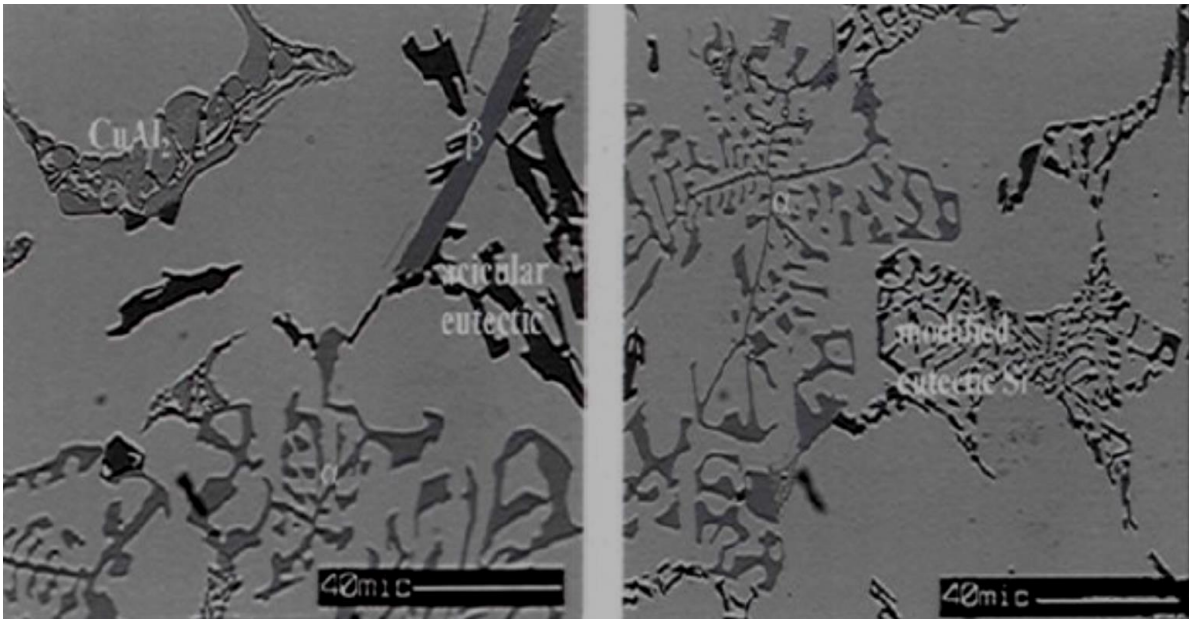

Figure 2.17 As-cast 319 alloy showing the morphology of β -Fe and α-Fe intermetallic phases.[74]

Al-Fe eutectic exists at 1.7%Fe at 655°C, shown in Figure 2.18. Melting maintained at 800°C get the Fe level up to 5%. Fe can enter an aluminum melt through the addition of the low-purity alloying materials such as Si. [28-31, 50]

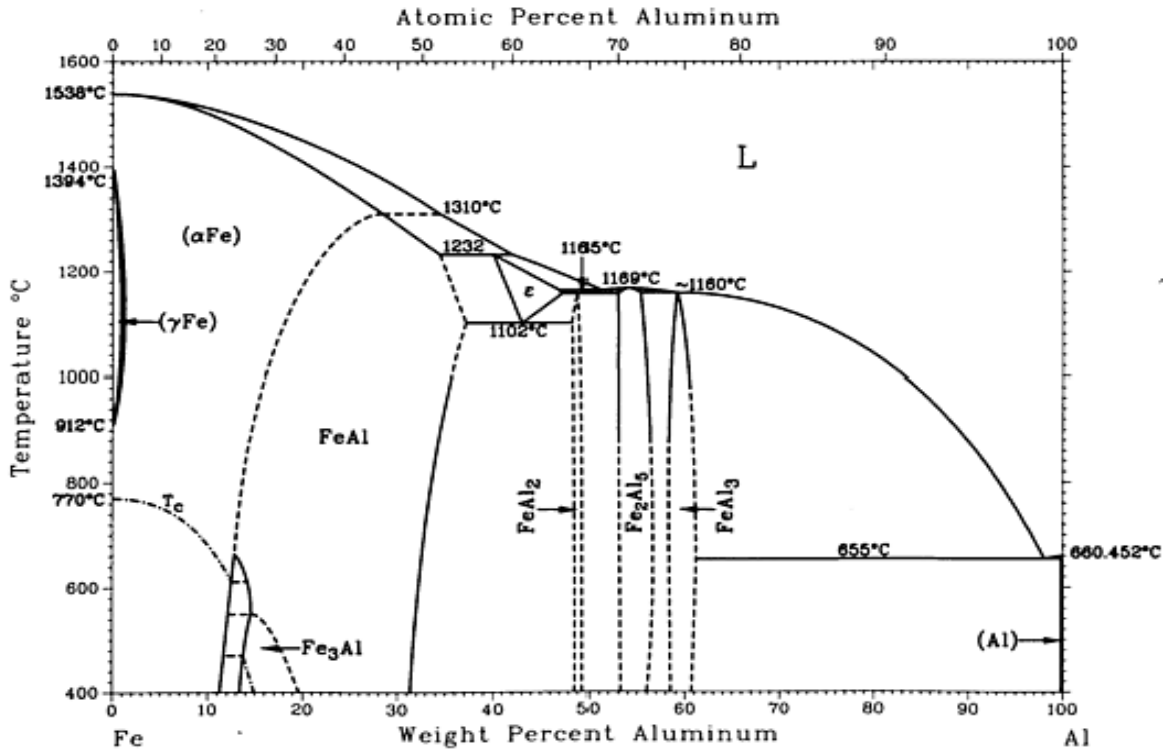

Figure 2.18 Al-Fe binary phase diagram.[50]

The β-Fe phase is Al_5FeSi (25.6%Fe, 12.8%Si), with a range of 25-30% Fe and 12-15% Si, has a monoclinic structure with parameters a=b=6.12 Å, and α=91°, a density of 3.30-3.35% g/cm^3, and it appears in the form of thin platelets in the microstructure. The temperature at which β-Fe can form prior to the Al-Si eutectic decreases with increasing Si content for a given Fe content. The morphology of the phase allows it to act as a stress raiser. The threshold amount of iron leading to the formation of primary Al_5FeSi capable of undermining the properties is said to be >0.7%. Increasing the Fe content in Al-Si-Cu alloys continuously decreases the ductility, and drastically so, for Fe contents above 0.9%. The coarse β-Fe phase platelets interfere with the flow of the liquid metal, which reduces

the feeding during solidification, thereby promoting the formation of the porosity. The percentage of iron which forms the primary or the secondary Al_5FeSi depends on the cooling rate and the silicon content. The effects of increasing Fe may be seen in the gradual reduction of the elongation, impact strength, and tensile strength of aluminum alloys, while hardness and yield strength are reported to increase. Whereas an Fe content of up to 0.2% improves the tensile strength, higher levels of 0.5-1.2% in an Al-Si casting alloy reduce the mechanical properties, mainly ductility, due to the formation of the β-Fe platelets. Iron, manganese, and chromium tend to segregate towards the bottom of melting and holding furnaces for aluminum, to form solid particles of the an iron phase which may precipitate in the form of the Chinese script-like $Al_{15}(Fe,Mn,Cr)_3Si_2$, termed sludge. An empirical formula called the "sludge factor" was proposed by Gobrecht,[75] and is used to determine the levels of the Fe, Mn, and Cr which will cause the formation of sludge in Al-Si alloys. This factor can be calculated as follow: [75, 76]

$$\text{Sludge Factor (S.F.)} = 1 \times \text{wt\% Fe} + 2 \times \text{wt\% Mn} + 3 \times \text{wt\% Cr} \quad \text{Eqn. 2.1}$$

This formula is used in predicting susceptibility to sludge formation. The critical sludge factor beyond which sludge is formed equals 1.8 in cases when the melt holding temperature of 650ºC is maintained. A critical sludge factor of 1.4 is recommended, as the sludge formation is a "temperature-dependent" process in addition to the Fe, Mn, and Cr concentrations. [28-31, 75, 76]

Precipitation-Hardening Phases

Precipitation hardening in the Al-Cu system occurs through the decomposition of a supersaturated Al-Cu solid solution during the aging process. As depicted schematically in Figure 2.19, the precipitation sequence begins with the formation of coherent Guinier-Preston zones (GPZ) which are clusters of copper atoms having a disc-like shape. The GP zones are ultimately replaced by the coherent θ'' phase with a tetragonal structure as aging progresses, both phases lies in the {100} planes of the matrix. With further aging, the metastable θ' phase is formed.[18]

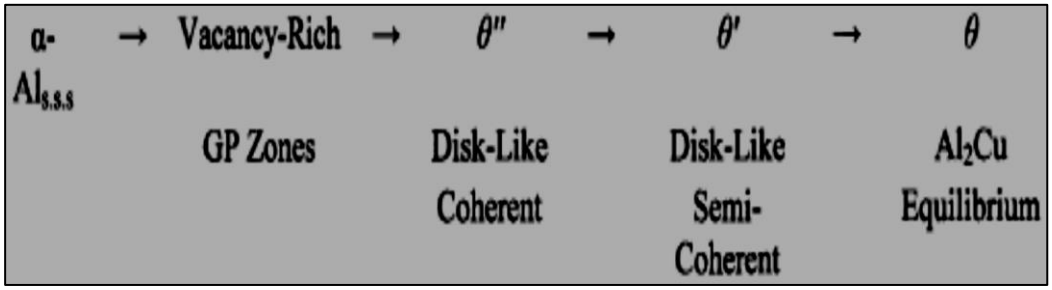

Figure 2.19 Al-Cu alloys precipitation-hardening.[18]

The equilibrium precipitate, θ, is formed in the overaging condition, when the θ' phase begins to lose coherency in the time that the dislocation accommodates the interface misfit between the precipitates and the matrix.[18]

The precipitation-hardening characteristics of these alloys appear to be complex, due to the formation of several hardening phases such as θ' (Al_2Cu), β'' (Mg_2Si), S' (Al_2CuMg), and AlMgSiCu which is called the Q phase ($Al_5Mg_8Si_6Cu_2$). Solution heat treatment is applied to the Al-Si-Cu-Mg alloys system to change the morphology of the

interdendritic phases and maximize the dissolution of precipitation-hardening elements which will give rise to such precipitates as $CuAl_2$, AlMgCu, and Mg_2Si upon aging.[31, 32]

2.5 QUALITY INDEX (Q)

The Quality index (Q) represents a numerical value that defines the quality of an aluminum alloy/casting, and is related to the UTS and plastic strain of the material to fracture. Drouzy, Jacob and Richard developed an empirical formula to characterize the mechanical performance (quality) of Al-7%Si-Mg casting alloys, using the following equations: [77, 78]

$$Q = UTS + d \log (E_f) \qquad \text{Eqn. 2.2}$$

where Q and UTS are in MPa, d is a material constant equal to 150 MPa for Al-7%Si-Mg alloys, and E_f, is the elongation to fracture in a tensile test.

$$YS = a\ UTS - b \log (Ef) + c \qquad \text{Eqn. 2.3}$$

where the coefficients a, b, and c were calculated as 1, 60, and -13 respectively, for Al-7%Si-Mg alloys, with b and c expressed in MPa.

The quality index value is used to indicate the level of the quality of the castings which are susceptible to improvement through the following factors; adequate control of the impurity elements, casting defects, modification, solution heat treatment and solidification conditions. Yield strength depends on hardening elements such as magnesium and copper and also on the age hardening process. Figure 2.20 shows the quality index chart proposed by Drouzy *et al*, [77, 78] generated using equations 2.2 and 2.3, which provides information for each point located on the plotted chart. Such charts are very useful in the

evaluation of the appropriate metallurgical conditions to obtain the specified properties required of an alloy/casting, since each point on the chart provides tensile strength (UTS), elongation to fracture (E_f), yield strength (YS), and quality index (Q) values corresponding to specific heat treatment and alloying conditions.

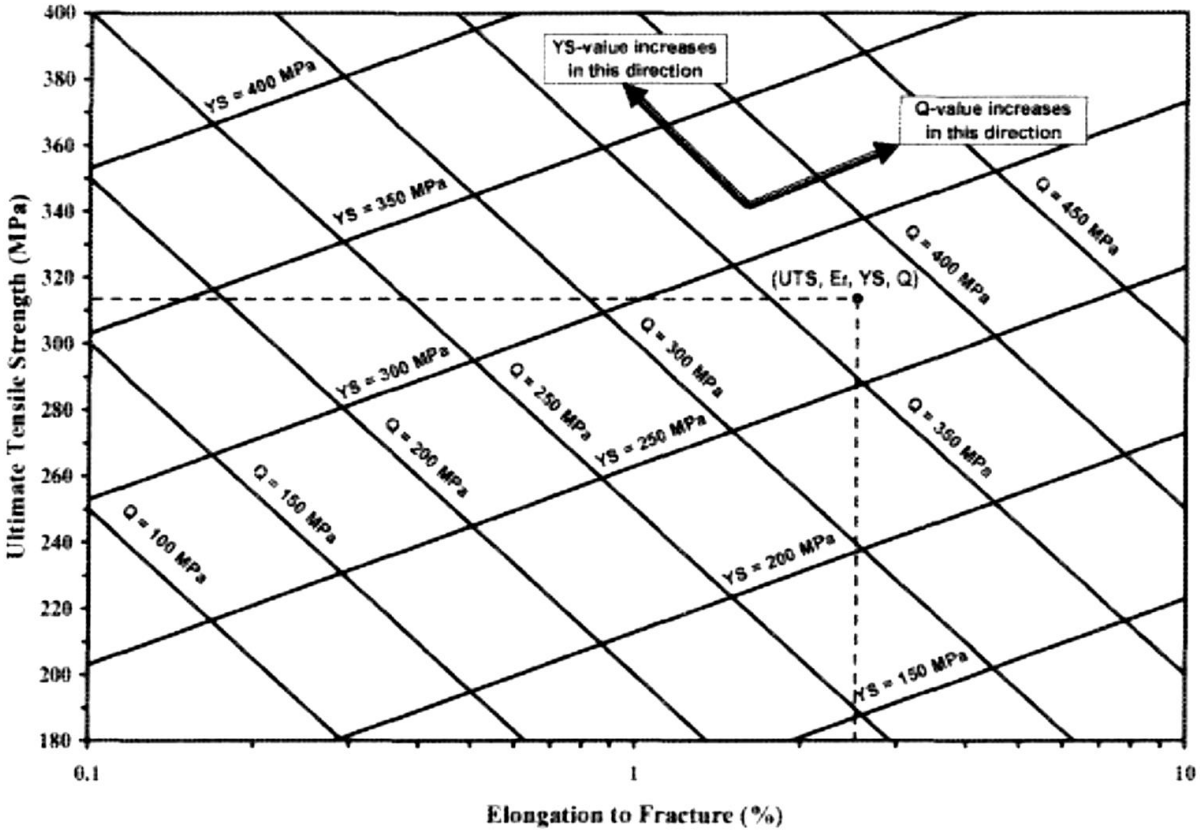

Figure 2.20 Quality chart proposed by Drouzy, generated using Equations 2.2 and 2.3. [77, 78]

Càceres developed a more general framework for casting quality, given by the following equation, which may be used for all alloys: [79, 80]

$$\sigma = K \varepsilon^{n} \qquad \text{Eqn. 2.4}$$

where σ is the true stress, ε is the true plastic strain. K is a material constant and n is the strain hardening coefficient. The strain-hardening exponent n is related to the rate of strain hardening, through the following formula: [79-81]

$$n = (\varepsilon / \sigma) * (d\sigma/d\varepsilon) \qquad \text{Eqn. 2.5}$$

Quality index equations as proposed by Càceres are based on the assumption that the curves of the quality maps follow the Holloman equation, a schematic representation of which is illustrated in Figure 2.21.[19, 20, 33]

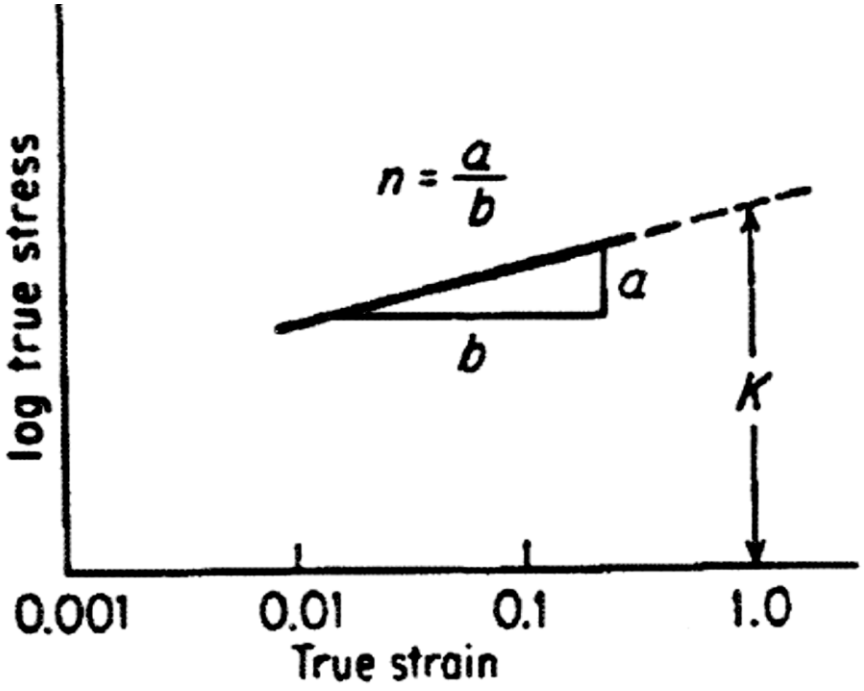

Figure 2.21 A log-log plot of true stress versus true strain.[19, 20, 33]

The strain-hardening exponent, n, related to the relation dP/dS, is presented as follows: [19, 20, 33]

$$n = \frac{d(\log P)}{d(\log S)} = \frac{d(\ln P)}{d(\ln S)} = \frac{S}{P} \times \frac{dP}{dS} \text{ or } \frac{dP}{dS} = n\frac{P}{S} \qquad \text{Eqn. 2.6}$$

Càceres further simplified his work on quality index, by identifying the material quality, through *Q*- and *q*-values as shown in Figure 2.22, using equations 2.7 and 2.8:

$$\sigma = K\,[\ln(1+E)]^{n}\, e^{-\ln(1+E)} \cong K\,E^{n}\, e^{-E} \qquad \text{Eqn. 2.7}$$

$$\sigma = K\,E^{\frac{E}{q}}\, e^{-E} \qquad \text{Eqn. 2.8}$$

Where the true stress P and true strain S are given by P = σ(1+E) and S = ln(l+E), σ and E are the engineering stress and strain, respectively, and K= 511 MPa. The values of n and *K* can be calculated from the log-log plot of true stress versus true strain. [19, 79]

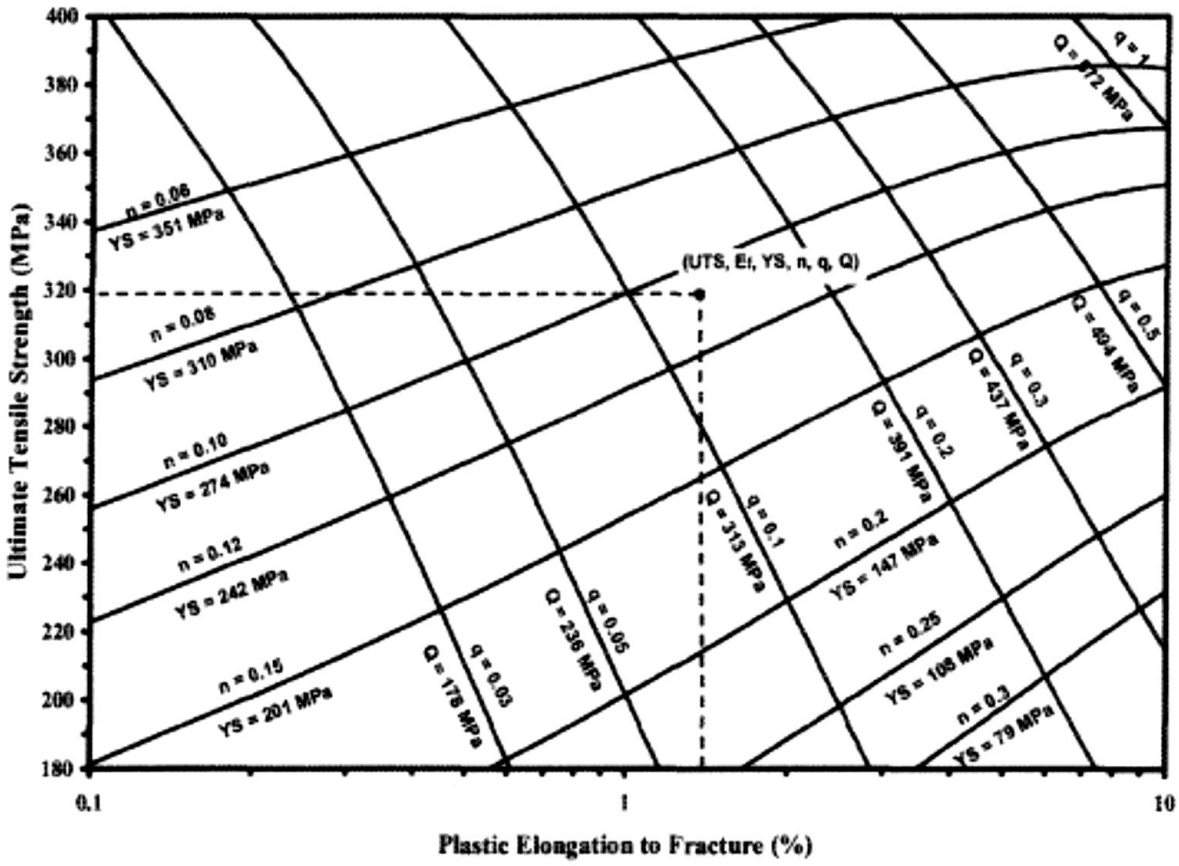

Figure 2.22 Quality chart proposed by Càceres, generated using Equations 2.7 and 2.8. [79, 80]

The quality chart proposed by Càceres may be explained as follow: the line q=1 represents the maximum quality, while those with q<1 represent lesser quality values. Each point located on the chart provides the corresponding tensile strength (UTS), elongation to fracture (E_f), yield strength (YS), relative quality index (q) and quality index (Q) values. The quality chart proposed by Càceres thus provides a good method for the prediction and selection of the most appropriate metallurgical conditions to be used for a specified aluminum casting alloy and the intended application.[79, 80]

2.6 CASTING TECHNIQUES

Among the many techniques which exist for casting alloys, there are three main techniques used for casting aluminum alloys: sand casting, permanent mold casting, and pressure diecasting. Figure 2.23 provides a schematic of the number of castings (or parts) produced per annum for each technique, and the alloy types generally used for preparing the castings.

While all three techniques have been extensively used in foundries for producing diverse aluminum castings, the die casting technique will be focused upon here, as the castings used in the present study were prepared using this technique.[82-84]

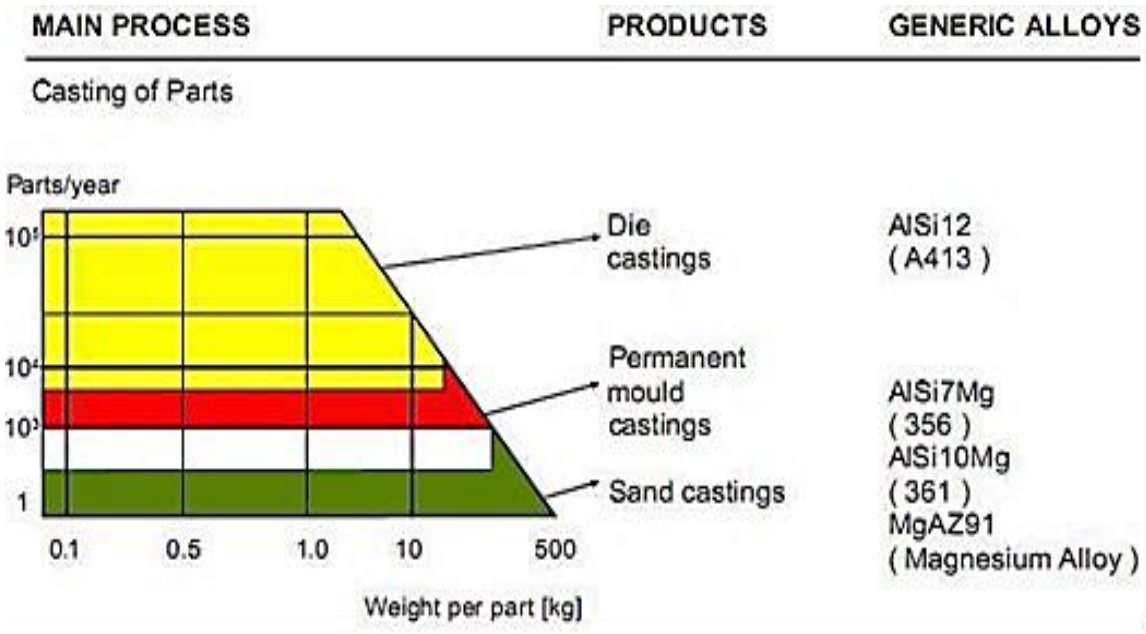

Figure 2.23 Casting methods used for aluminum alloys.[82]

Die Casting Technique

Die casting is a rapidly repetitive operation in which identical parts are cast at high production rates by forcing molten metal under considerable pressure into metal dies (or 'molds'). The dies are made of two or more parts called cavity or die halves. The main steps involved in the process are as follows:

1) The die halves are produced and mounted onto platens in the die casting machine, which hold the die sections together tightly.
2) The mold is prepared by brushing or spraying the mold with a refractory wash or coating.
3) Molten metal is injected into the die cavities, using pressure, where it chills rapidly.
4) When the metal has cooled, the dies are opened, and the still-hot casting is ejected.

5) Following ejection of the casting, other appropriate finishing steps follow (removal of gating, flash, surface machining, etc.)
6) The sequence is repeated until the required number of castings has been produced.

There are two main types of die casting processes: the hot chamber process and the cold chamber process, where the molten metal injection system connected to the shot chamber is either immersed in the molten bath or else the molten metal is held in a separate furnace and is introduced into the shot chamber just prior to casting.[85, 86] The great value of the die casting technique lies in its capacity for high production rates. Compared to processes such as forging and plastic injection molding, die castings can have more complex shapes and thinner sections, and closer dimensional tolerances; the castings are stronger, stiffer, more heat resistant and dimensionally stable, and far superior to plastics on a properties/coat basis. Compared with sand castings, die castings require much less machining; can be made with thinner walls; can have all or nearly all holes cored to size; have smoother surfaces, and can be held within much closer dimensional limits. Unlike sand castings, die castings do not require new cores for each casting, and involve much less labor/cost per casting. Likewise, die castings have the same advantages in comparison with permanent mold castings.[87, 88]

Low Pressure Die Casting (LPDC) Technique

In the die casting process, high pressure is normally used to inject the molten metal into the die cavity, hence the term 'high pressure die casting.' Another variation of the technique, the low pressure die casting or LPDC technique, uses a lower pressure (typically

0.3 to 1.5 bars), where the molten metal is forced upward into the die cavity which is held above the furnace. This method allows for an excellent compromise between quality, cost, productivity, and geometrical feasibility.

The principle of this process is quite simple: the permanent die and the filling system are placed over the furnace containing the molten alloy as shown in Figure 2.24. The filling of the cavity is obtained by forcing - by means of a pressurized gas - the molten metal to rise into a ceramic tube (termed *stalk*), which connects the die to the furnace. The pressure used is roughly equivalent to 2 meters of an aluminum column. Once the die cavity is filled, the overpressure in the furnace is removed, and the residual molten metal in the tube flows again towards the furnace. The various parts of the die are then separated, and the casting is finally extracted. Specific attention must be paid to the design of the die to control, by means of proper cooling circuits, the solidification path of the alloy. The massive region of the casting has to be the last one to solidify and must be placed near to the stalk, which acts as a “virtual” feeder and allows avoiding the use of conventional feeders, thus improving the yield of the process, which becomes significantly high. The low injection velocity and the relatively high cycle time lead to a good control of the fluid dynamics of the process, avoiding the defects originating from turbulence phenomena.[88-96]

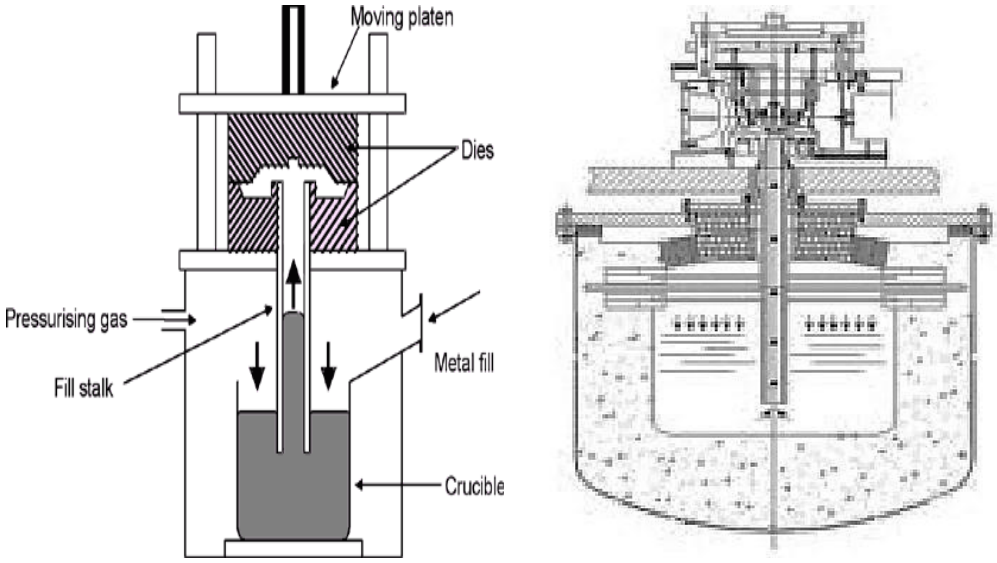

Figure 2.24 General scheme of the low pressure die casting process.[87, 88]

The low injection velocity and the relatively high cycle time lead to a good control of the fluid dynamics of the process, avoiding the defects originated by turbulence phenomena. Castings up to 70 kg weight can be produced, with tolerances of 0.3-0.6 %. The die can be designed for the production of a single casting or for multiple castings, according to the size required and to the characteristics of the machine.

The advantages of the low pressure die casting process are several:

1- The high yield achievable (typically over 90%).

2- The reduction of machining costs, due to the absence of feeders.

3- The excellent control of process parameters, which can be obtained, with a high degree of automation.

4- The good metallurgical quality, due to a homogeneous filling and controlled solidification dynamics, resulting in good mechanical and technological properties of the castings.[88, 90, 91, 96]

CHAPTER 3

EXPERIMENTAL PROCEDURES

CHAPTER 3

EXPERIMENTAL PROCEDURES

3.1 INTODUCTION

This chapter will provide all the details on the alloys that were prepared for this study, the melting and casting procedures, heat treatment procedures, preparation of samples for metallographic examination, and the mechanical testing procedures.

Alloy 220 with a composition of Al-2%Cu-1.32%Si-0.425Mg-0.58%Fe-0.59%Mn-0.07%Ti was used as the base alloy. Other alloys were prepared from this alloy by adding Sr, Ti, Zr, Ag, and Sc to the 220 alloy melts, individually or in different combinations, to produce twelve alloy compositions.

These alloys were coded 220A (base alloy), 220B, 220C, and so forth. Table 3.1 shows the details of the additions made in each case. One hundred test bars were cast from each of the alloys prepared, using the low pressure die casting technique. It should be noted here that, for the sake of brevity, the alloy codes used in the figures to be presented in Chapter 4 have been further abbreviated to A, B, C, etc.

Table 3.1 List of Al-2%Cu based alloys prepared for this study.

Code	Alloy	No. of tensile test bars prepared bars
220A	Base 220 alloy: Al-2%Cu-1.32%Si-0.42%Mg-0.58%Fe-0.59%Mn-0.07%Ti	100
220B	A + 0.02%Sr	100
220C	A + 0.15%Ti	100
220D	A + 0.15%Ti +0.02%Sr	100
220E	A + 0.15%Ti + 0.50%Zr	100
220F	A + 0.15%Ti + 0.30%Zr	100
220G	A + 0.15%Ti + 0.50%Zr + 0.70%Ag	100
220H	A + 0.15%Ti + 0.02%Sr + 0.50%Zr	100
220I	A + 0.15%Ti + 0.02%Sr + 0.50%Zr + 0.70%Ag	100
220J	A + 0.15%Ti + 0.30%Zr + 0.15%Sc	100
220K	A +0.15%Zr	100
220L	A +0.30 %Zr	100
220M	A +0.50 % Zr	100

Note: A: Base alloy 220A

3.2 ALLOY PREPARATION AND MELTING PROCEDURES

Alloy 220 was received in the form of ingots. The ingots were cut into small pieces, cleaned, dried and then melted in a 150 kg-capacity crucible, using an electrical resistance furnace as shown in Figure 3.1(a). The melting temperature was held at 740 ± 5°C. The molten metal was degassed for 15 minutes using pure dry argon injected into the molten metal (at a flow rate of 30 ft^3/hr) by means of a graphite rotary degassing impeller. The

degassing time/speed was kept constant at 30 min/150 rpm. Such a degassing process was used to minimize the hydrogen level of the melt, and to eliminate inclusions and oxides via flotation. After degassing, the molten metal surface was skimmed carefully to remove all the oxide layers and dross before pouring the melt into the ingot molds. Samplings for chemical analysis were also taken simultaneously for each alloy melt composition prepared. The ingots thus prepared were later remelted in the furnace shown in Figure 3.1(b) used for preparing melts for casting the LPDC test bars.

(a) (b)

Figure 3.1 Furnaces used for (a) preparing 220 alloys; and (b) remelting the alloys for LPDC casting.

3.3 CASTING PROCEDURES

Tensile test bar castings were prepared using the LPDC technique. The casting was carried out using the LPDC casting facilities at MTL-CANMET in Ottawa. Figure 3.2 shows photographs of a) the LPDC machine, b) the mold used to prepare the castings, and c) some of the LPDC castings produced.

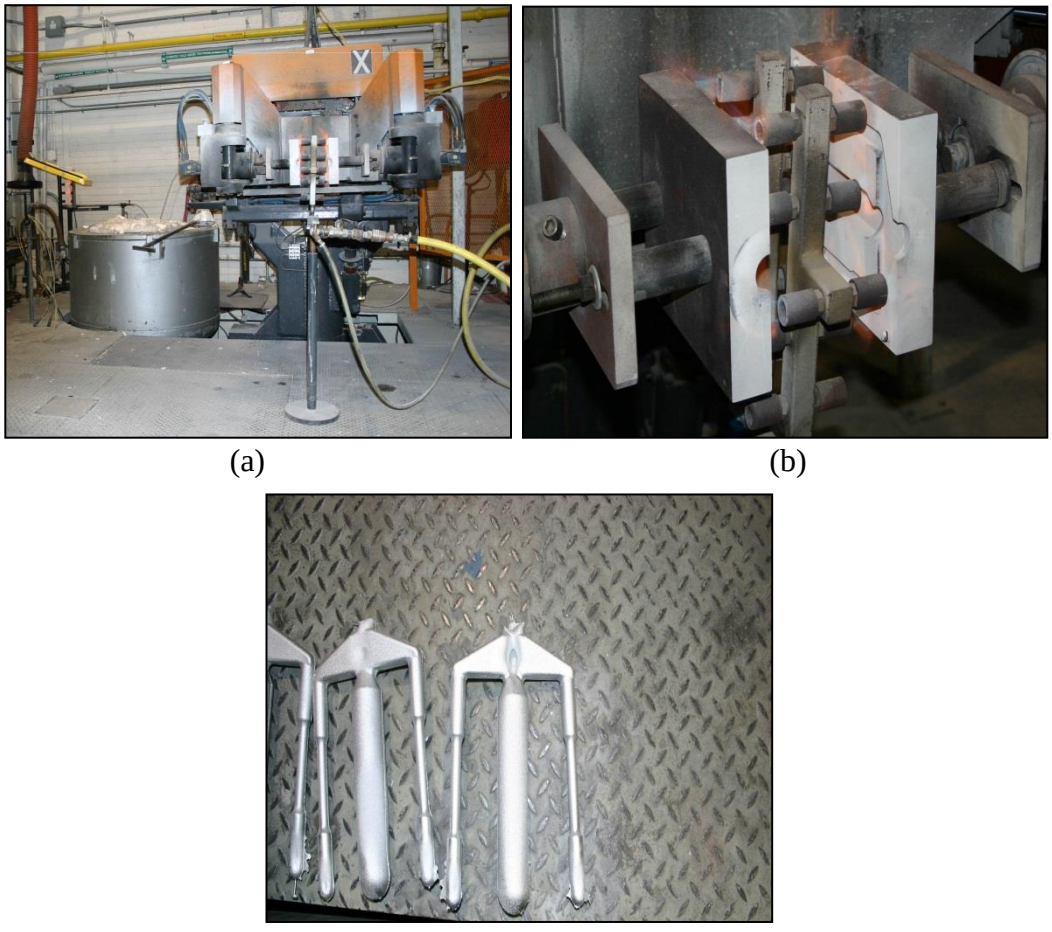

(a) (b)

(c)

Figure 3.2 Photographs of (a) LPDC machine, (b) mold used for casting and (c) LPDC castings.

One hundred test bars were cast per alloy composition. As mentioned previously, in this technique, the permanent die and the filling system are placed over the furnace containing the molten alloy. The cavity is filled by forcing the molten metal (using pressurized gas @ 0.3 to 1.5 bar) the molten metal to rise into a ceramic tube which connects the die to the furnace. Once the die cavity is filled, the overpressure in the furnace is removed, and the residual molten metal in the tube flows again into the furnace. The various parts of the die are then separated, and the casting extracted. The tensile test bars were subsequently cut from their castings with dimensions corresponding to ASTM dimensions, as shown in Figure 3.3. Table 3.2 shows the chemical composition of the alloys investigated in the current study.

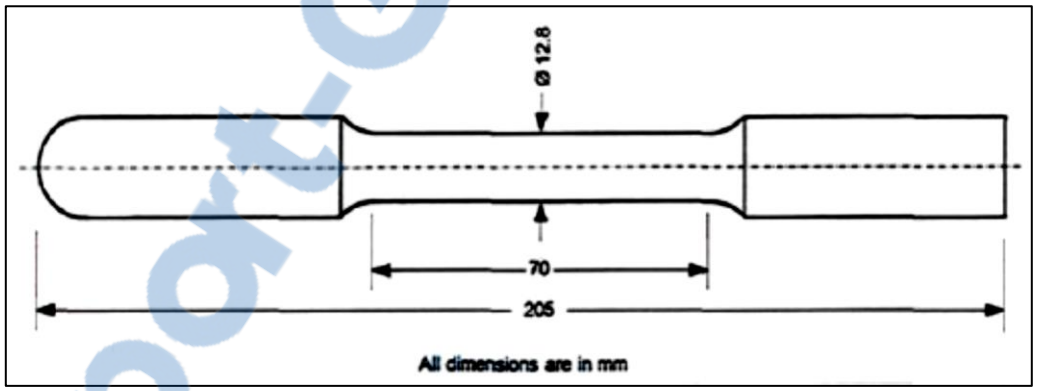

Figure 3.3 The tensile test bar dimensions (mm) as per ASTM specifications.

Table 3.2 Chemical composition of the alloys investigated in the current study.

Alloy Code	Chemical Composition (% wt)										
	Cu	**Si**	**Mg**	**Fe**	**Mn**	**Sr**	**Ti**	**Zr**	**Sc**	**Ag**	**Al**
220A	2.28	1.28	0.36	0.39	0.61	0.00	0.04	0.00	0.00	0.00	bal.
220B	2.35	1.21	0.35	0.40	0.60	0.02	0.07	0.00	0.00	0.00	bal.
220C	2.36	1.13	0.35	0.39	0.60	0.00	0.23	0.00	0.00	0.00	bal.
220D	1.87	0.98	0.23	0.53	0.53	0.017	0.19	0.00	0.00	0.00	bal.
220E	2.32	1.16	0.34	0.40	0.62	0.00	0.14	0.36	0.00	0.00	bal.
220F	2.32	1.12	0.37	0.36	0.59	0.00	0.21	0.27	0.00	0.00	bal.
220G	2.29	1.09	0.33	0.37	0.57	0.00	0.21	0.36	0.00	0.51	bal.
220H	1.91	1.00	0.32	0.56	0.56	0.015	0.12	0.65	0.00	0.00	bal.
220I	1.91	1.00	0.31	0.54	0.54	0.016	0.18	0.35	0.00	0.55	bal.
220J	1.40	0.81	0.26	0.41	0.41	0.00	0.11	0.13	0.15	0.00	bal.
220K	2.06	1.15	0.35	0.52	0.57	0.00	0.13	0.14	0.00	0.00	bal.
220L	2.07	1.11	0.34	0.51	0.57	0.00	0.14	0.26	0.00	0.00	bal.
220M	2.08	1.10	0.34	0.51	0.58	0.00	0.11	0.47	0.00	0.00	bal.

For hardness testing, castings were prepared using the L-shaped rectangular graphite-coated metallic molds shown in Figure 3.4(a), to obtain castings of the type shown in Figure 3.4(b). Hardness test bars were subsequently cut from these castings and further machined to final dimensions of 35 x 30 x 80 mm.

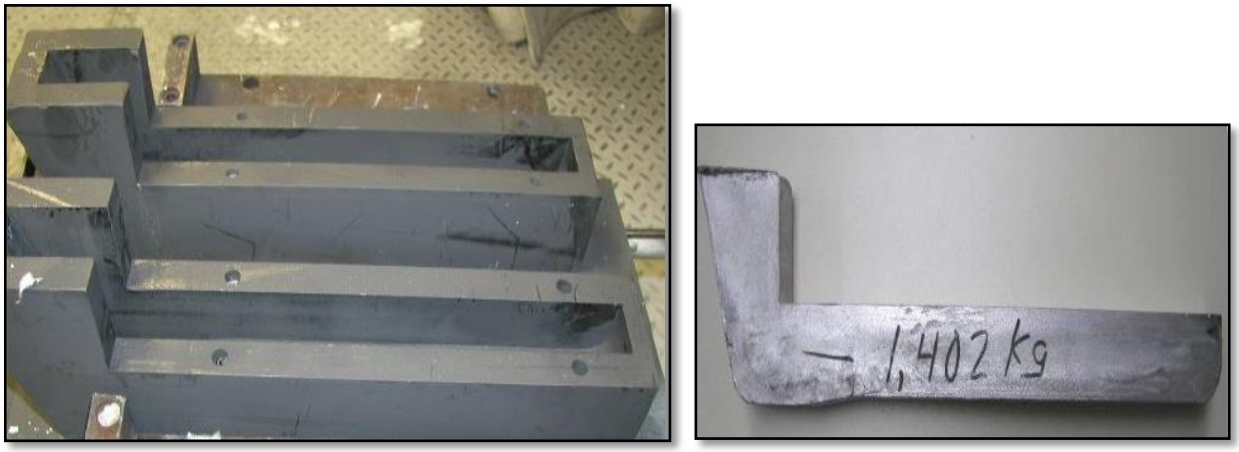

(a) (b)

Figure 3.4 (a) L-shaped metallic molds, (b) casting used for sectioning hardness test bars.

3.4 HEAT TREATMENT PROCEDURES

The as-cast test bars were subjected to T6 heat treatment which consisted of (a) solution heat treatment at 490°C for 8 hrs, followed by (b) quenching in warm water, and then (c) artificial aging at temperatures of 155, 180, 200, 220, 240 and 300°C for 5 hrs at each temperature. The Blue M forced air furnace shown in Figure 3.5 was used for carrying out both the solution and aging treatments.

Figure 3.5 Blue M furnace used for heat treatment.

3.5 METALLOGRAPHY

Samples were sectioned from as-cast and heat-treated tensile-tested bars for metallographic examination. The samples were mounted in bakelite, ground, and polished to a fine finish, using standard polishing procedures. The polished samples were examined using an optical microscope-image analyzer system. The set-up is shown in Figure 3.6. The volume fraction of intermetallic phases in these samples was determined using an electron microprobe analyzer.

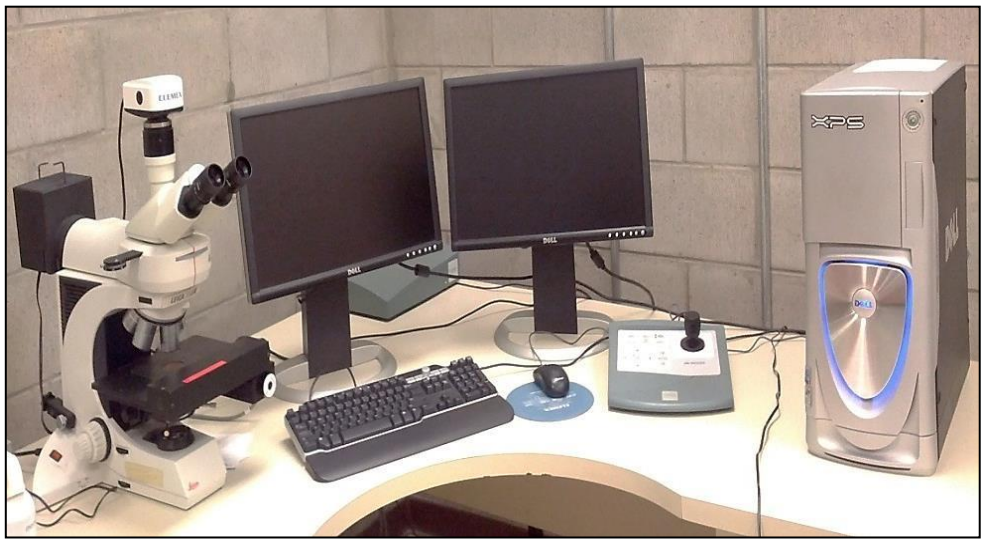

Figure 3.6 Optical microscope-Clemex image analyzer system.

3.6 MECHANICAL TESTING

The mechanical properties examined in this study were the hardness and tensile properties. A full description of the castings prepared for these tests and details of the test samples sectioned from the respective castings have been provided in section 3.3.

Hardness Testing

Hardness is the property of a material that enables it to resist plastic deformation when subjected to indentation by means of a load applied to the indentation device of a hardness tester. The term hardness also refers to resistance to bending, scratching, abrasion or cutting.

Hardness measurements were carried out on the hardness test bars prepared for this purpose using a Brinell Hardness tester, as shown in Figure 3.7. All measurements were

carried out using a steel ball of 10 mm diameter and a load of 500 kg applied for 30 seconds, causing a round indentation in the test block. As the schematic diagram of Figure 3.8 [97] Shows, the Brinell Harness number (BHN) equation with an explanation diagram, the BHN is calculated by dividing the load applied (F) by the surface area of the indentation (where D is the diameter of the indenter, and D_i the diameter of the indentation), which is inversely proportional to the block hardness. An average of eight readings obtained from two perpendicular surfaces was taken to represent the hardness value of each alloy/condition.

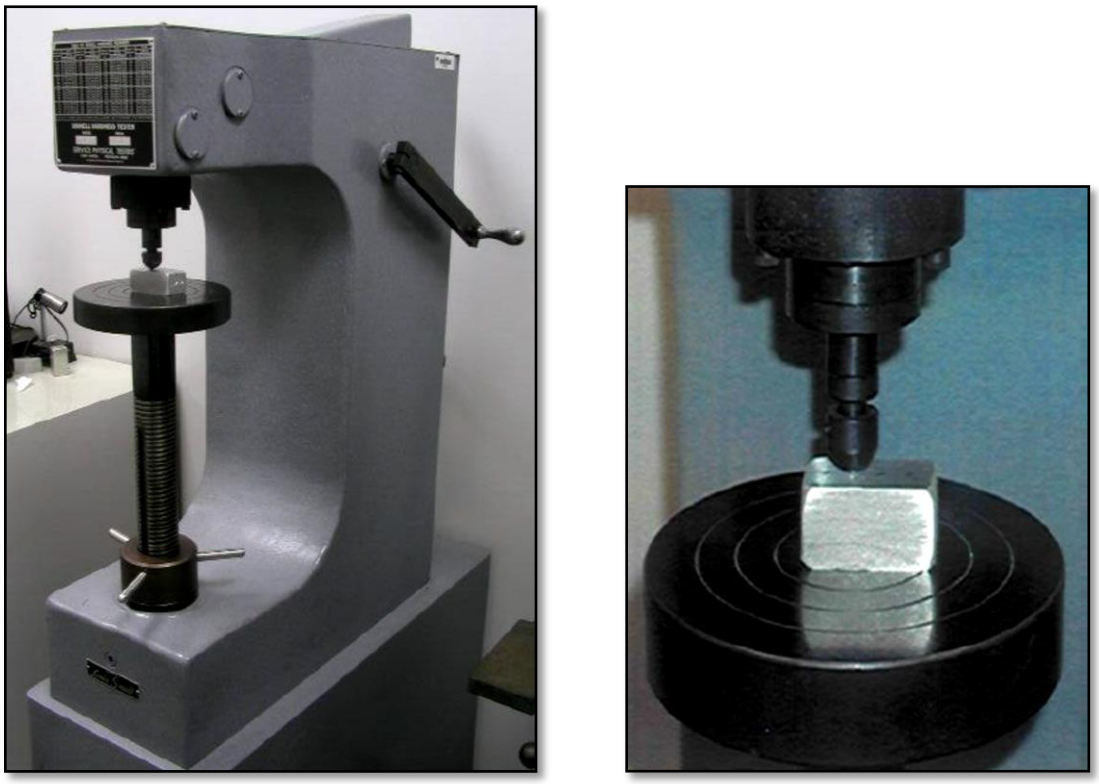

(a) (b)

Figure 3.7 (a) Brinell Hardness tester; (b) Hardness measurement of the test blocks.

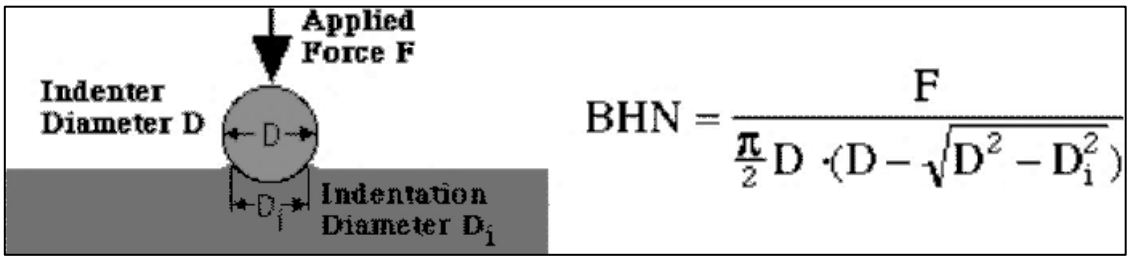

Figure 3.8 The Brinell Hardness number (BHN) equation, along with an explanation diagram.[97]

Tensile Testing

The test bars were tested at room temperature in the as-cast and T6 heat-treated conditions using an MTS Servohydraulic Mechanical Testing Machine, as shown in Figure 3.9(a). A data acquisition system attached to the machine provided the tensile test data. The test bars were pulled to fracture at room temperature at a strain rate of 4×10^{-4}/s. A strain gauge extensometer was attached to the test bar to measure percent elongation as the load was applied. The yield strength (YS) was calculated according to the standard 0.2% offset strain, and the fracture elongation was calculated as the percent elongation (%El) over the 50 mm gauge length of the test bar. The ultimate tensile strength (UTS) was also obtained from the data acquisition system of the MTS machine, as shown in Figure 3.9(b). The machine was calibrated each time before any testing was carried out.

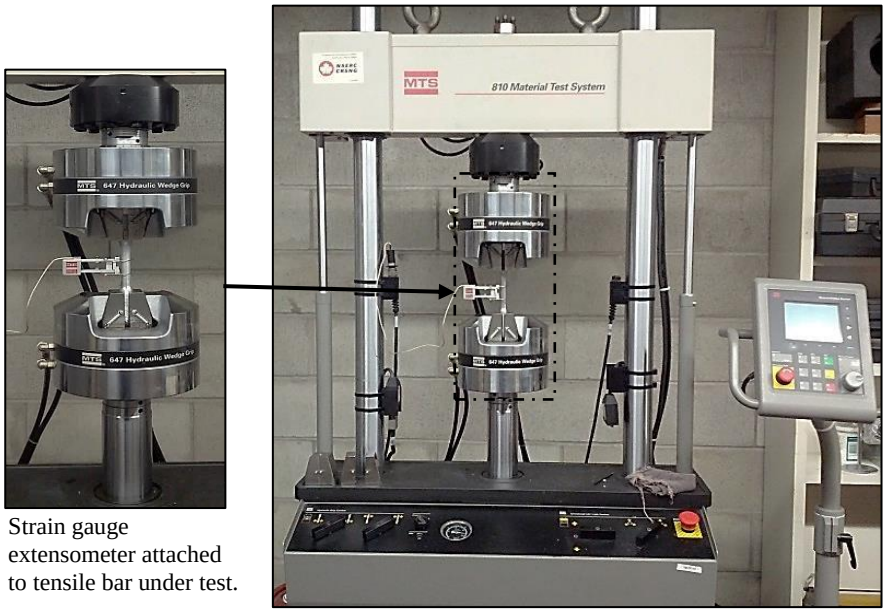

Strain gauge extensometer attached to tensile bar under test.

(a)

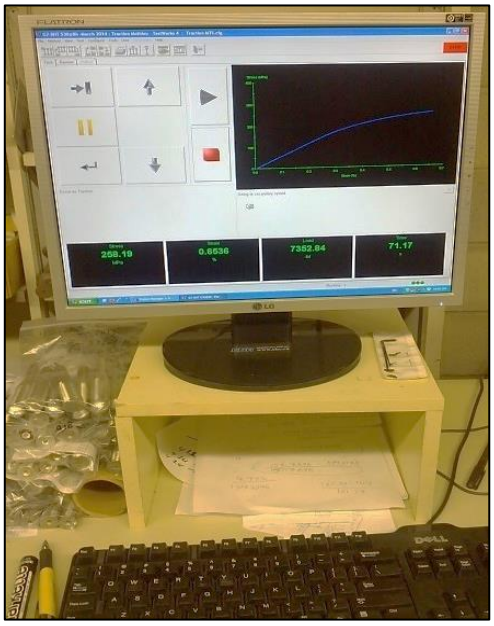

(b)

Figure 3.9 (a) Servohydraulic MTS mechanical testing machine; (b) Data-acquisition system of the MTS machine.

CHAPTER 4

RESULTS AND DISCUSSION

CHAPTER 4

RESULTS AND DISCUSSION

4.1 INTRODUCTION

Mechanical properties are an important measure of product quality, and hardness measurements and tensile tests are commonly used to determine the mechanical properties of an alloy casting. Hardness of a material is a measure of its resistance to plastic deformation, whereas tensile properties measure the strength of a material and its ability to resist loads without failure, that is, a measure of its ductility. For samples pulled in tension at a constant rate, the tensile properties measured are the ultimate tensile strength (UTS), the yield strength (YS) at 0.2% offset strain, and the elongation to fracture or percent elongation (%El).

As mentioned previously in Chapter 2, the concept of quality index (Q) was introduced by Drouzy *et al.*[77, 78] and expanded upon by Caceres and others[79, 80] to provide a better understanding of the tensile properties and includes Al-Si-Cu and Al-Si-Mg-Cu alloys in addition to the Al-7%Si-Mg alloys investigated by Drouzy *et al.*

Based on this concept, quality charts can be constructed which plot the tensile properties for a given alloy subjected to different aging treatments. Plotting the properties on a chart constructed of *iso-YS* and *iso-Q* or *iso-flow and iso-q* lines facilitates the process of determining the optimal aging conditions (temperature and time) to improve the alloy quality and for adjusting these conditions to achieve the required strength-ductility combination desired for a specific application.

The mechanical properties of a casting are initially determined by the microstructure obtained upon solidification (as-cast condition), and may be improved thereafter by subjecting the casting to a suitable heat treatment process and following the evolution of the microstructure in order to optimize the heat treatment conditions. An examination of the microstructure allows determination of the constituent phases present in the solidified structure, as well as the phases and precipitates that form following heat treatment. The alloy properties may then be analyzed in terms of the corresponding microstructures.

This chapter will present the hardness and tensile test data for the Al-2%Cu based 220 alloys studied. The data will be analyzed and discussed with respect to the corresponding macro- and microstructures obtained based on the alloying additions made to the respective alloys. The alloy properties will also be examined in terms of quality charts constructed from the experimental data as well as statistically analyzed using Minitab software.

4.2 MICROSTRUCTURAL EXAMINATION

The thirteen alloys used in this study were divided into four different groups defined by the additions made to the base alloy, as shown below in Table 4.1, with a view to examining their effects individually or in combination with the other additives in the group. The actual additions and addition levels made for each alloy are listed in Table 4.2.

Table 4.1 Division of 220 alloys into groups

Group	Alloys
Base Alloy	220A
Group I (Ti-Sr)	220B, 220C, 220D
Group II (Zr-Ti-Ag)	220E, 220F, 220G
Group III (Zr-Ag-Sc)	220H, 220I, 220J
Group IV (Zr)	220K, 220L, 220M

It is to be mentioned here that, dividing the alloys into four groups of three alloys each also facilitated plotting the alloy properties in the aged condition without crowding the graphs.

Figure 4.1 shows examples of the microstructure of the base alloy 220A and those of alloys 220D and 220I. In all cases the α-Al dendrites may be clearly observed, outlined by the secondary phases present in the interdendritic regions. Compared to the base alloy which exhibits elongated dendrites in general, the dendrites in Alloy D and Alloy I appear to be more equiaxed or rounded in nature. This is to be expected, since the two alloys respectively contain Ti and Zr which are well known for their grain refining action. In Figure 4.1(c), the presence of Al_3Zr particles (arrowed) is noted.

The grain refining effect of these additives may be seen more clearly in the macrostructures of etched samples of these alloys as shown in Figure 4.2. It is interesting to note the increase in the level of refinement on going from Alloy D to Alloys G, H and I as more grain refiners are added. The fineness of the microstructure is reflected by the secondary dendrite arm spacing (SDAS), so that the finer the microstructure obtained, the smaller the average SDAS value exhibited by the solidified alloy sample. It is well known that SDAS has a strong influence on the mechanical properties of cast aluminum alloys.[98]

Grain size measurements were carried out for all the alloys investigated. For these measurements, etched samples were examined using the optical microscope-Clemex image analyzer system, and the linear intercept method was employed to determine the average grain size in each case. Table 4.3 lists the average grain sizes obtained for the 220 alloys studied. The grain refining effect of the different additives will be further elaborated upon in the discussion of the tensile properties in later sections.

Besides the effect of the grain refiner additions, it is also important to know the type and amounts of intermetallic and other phases formed in these alloys as a result of these additions, as they will also affect the resultant alloy properties. The additives may interact with each other and with the alloying elements present in the alloy to produce various phases depending on the melt and solidification conditions. Some of these interactions may have a deleterious effect on the resultant properties. For example, the presence of Sr in Al-Si-Cu based alloys is known to create an increase in porosity and also cause segregation of the copper phases in the interdendritic regions so that the phase is much harder to dissolve during solution heat treatment, and so forth. On the other hand, Sr

is also known to cause the fragmentation and dissolution of the brittle platelet-like β-Fe intermetallic phase whose presence is known to cause feeding problems during solidification and result in porosity formation, as well as reduce the mechanical properties.[99] Therefore, an examination of the phases formed in the 220 alloys containing the various additives used in our study will be very helpful in understanding the tensile and hardness properties that were determined for these alloys.

In order to observe and identify the various phases formed, the alloy samples were examined using an electron microprobe analyzer equipped with EDX and WDS facilities for phase identification purposes. Backscattered electron (BSE) images of the samples clearly revealed the phases appearing in the solidified microstructure of the corresponding alloys, while EDX spectra and X-ray maps of phase particles of interest helped to establish the elements present in these particles.

Table 4.2 List of the various 220 Al-2%Cu based alloys used in the present study and alloy chemistry

Group	Alloy Code	Alloy Chemistry
Base Alloy	220A	220 alloy:Al-2%Cu-1.32%Si-0.42%Mg-0.58%Fe-0.59%Mn-0.07%Ti
Group I Ti-Sr	220B	220A + 0.02%Sr
	220C	220A + 0.15%Ti
	220D	220A + 0.15%Ti + 0.02%Sr
Group II Zr-Ti-Ag	220E	220A + 0.15%Ti + 0.50%Zr
	220F	220A + 0.15%Ti + 0.30%Zr
	220G	220A+ 0.15%Ti + 0.50%Zr + 0.70%Ag
Group III Zr-Ag-Sc	220H	220A+ 0.15%Ti + 0.02%Sr + 0.50%Zr
	220I	220A+ 0.15%Ti + 0.02%Sr + 0.50%Zr + 0.70%Ag
	220J	220A+ 0.15%Ti + 0.30%Zr + 0.15%Sc
Group IV Zr	220K	220A+ 0.15%Zr
	220L	220A+ 0.30%Zr
	220M	220A+ 0.50%Zr

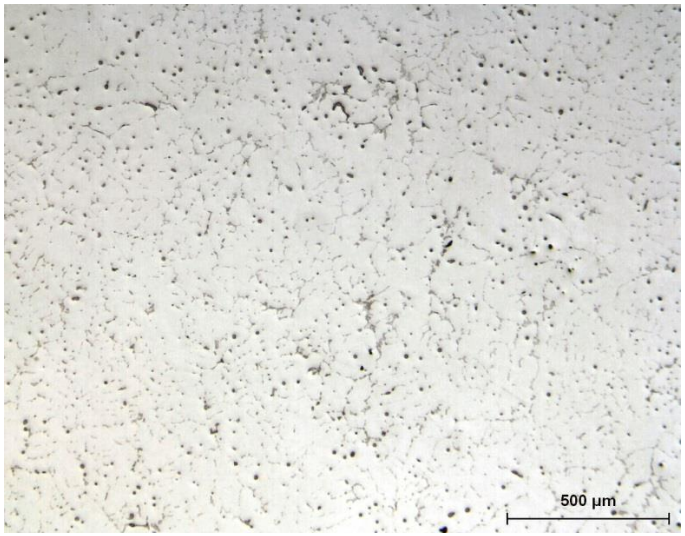

(a)

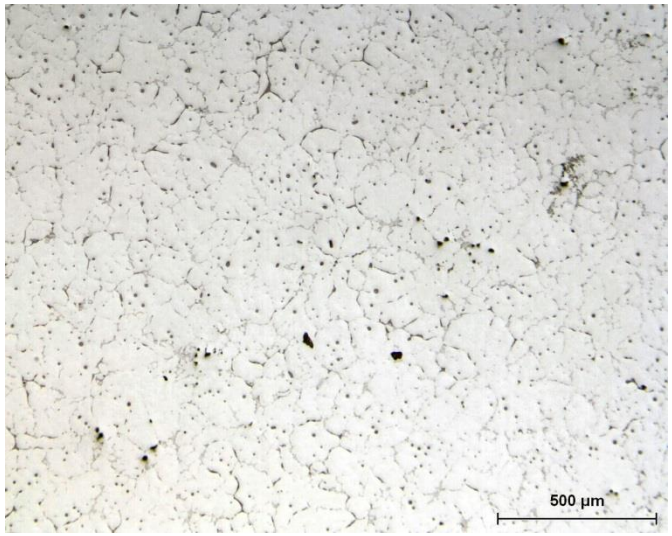

(b)

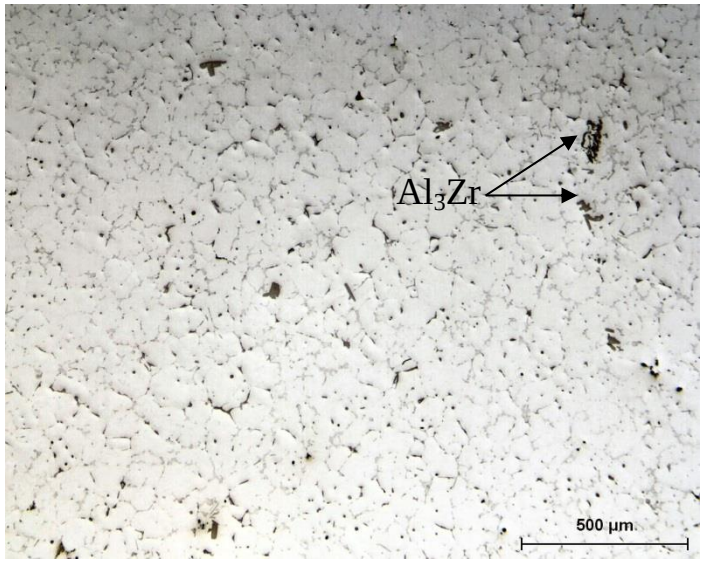

(c)

Figure 4.1 Optical micrographs showing the microstructures of (a) Alloy 220A, (b) Alloy 220D, and (c) Alloy 220I.

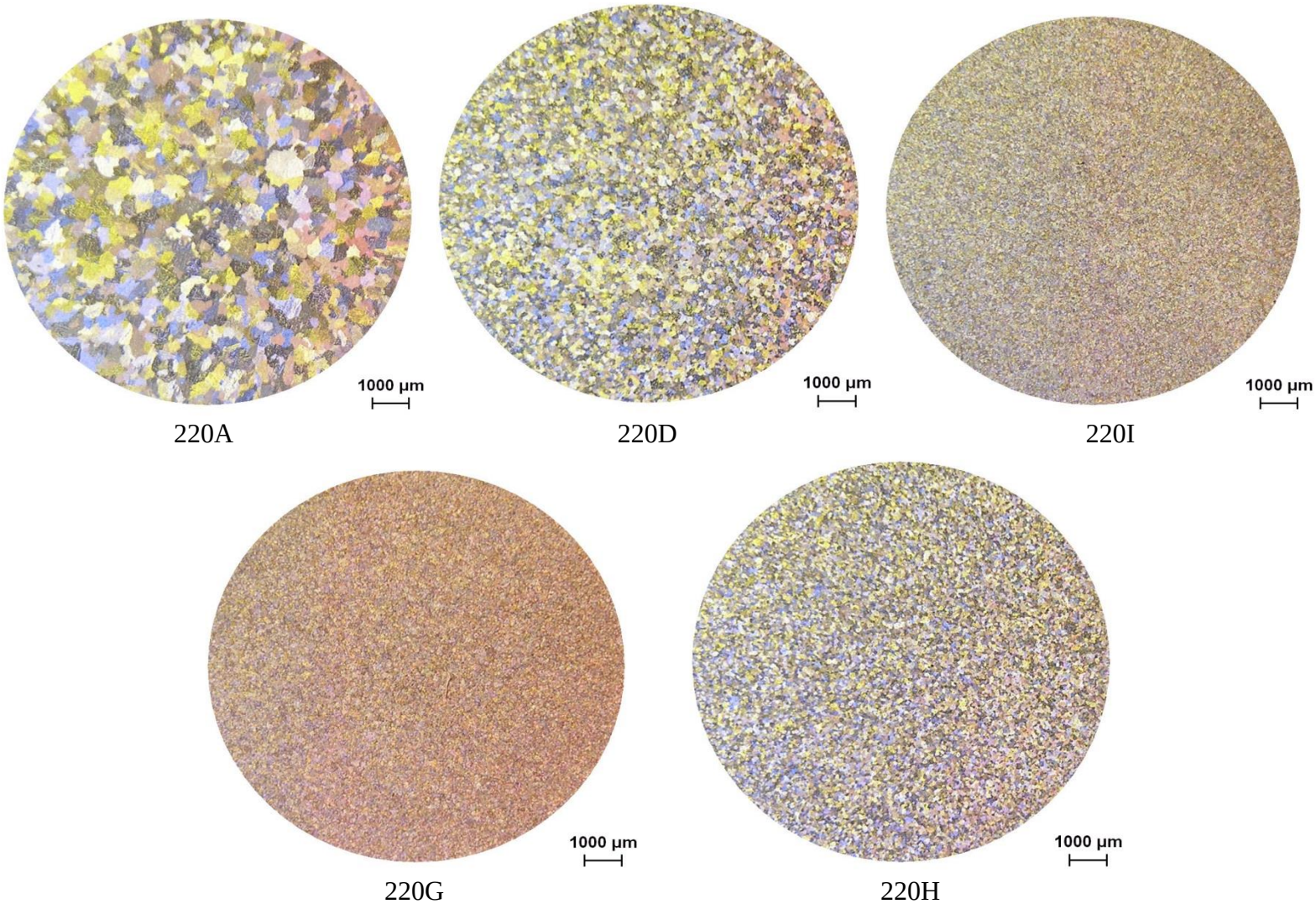

Figure 4.2 Macrostructures comparing the grain size of alloys 220A, 220D, 220I, 220G and 220H.

Table 4.3 Average grain size of the different 220 alloys studied

Alloy Code	Av. Grain Size (μm)	Additives (wt%)
220A	434	Base alloy
220B	422	0.02 Sr
220C	142	0.15 Ti
220D	177	0.15 Ti + 0.02 Sr
220E	143	0.15 Ti + 0.50 Zr
220F	122	0.15 Ti + 0.30 Zr
220G	190	0.15 Ti + 0.50 Zr + 0.70 Ag
220H	144	0.15 Ti + 0.50 Zr + 0.02 Sr
220I	130	0.15 Ti + 0.50 Zr + 0.70 Ag + 0.02 Sr
220J	56	0.15 Ti + 0.30 Zr + 0.15 Sc
220K	300	0.15 Zr
220L	132	0.30 Zr
220M	76	0.50 Zr

Figure 4.3 shows representative examples of the BSE images obtained from alloys corresponding to the different groups. The base alloy, depicted in Fig. 4.3(a), shows intermetallic phases and Cu-phases (bright particles) distributed more or less evenly over the matrix surface. The Fe:Mn ratio of the 220 alloy leads to the formation of the script-like α-Fe intermetallic phase rather than the β-Fe platelet or needle-like iron phase.[100] When Sr is added to the base alloy, i.e., alloy 220B, the presence of Sr leads to the segregation of the Cu-phase in regions away from the other phases, as may be observed in Fig. 4.3(b), so that the Cu-phase tends to precipitate in block-like form rather than the finer eutectic-like form observed in the base alloy. The combined addition of Ti and Sr appears to further refine the intermetallic phases, as seen in the BSE image of Alloy 220D shown in Fig. 4.3(c).

The presence of Ti, Zr and Ag in Alloy G lead to the appearance of blocky rectangular shaped bright particles mostly found within the α-Al dendrites or across two dendrites, as shown in Fig. 4.3(d). Sometimes these particles appear as needles, crossed over each other. The copper and intermetallic phases appear in the interdendritic regions, as in the case of other samples.

Alloy 220H which also contains the same levels of Ti and Zr as Alloy G, but 0.02%Sr instead of 0.7%Ag, also depicts a number of white particles; however, many of them appear as thin needles, situated along the dendrite boundaries or at times within the dendrites, as displayed in Fig. 4.3(e). Other irregular shaped thicker particles are also observed in the microstructure. These particles are not as bright as those observed in the case of Alloy G. Figure 4.3(f), corresponding to Alloy 220I, which contains the same Ti, Sr and Zr additions as Alloy H and 0.7% Ag in addition, shows a matrix covered with fine micro-constituents all over the surface. The great refinement of the microstructure is clearly noted when compared to that of the other alloys shown in Fig. 4.3.

Table 4.4 lists the total volume fraction of intermetallic phases observed in the 220 alloy samples. The average total volume fraction varies from 2.91 to 5.97 depending on the alloy and the additives it contains.

Table 4.4 Total volume fraction of intermetallics observed in the 220 as-cast alloy samples

Alloy	**A**	**B**	**C**	**D**	**E**
Average	3.98	3.91	3.69	2.91	5.74
Std Dev.	0.42	0.44	0.02	0.31	0.9
Alloy	**F**	**G**	**H**	**I**	**J**
Average	4.87	3.88	5.17	3.89	5.97
Std Dev.	0.65	0.45	0.59	1.04	0.6

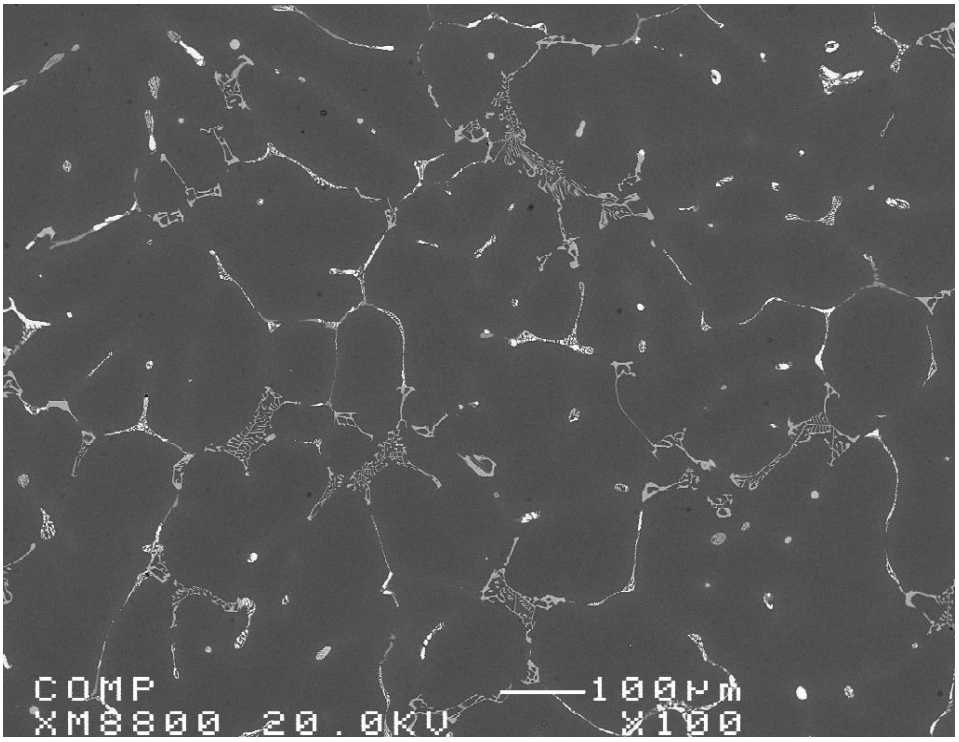

(a) Alloy 220A

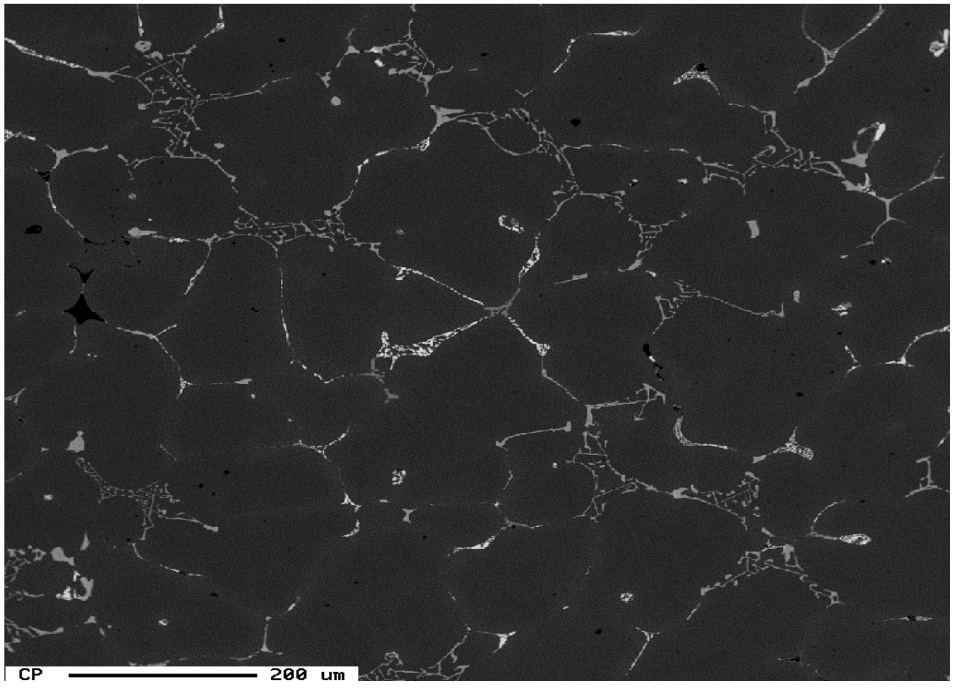

(b) Alloy 220B

Figure 4.3

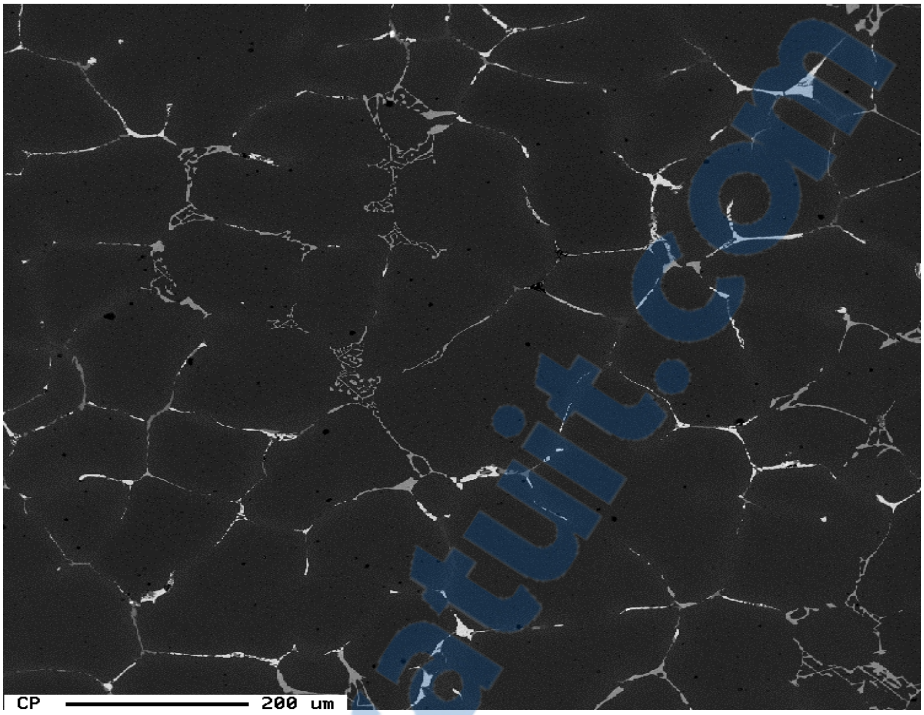

(c) Alloy 220D

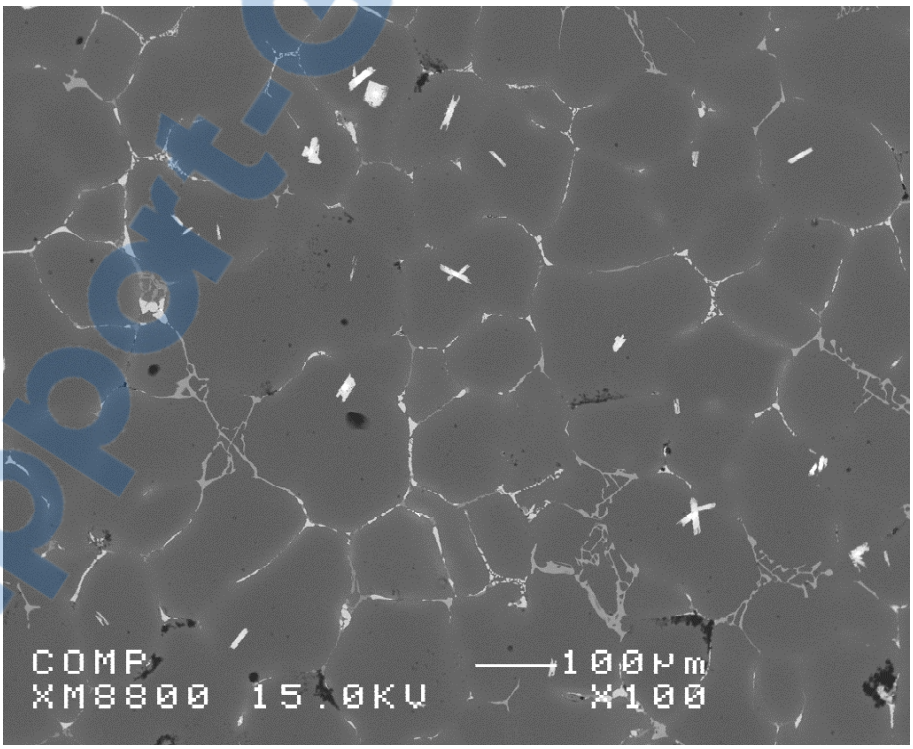

(d) Alloy 220G

Figure 4.3

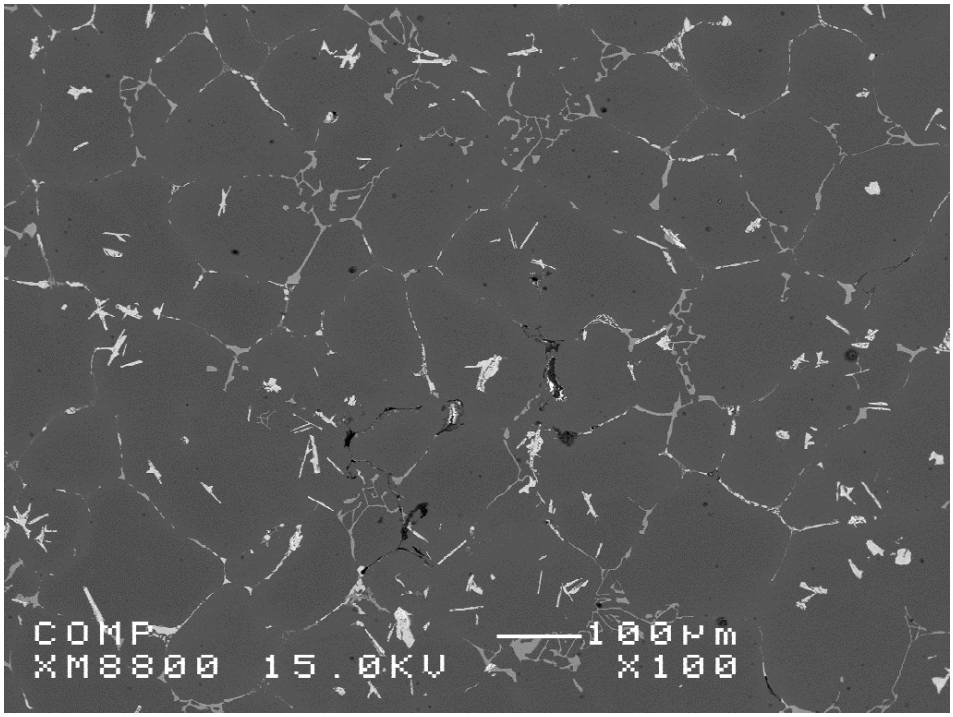

(e) Alloy 220H

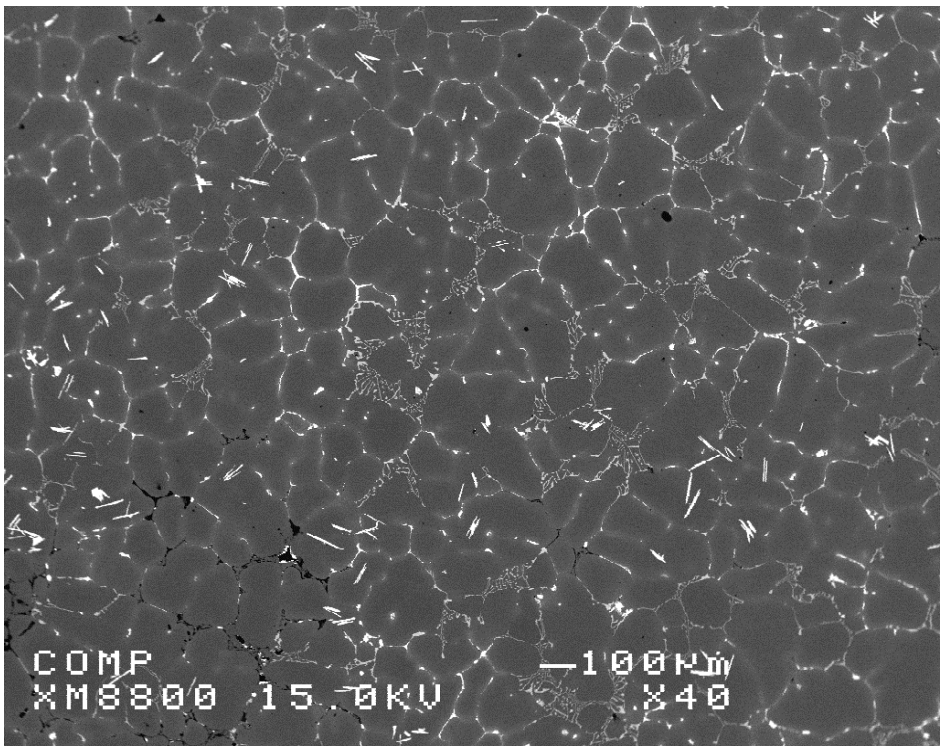

(f) Alloy 220I

Figure 4.3 (a-f) Backscattered electron images obtained from various 220 alloy samples.

Apart from the usual phases observed in the 220 base alloy, namely the α-Al dendrites, the α-Fe script phase and the Al_2Cu copper phase, other new phases of interest which stood out in the matrix were examined using the electron microprobe analyzer and associated EDX, X-ray imaging, X-ray mapping and WDS facilities to determine the elements constituting these phases. Some examples of interest are described below.

The backscattered electron image of the Alloy 220F sample which contains 0.15% Ti and 0.3% Zr is shown in Figure 4.4(a). X-ray images of the bright star-like particles shown in Figures 4.4(b) through 4.4(d) showed that these particles contain Ti, Si and Zr in addition to Al. Alloy 220E which contains the same two additives but a higher level of Zr (0.5%) shows the presence of bright irregular-shaped particles, Figure 4.5(a), that are larger in size than the star-like particles observed in the case of Alloy 220F.

The particle entity observed at the bottom left corner in Fig. 4.5(a), when observed at a much higher magnification, Fig. 4.5(b), revealed that it consisted of two phases – a medium grey phase with a lighter greyish-white phase situated in the centre. X-ray imaging showed the former to correspond to an Al-Si-Ti-Zr phase, while the brighter particles in the centre corresponded to an Al-Zr or more precisely, the Al_3Zr phase. The EDX spectra obtained from the two phases confirmed these results, as shown in Figure 4.6.

Figure 4.7 shows a composite of the BSE image taken from the 220I alloy sample and the corresponding X-ray maps for Si, Al and Ti. The bright crossed needle-shaped particles correspond to the Al_3Ti phase, while the iron phases (containing Si) appear in the interdendritic regions. The silver is distributed throughout the matrix, but more concentrated along the dendrite cell boundaries.

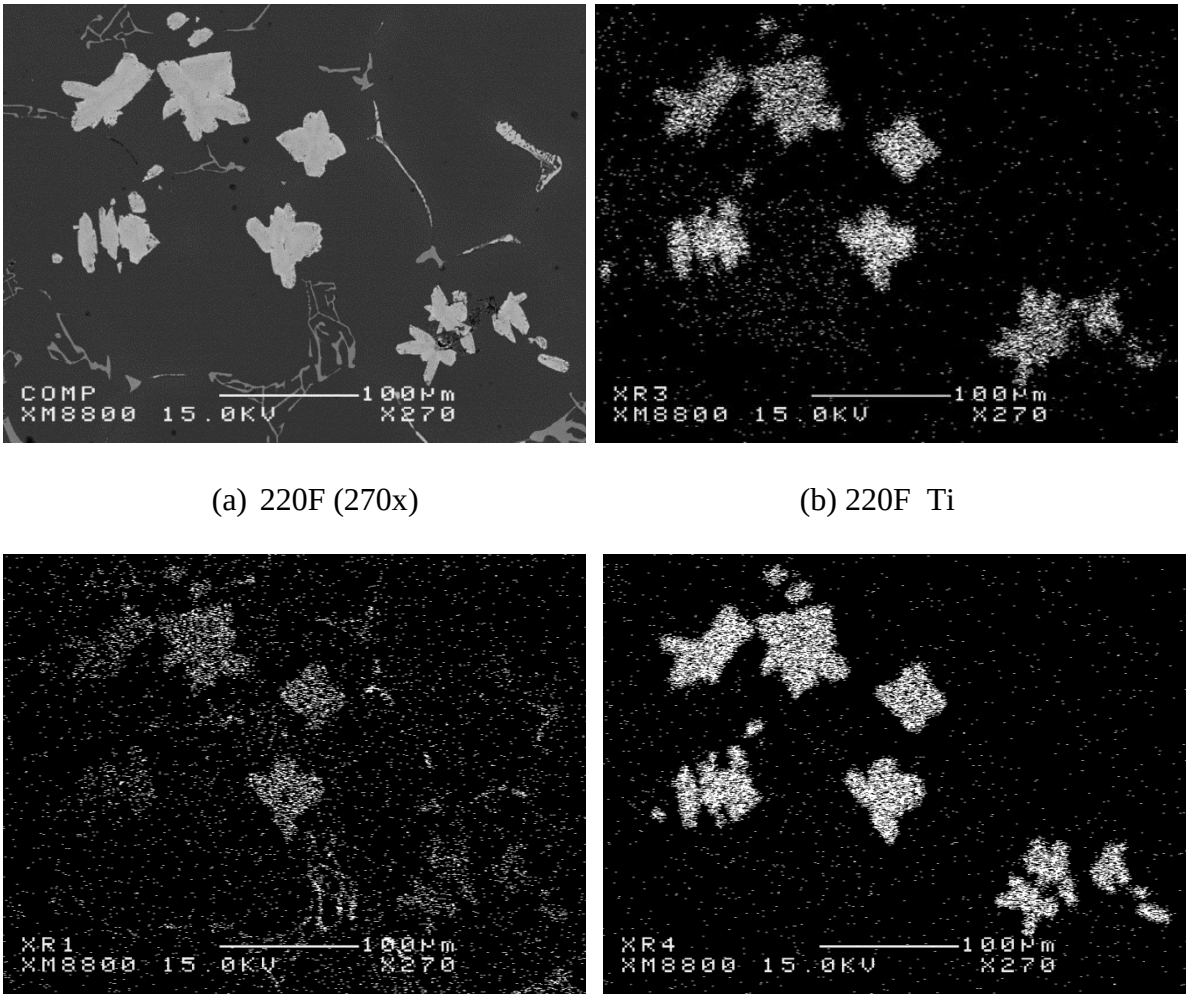

(a) 220F (270x) (b) 220F Ti

(c) 220F Si (d) 220F Zr

Figure 4.4 (a) BSE image of 220F alloy sample taken at 270x magnification, and corresponding X-ray images of (b-d) Ti, Si and Zr.

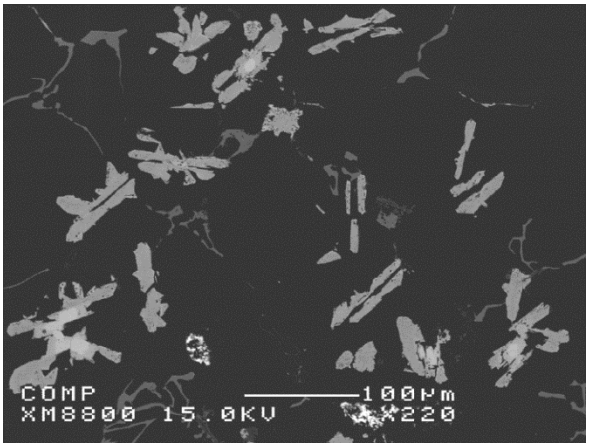

(a) 220E 220X

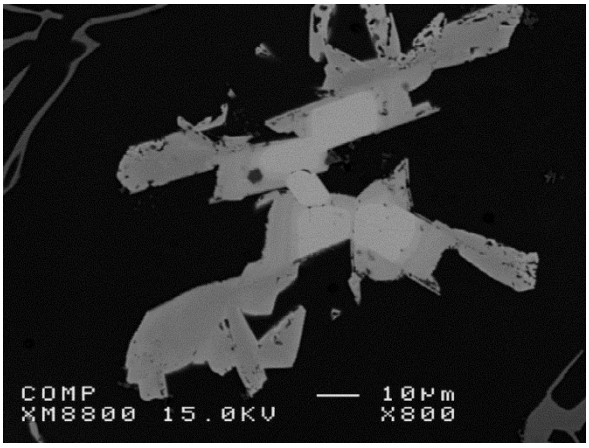

(b) 220E 800X

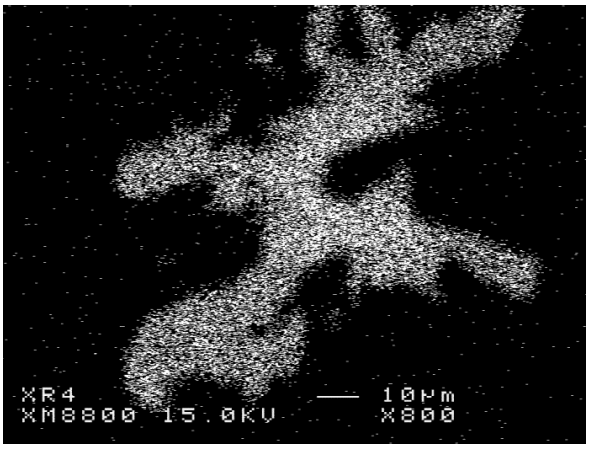

(c) 220E Zr

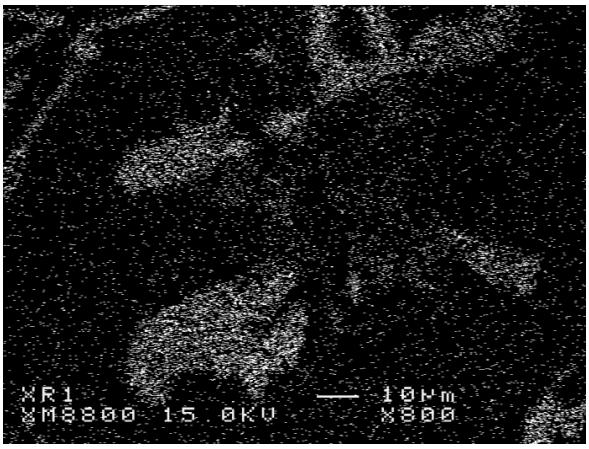

(d) 220E Si

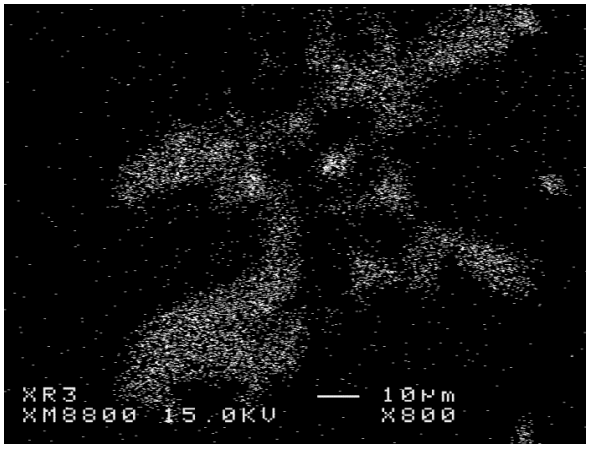

(e) 220E Ti

Figure 4.5 BSE images of 220E alloy sample taken at (a) 220x, and (b) 800x magnification, and (c-e) corresponding X-ray images of Zr, Si and Ti.

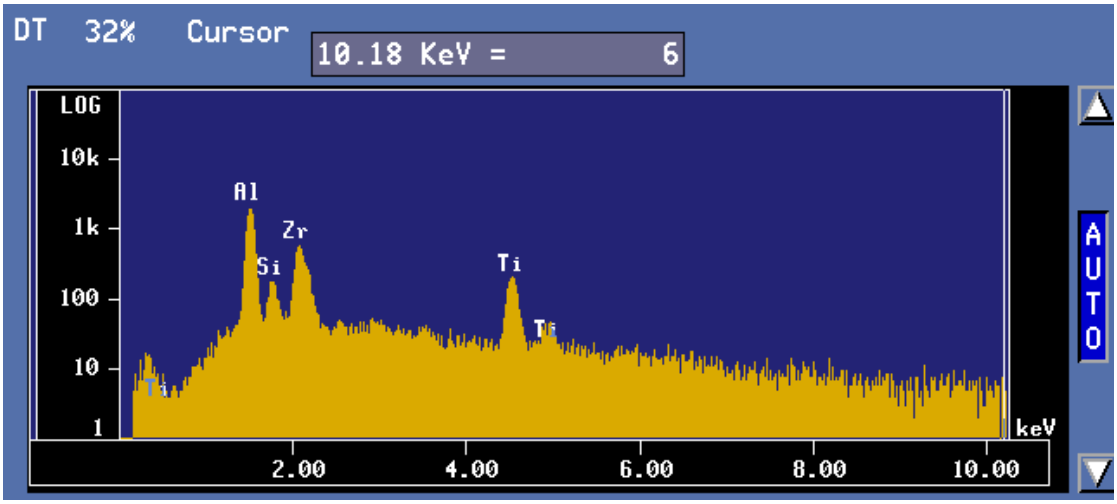

(a)

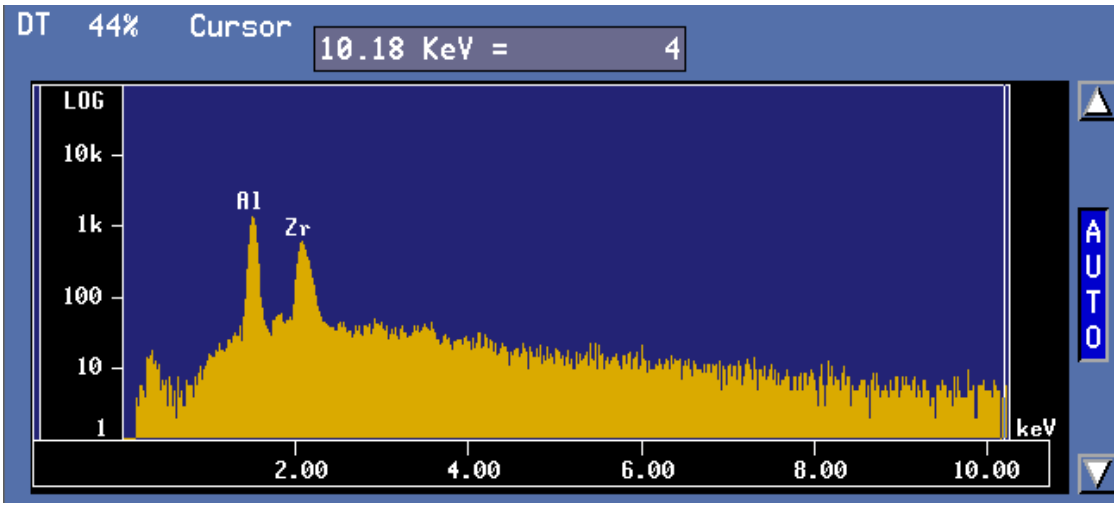

(b)

Figure 4.6 EDX spectra corresponding to (a) the medium grey, and (b) the light grey particles observed in the BSE image of the 220E alloy sample shown in Fig. 4.5(b).

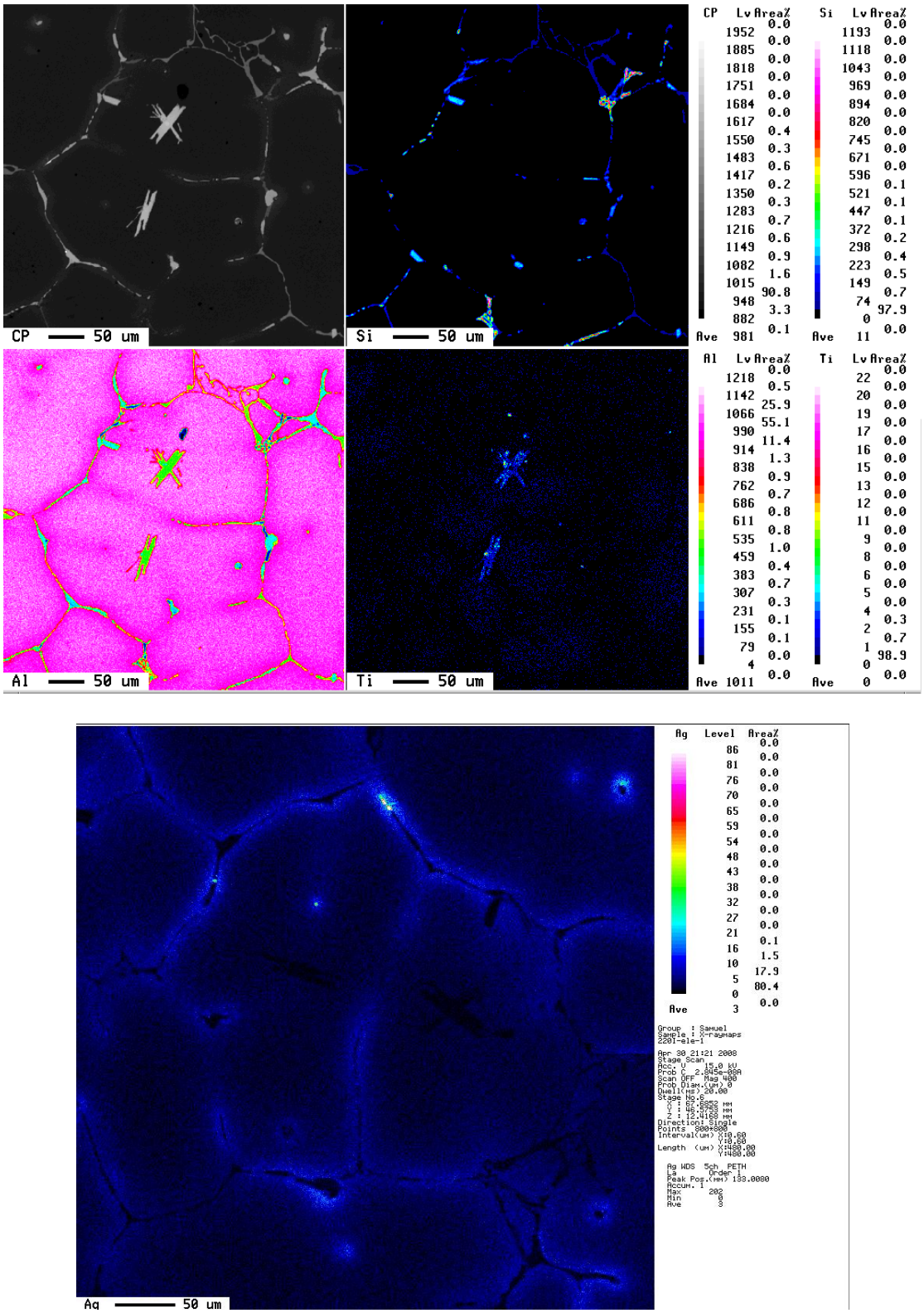

Figure 4.7 BSE image of 220I alloy sample and X-ray mapping of Si, Al, Ti and Ag.

4.3 EFFECTS OF ADDITIVES ON THE HARDNESS AND TENSILE PROPERTIES

The effects of Sr, Ti, Zr, Ag, and Sc alloying element additions to the base 220 alloy, individually or in different combinations, on the mechanical properties are examined and discussed in this section. The hardness and tensile test data is presented for the as-cast, solution heat-treated (SHT) and T6-aged conditions. The 13 alloys used in this study were divided into four groups, based on the additives used. Table 4.2 lists the additions and addition levels that were made in each case.

4.3.1 Hardness Test Results

Figure 4.8 illustrates the variation in hardness of the Al-2%Cu based alloys, as a function of as-cast and solution heat-treated (SHT) conditions. It may be observed that in the as-cast condition, the highest hardness values are obtained for alloys 220H and 220M, namely, 83.5 and 86.1 BHN, respectively. Compared to a hardness value of 78.7 BHN for the base alloy 220A, those observed for the other alloys are more or less similar, within ~6 BHN, depending on the alloying element additions made in each case. It can also be observed that all alloys show an improvement in hardness of ~18% after solution heat treatment.

Maximum hardness is observed in the case of alloy 220H which displays a hardness of ~94.5 BHN. Comparatively speaking, however, alloys C, F, and I which show the lowest hardness values in the as-cast condition, are the ones which show maximum improvement in hardness after solution heat treatment. This indicates that the 220 alloys, in the presence

of grain refining elements (Ti, Zr) as 0.15%Ti alone or in combination with Zr (0.3% or 0.5%) has the greatest response to solution heat treatment. These three alloys display grain sizes in the same range (see Table 4.3). Thus it is reasonable to assume that they will show the same response to hardening. The presence of the additives, either in solid solution or in the form of precipitates in the matrix will impede dislocation movement, causing an increase in the yield stress of the alloy and an increase in strength and hardness. The higher Zr content in the 220H and 220M alloys will amplify the impedance to dislocation slip, so that after the same solution treatment, these alloys exhibit maximum hardness.

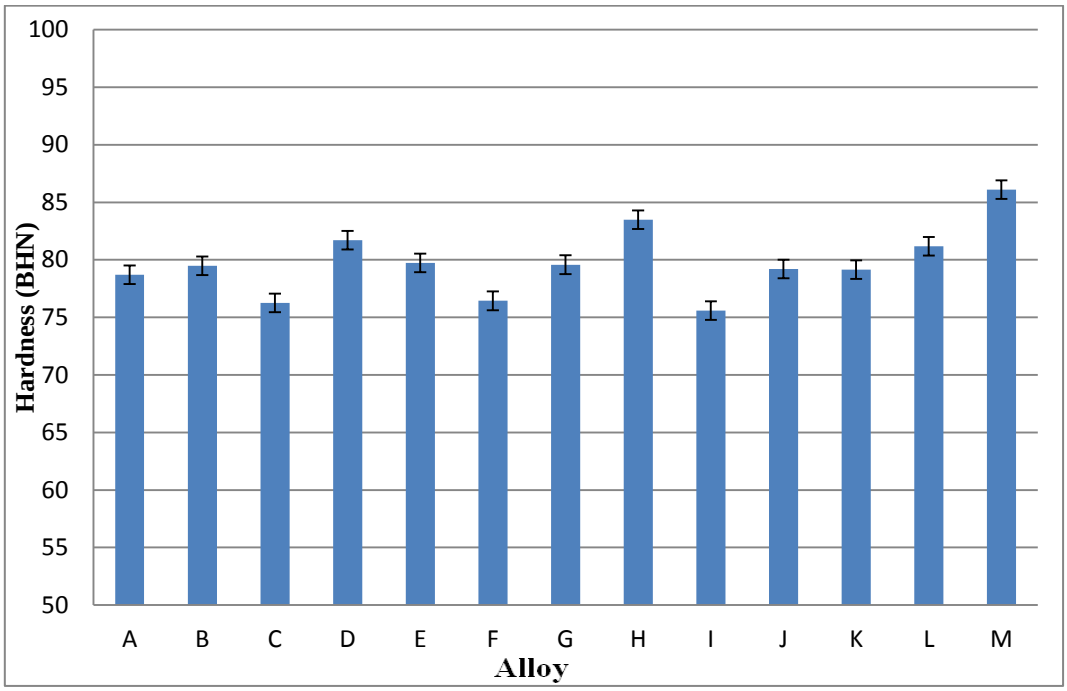

(a)

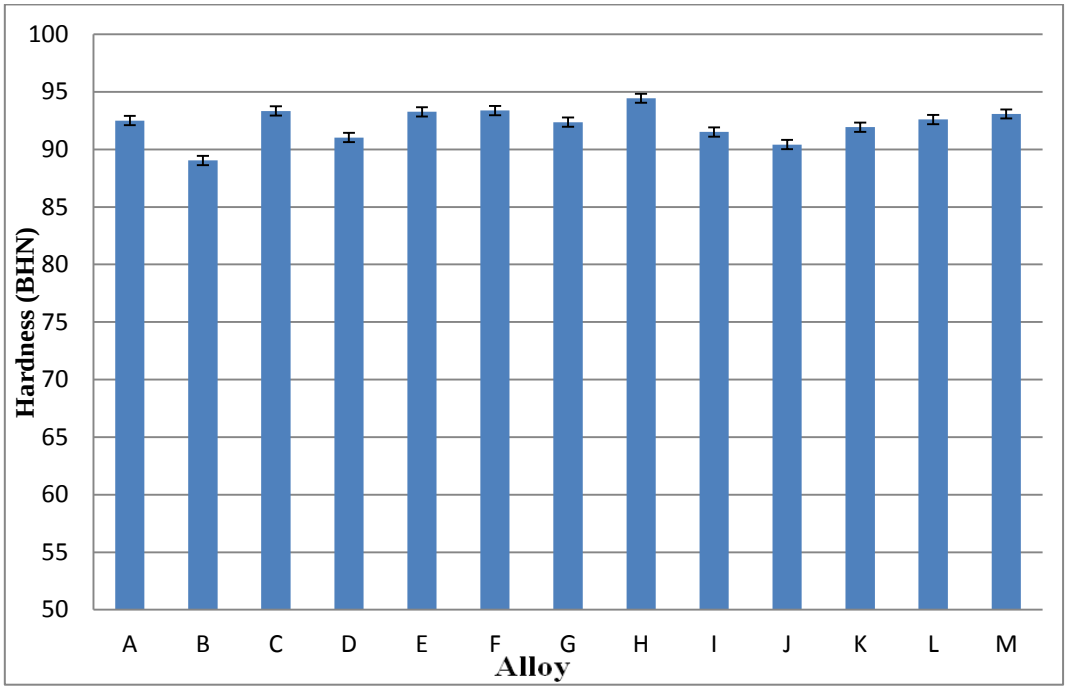

(b)

Figure 4.8 Hardness values for 220 alloys in (a) as-cast, and (b) solution heat-treated conditions.

The increase in hardness of the aged alloys beyond that observed after solution heat treatment may be attributed to the added contribution of precipitation hardening which occurs during aging. For a specified 220 alloy, the type of precipitates formed will vary, depending upon the number of additives as well as their concentration levels. Based on the nature and size of these precipitates, the strength will be affected accordingly. Dislocations can cut through smaller precipitates more easily which is not the case when the precipitates are larger in size, where the latter impede dislocation movement. Thus, the strength of the alloy increases with increasing size (or radius) of the precipitate. The two mechanisms for precipitation hardening are described by equations corresponding to the two cases: (i) dislocations cutting through the particles where the strength is proportional to the particle radius, and (ii) dislocations bowing around the particles in which case the strength is inversely proportional to the precipitate particle radius. The latter mechanism is also known as Orowan strengthening and is more likely to occur at higher precipitate density.[101]

The hardness values for the aged alloys are shown in Figure 4.9(a) through 4.9(d) for the four respective groups of 220 alloys. As may be seen, over the range of aging temperatures used (155°C, 180°C, 200°C, 220°C, 240°C and 300°C), the hardness improves further, from ~92.4 BHN (average) in the solution-treated condition to 105 BHN or above for all alloys in the aging temperature range of 155°C to 200°C, with peak hardness being observed at 180°C. At higher temperatures, the hardness begins to decrease rapidly, reverting more or less to the solution heat-treated hardness values at 220°C, the as-cast hardness values at 240°C, and then lowers to about 60-65 BHN at 300°C.

As described previously in Chapter 2, the precipitation hardening process in Al-Cu alloys takes place through the sequential formation of precipitates, namely the GP zones (GP 1 and GP2) which are coherent with the matrix, followed by the metastable θ″ and the metastable semi-coherent θ′ phases, and finally the non-coherent θ-$CuAl_2$ phase. Hardening accompanies the formation and growth of the GP zones caused by the distortion of the matrix lattice which hinders dislocation movement. As these precipitates transform successively to θ″ and θ′ phases, the latter contribute to increasing the strengthening level of the alloys, whereas with the precipitation of the θ-$CuAl_2$ phase, the strength begins to decrease due to the lack of coherency between the precipitates and the metal matrix.

Another point to consider from the point of view of precipitation reactions is that the 220 base alloy has a complicated chemical composition, added to which the various additives used to prepare the different 220 alloys studied will result in a wide variety of age-hardening phases which will form during aging. These phases, with their precipitation sequences, may occur either simultaneously or independently.[102] This would explain the variations in the hardness curves from one alloy to another, as observed in Figure 4.9. In fact, in this regard, it is interesting to note how the peak hardness of Alloy G more or less extends across the 155ºC-180ºC-200ºC aging temperature range, and that the decrease in hardness with further increase in aging temperature is not as rapid as in the case of the other alloys, as shown in Fig. 4.9(b).

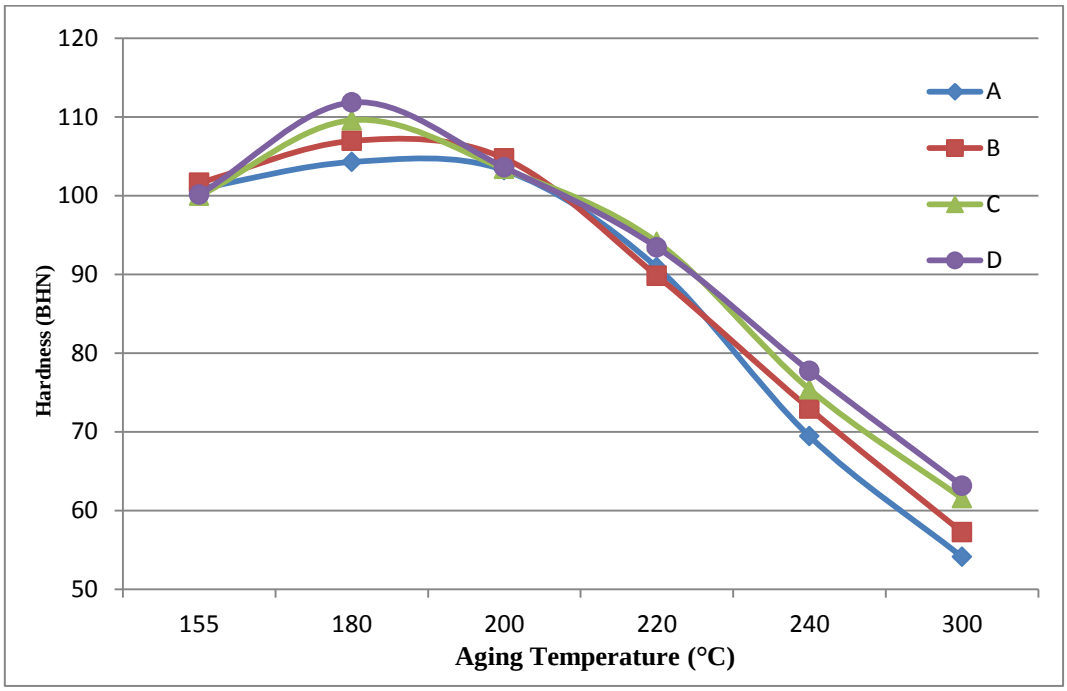

(a)

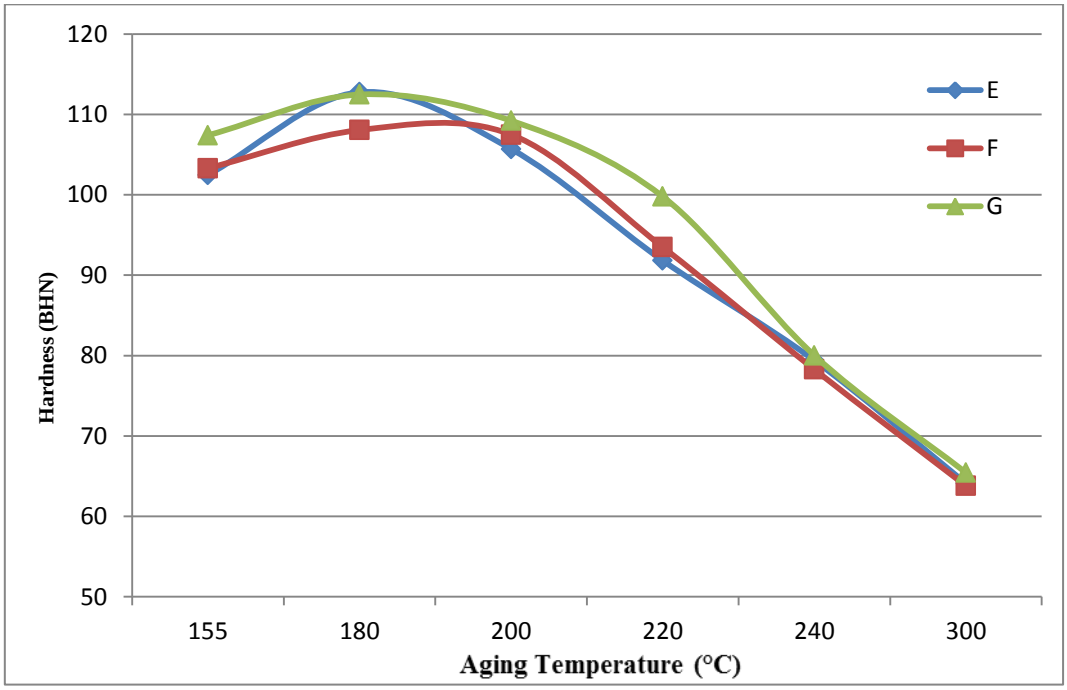

(b)

Figure 4.9

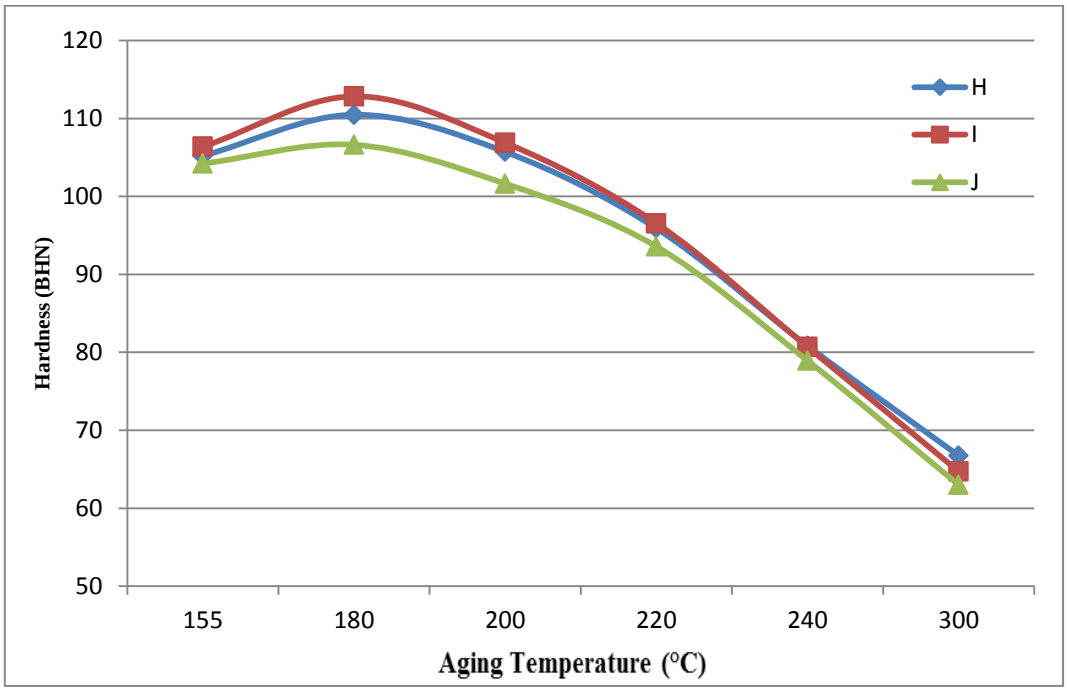

(c)

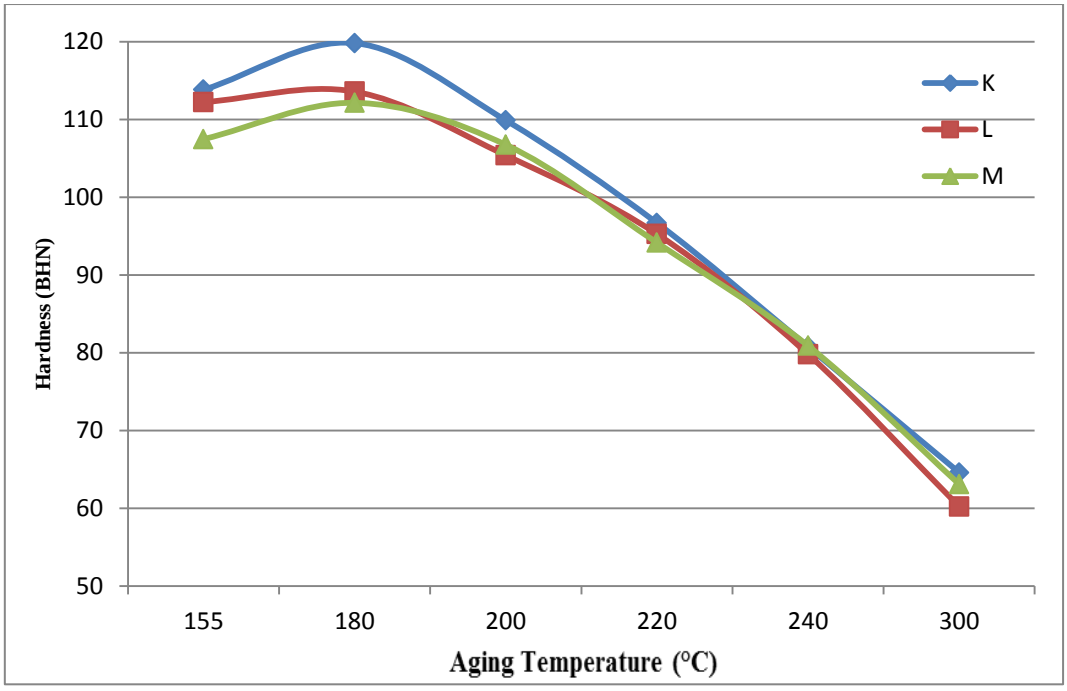

(d)

Figure 4.9 Hardness values for 220 alloys after aging at various temperatures for (a) I, (b) II, (c) III, and (d) IV alloy groups.

4.3.2 Tensile Test Results

As-Cast and Solution Heat Treated Conditions

Figure 4.10 shows the UTS values obtained for the 220 alloys studied in the (a) as-cast and (b) solution heat-treated conditions. The tensile strength values lie in the range of 220MPa to 250MPa in the as-cast condition, whereas they exhibit values in the range of 265 MPa-315 MPa after solution heat treatment, showing an average overall increase of about 23.4%. The observed increase in tensile strength may be attributed to the dissolution of the Cu-rich intermetallic phase particles, mainly the Al_2Cu phase during solution treatment, and solid solution hardening is the process mainly responsible for the observed increase in strength.

As Figure 4.10(a) shows, alloy G and E possess UTS values in the as-cast condition that are lower than that of the base alloy A. This may be attributed to the relatively high volume fraction of intermetallics observed in these alloys. Both these alloys contain 0.15%Ti + 0.50%Zr, with alloy G containing 0.70%Ag in addition.

According to Reich *et al.* [12] who investigated the evolution of the Ω phase (which is similar in structure to the θ-$CuAl_2$ phase) in Al-Cu-Mg-Ag alloys, several studies are reported in the literature which propose different structures of the Ω phase, and how the addition of Ag changes the precipitation process which normally occurs in Al-Cu-Mg alloys. Garg *et al.*[71] have reported, however, that while Ag is not needed for the formation of the Ω phase, its presence greatly increases the number density of these precipitates in the alloy. The mechanism by which Ag promotes the nucleation of the Ω phase is still not known.

The improvement in tensile strength of Alloy B (containing 0.02%Sr) in comparison to the base alloy may be attributed to the refining effect of Sr on the morphology of the α-Fe script intermetallic phase, which leads to a more even distribution of the α-Fe phase particles within the matrix.[11] Similarly, in the case of grain refining additions, the presence of Ti, Zr, and Sc (in the case of Alloy J) enhances the tensile strength in Alloys C, F, J, L and M, due to the decrease in grain size from 434 μm in the base alloy A to much lower calues of 142, 122, 56, 132 and 76 μm, respectively (see Table 4.3). In the as-cast condition, therefore, the best combination for maximizing UTS appears to be (0.15 Ti + 0.30 Zr), followed by (0.15 Ti + 0.30 Zr + 0.15 Sc).

The tensile strength values of the 220 alloys are considerably enhanced following solution heat treatment, particularly in the case of Alloys B, G and C. In the case of Alloy B, the Cu-rich intermetallic phase become almost completely dissolved in solid solution, so that the volume fraction of these intermetallics in the microstructure is reduced by about a third, as reported by Elgallad [103] who carried out a detailed microstructural investigation of permanent mold cast 220 alloys.

Figure 4.11 displays the yield strength results for the same alloys. As before, the YS values which range from 162 to 193 MPa (average 177.5 MPa) in the as-cast samples, increase to 180-205 MPa after solution treatment (average 192.5 MPa), showing an overall average increase of ~8.5%. Any mechanism which resists the mobility of dislocations in an alloy will increase its yield (and tensile) strength. For the as-cast 220 alloys shown in Figure 4.11(a), grain boundary hardening through grain size reduction is expected to be the operating mechanism in the case of alloys F, J, K, L and M. The low yield strength

exhibited by Alloy D (and alloy I to a lesser extent) may be attributed to the interactions between Sr and Ti, or Sr and B (from the Al-5Ti-1B master alloy used for the Ti additions) which have been reported to cause mutual 'poisoning' of the elements, [104] so that modification and/or grain refining effects are suppressed. This is not the case for Alloys B and C which contains individual additions of Sr and Ti, respectively.

Upon solution heat treatment, the YS values of all alloys increase, in a manner similar to that shown in Figure 4.10(b) for the UTS results. The same strengthening mechanisms apply in this case, with solid solution strengthening acting as the operating mechanism.

As Figure 4.12 shows, the pct elongation exhibited by these alloys increases from an average of roughly 2.3% in the as-cast state to values that range from 3.3% min to 5.2% max after solution treatment, with an overall average of ~4.3%. Compared to this average, Alloy C exhibits a relatively higher elongation of 5.8%, which Alloy B attains the maximum ductility at 6.8% among all the alloys studied. The dissolution of the Cu-rich intermetallic phases due to the presence of Sr, as well as its effect on refining the α-Fe intermetallic phase so that it is more evenly distributed in the matrix are the reasons for the large increase in elongation observed.

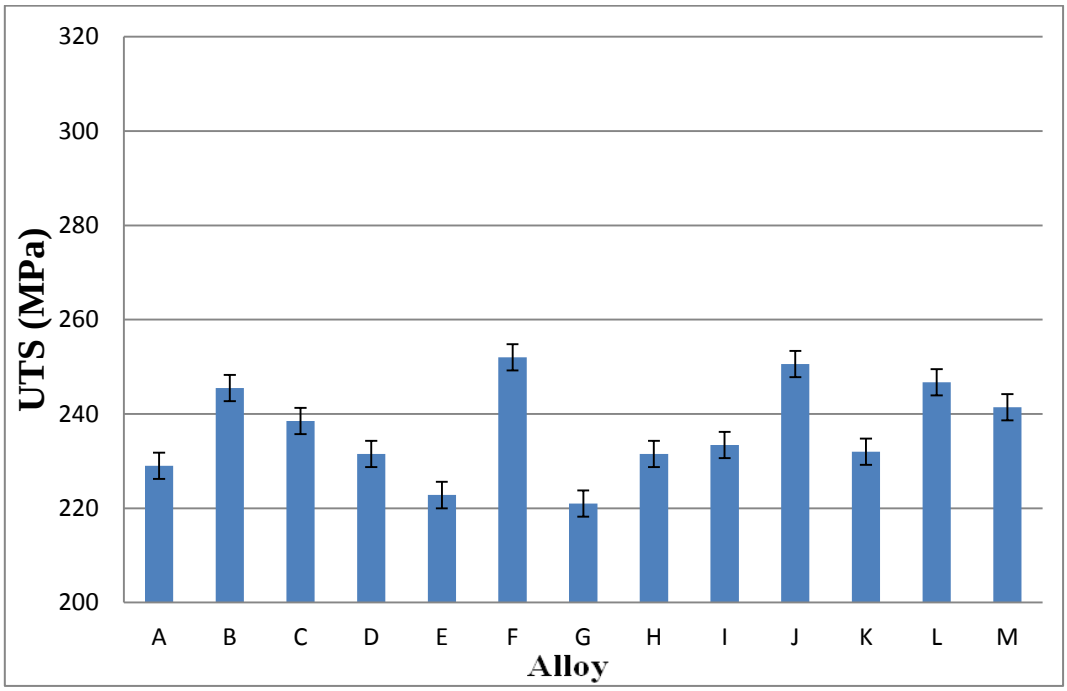

(a)

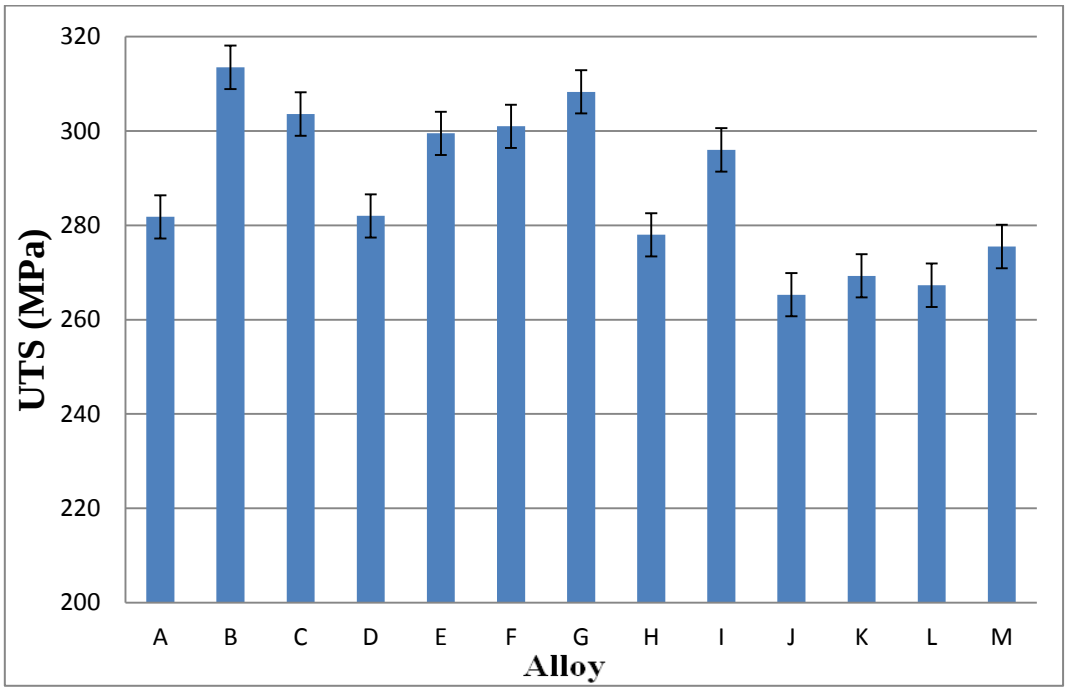

(b)

Figure 4.10 Ultimate tensile strength data for 220 alloys in (a) as-cast, and (b) solution heat-treated conditions.

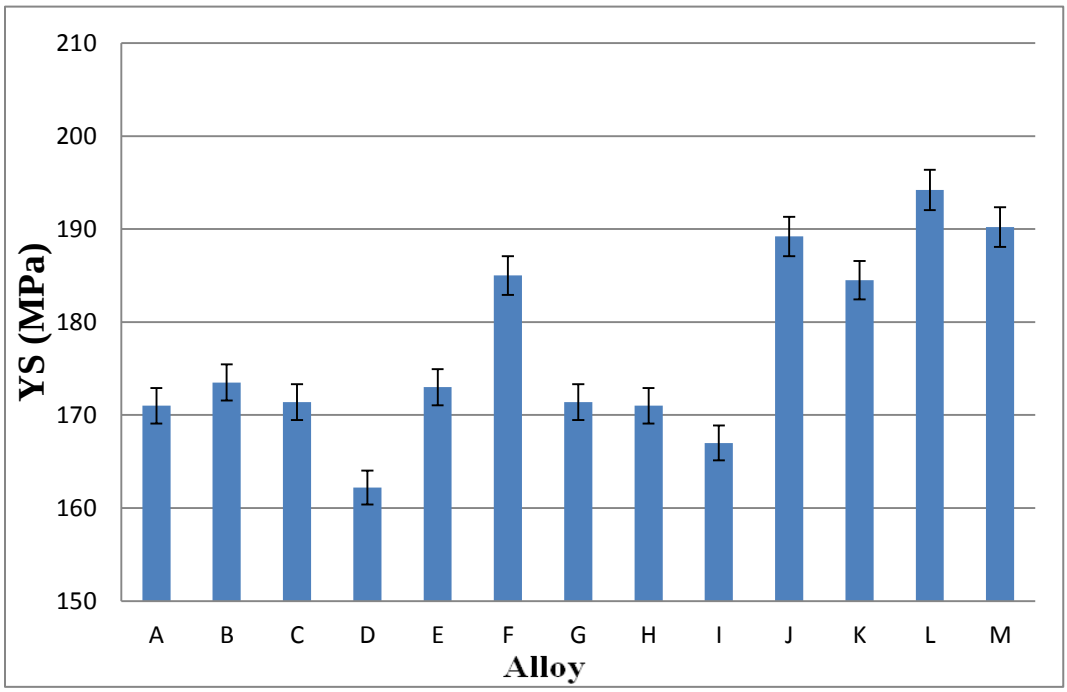

(a)

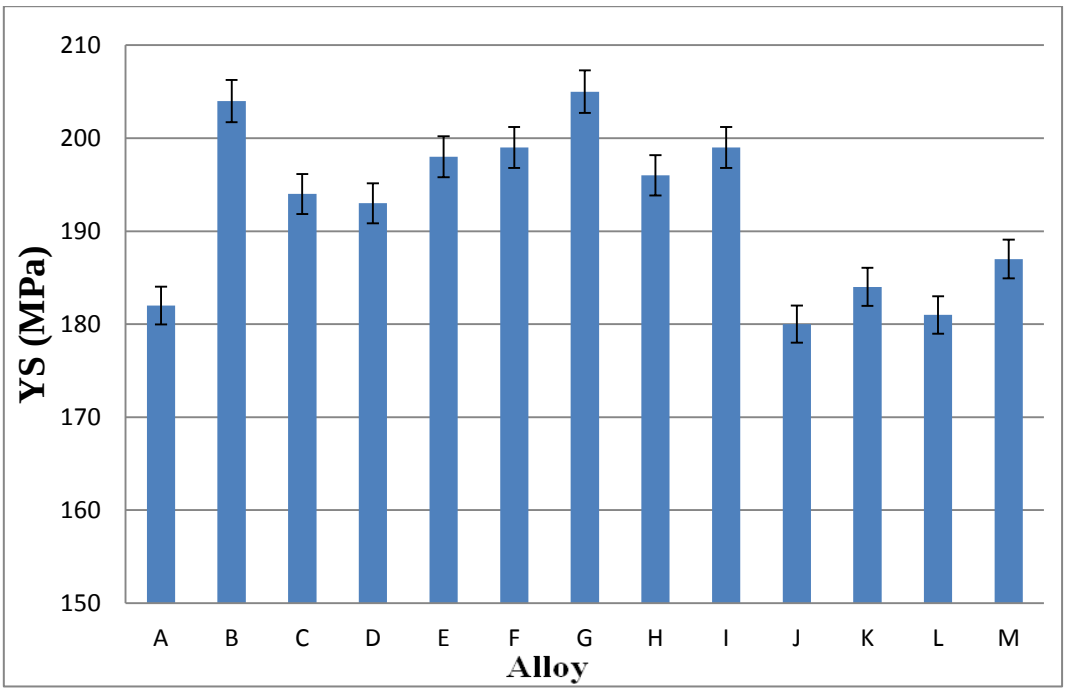

(b)

Figure 4.11 Yield strength data for 220 alloys in (a) as-cast, and (b) solution heat-treated conditions.

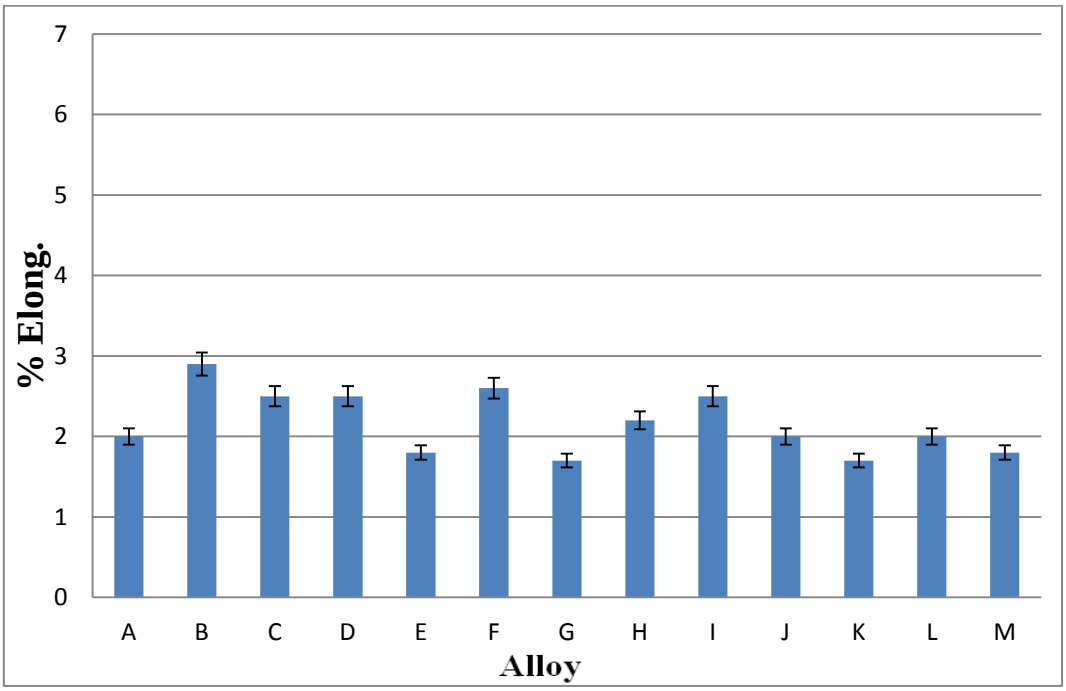

(a)

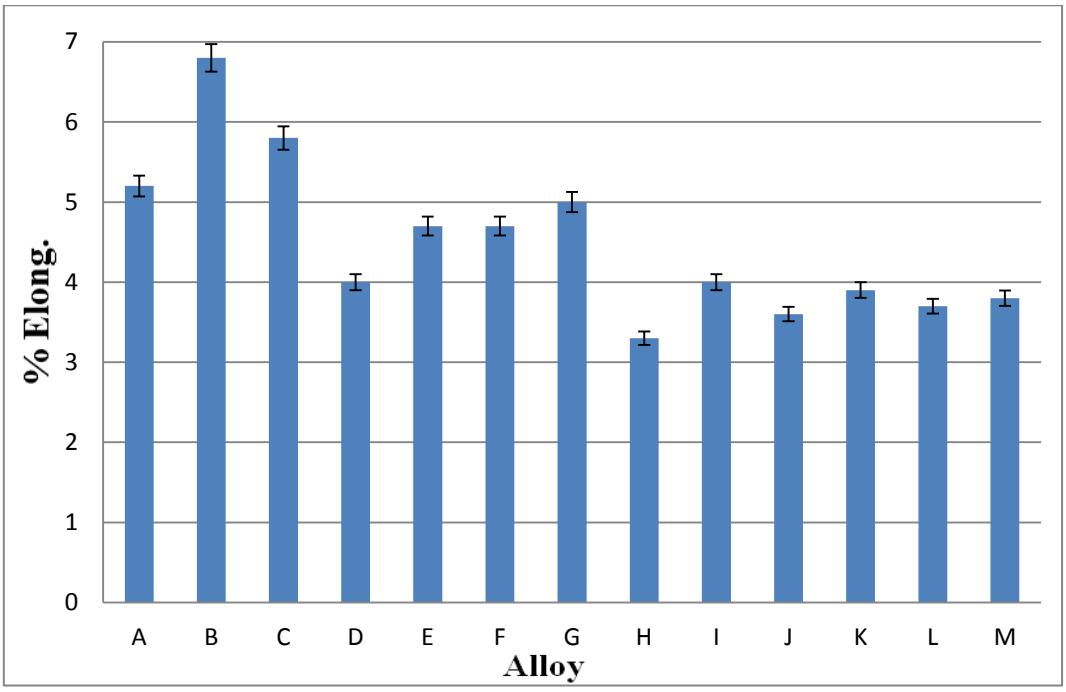

(b)

Figure 4.12 Elongation data for 220 alloys in (a) as-cast, and (b) solution heat-treated conditions.

T6-Aged Condition

Figures 4.13 through 4.15 show how the tensile properties of the 220 alloys studied vary with aging temperature for the four alloy groups. Compared to the range of UTS values exhibited by the solution-treated alloys (265 to 315 MPa), aging at 155°C increases the strength by ~16.6% on average (~330 to ~352 MPa) over the four groups of alloys studied, the highest improvements being noted for the group II (or the E, F, G alloys) as may be observed from Figure 4.13. The addition of Zr-Ti produces a refined non-dendritic structure that decreases the probability for porosity formation and increases the amount of dissolved Al_2Cu after solution heat treatment, and thereby the level of Cu in solid solution of α-Al, which then allows for a larger amount of precipitation hardening to take place upon aging, and therefore improve the alloy strength. Additionally, dispersoid precipitates of Al_3Zr and/or $Al_3(Zr_{1-x}Ti_x)$ may act as nucleation sites for the hardening phases during the aging process, resulting in further improvement in strength.[105-107] In order to enhance the mechanical properties of an aluminum alloy, it is important to obtain a thermally stable microstructure and coarsening-resistant dispersoids. This may be achieved by adding Zr, which has the smallest diffusion flux in aluminum of all the transition metals; the presence of Zr leads to the formation of fine dispersoids that resist coarsening at higher temperatures, which helps to improve/maintain the mechanical properties.[54, 108, 109]

Figure 4.13 also shows that peak aging of the 220 alloys is achieved mainly at 180°C, although in some cases, this may spread up to 200°C. Softening begins as the aging temperature is increased above this range, so that with the coarsening of the precipitates, the alloy strength decreases and a corresponding increase in ductility is observed.

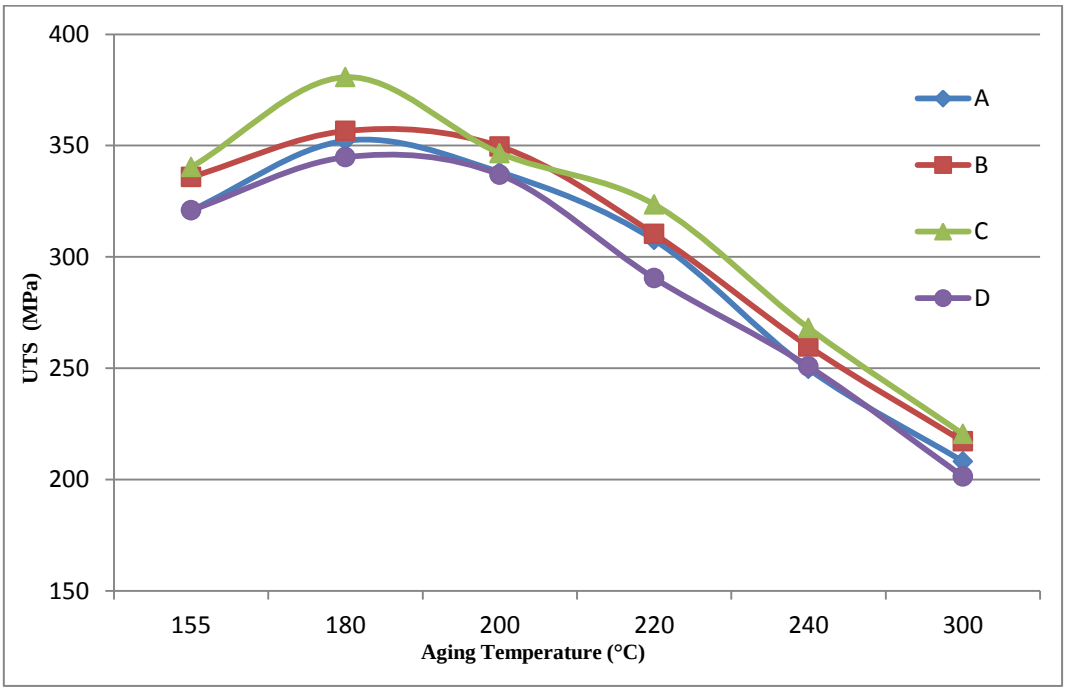

(a)

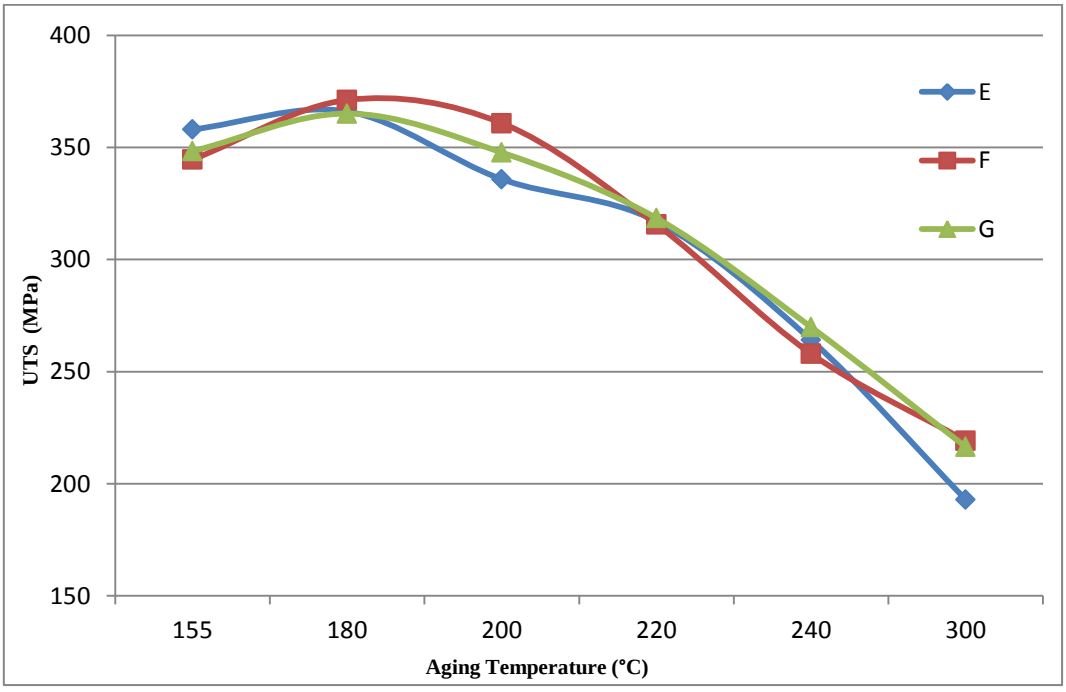

(b)

Figure 4.13

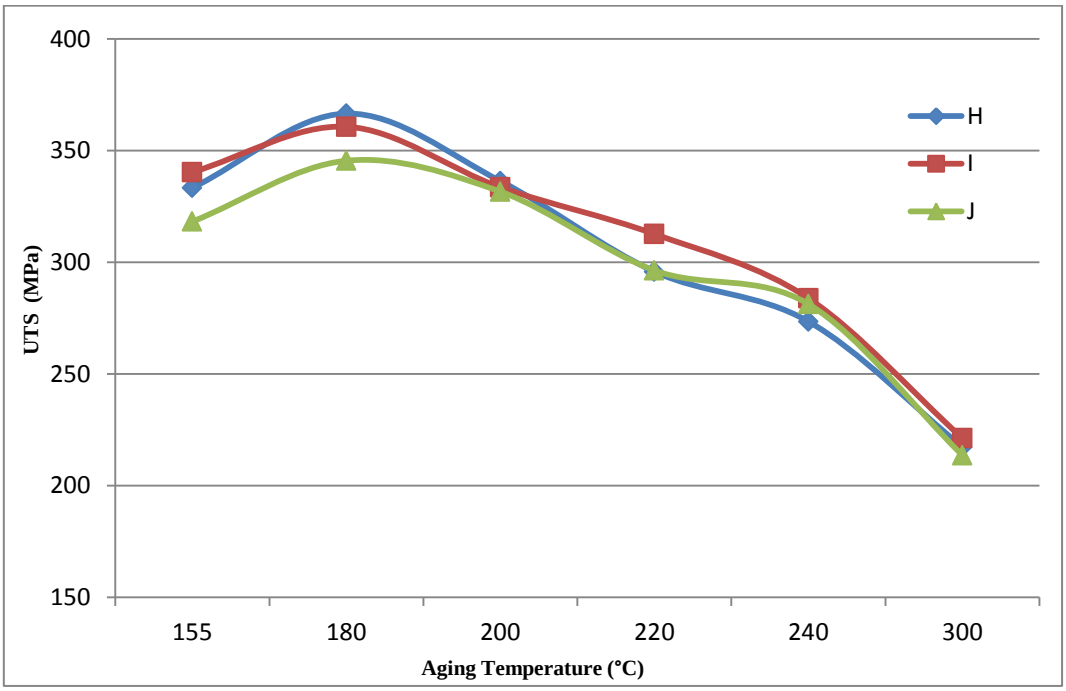

(c)

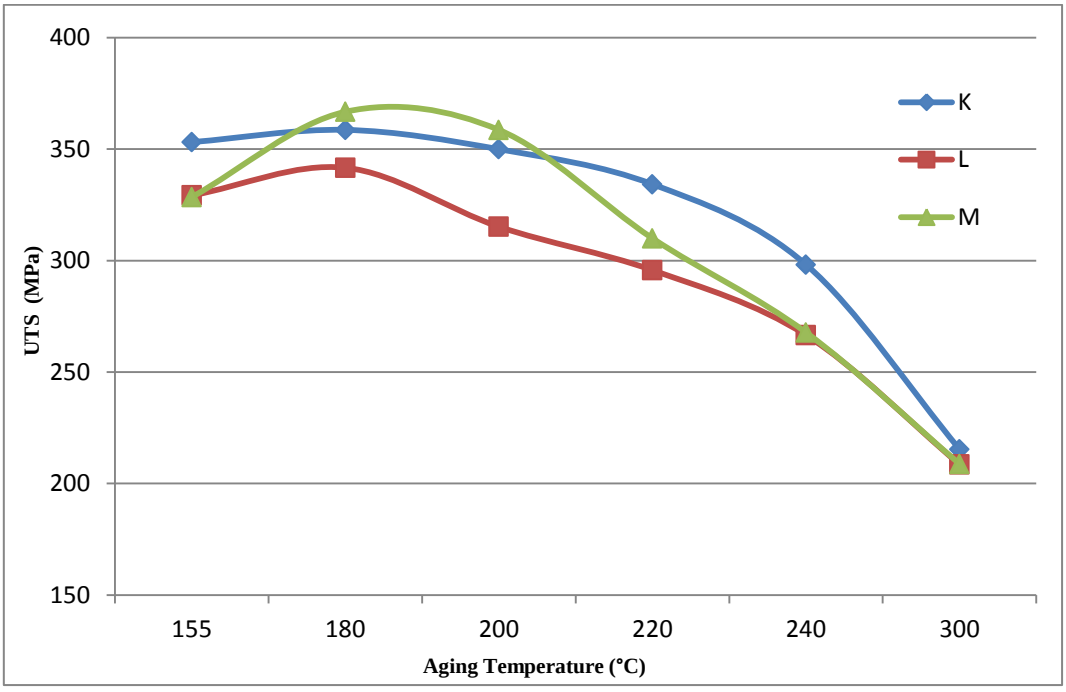

(d)

Figure 4.13 Variation in UTS as a function of aging temperature for the 220 alloys studied.

With respect to the alloy yield strength, Figure 4.14 reveals that the base alloy A and alloys B, C and D show almost identical behavior as the aging temperature is increased from 155°C to 300°C. Alloys E, F, G of Group II, and alloys H, I, J of Group III also show more or less similar behavior across this range of aging temperatures. At 155°C, the YS value in Group I is 250 MPa regardless of the Sr and/or Ti additions of this group. In comparison, the YS values for the other three groups increase by about 20-45 MPa due to the Zr, Ag and Sc additions. Highest YS values are observed within the peak aging temperature range of 180°C-200°C, with maximum YS values being exhibited by alloys M, I, J and F.

It is interesting to note that these alloys contain one or more of the elements Ti, Zr, Sc and Ag in different amounts. Alloy M, which shows YS values of 346-348 MPa, indicates that a high Zr level (0.5 wt%) greatly improves the yield strength, due to its influence in controlling the evolution of the grain size and the sub-grain structure through the formation of a copious amount of Al_3Zr phase dispersoids. The resistance of these dispersoids to dissolution and coarsening increase the alloy yield strength during precipitation hardening. Similarly, the alloys I, J and F give rise to the formation of Al_3(Zr,Ti) and Al_3(Zr,Sc) precipitates due to the presence of combined Ti+Zr (alloy F), Ti+Zr+Sc (alloy J), or Ti+Zr+Ag+Sr (alloy I) additions.

As was mentioned earlier in section 4.3.2, while discussing the tensile properties of the as-cast and solution heat treated alloys, the presence of Ag contributes to the formation

of the Ω phase which significantly improves the high temperature mechanical performance of Alloy I due to the high resistance of this phase to particle coarsening.[12]

This phase is similar in structure to the Al_2Cu phase, and the addition of Ag significantly increases the number density of these Ω precipitates. With further increase in aging temperature, the YS begins to decrease rapidly, as softening commences, all alloys reaching a YS value of 100 MPa at 300°C aging temperature.

In keeping with the tensile strength results shown in Figure 4.13, the alloy ductility varies accordingly, as shown in Figure 4.15, the lowest ductility values being observed in the peak aging temperature range of 180°C-200°C, with alloys M and J exhibiting elongations of less than 1% at these temperatures.

Alloy D shows the lowest ductility values across the aging temperature range, Figure 4.15(a), even lower than the base alloy A. This may be attributed to the interaction between Ti and Sr, reducing the benefits of the individual additions. This indicates that the alloy is more resistant to softening than the other alloys. While all alloys show maximum ductility at 300°C, the greatest amount of softening is noted for the C, F and K alloys.

To summarize, these results show that, depending on the end application, the aging conditions for 220 type alloys may be selected to provide the best compromise between strength and ductility required for that application, bearing in mind also the economic benefits of the 5 hours aging time used in this work.

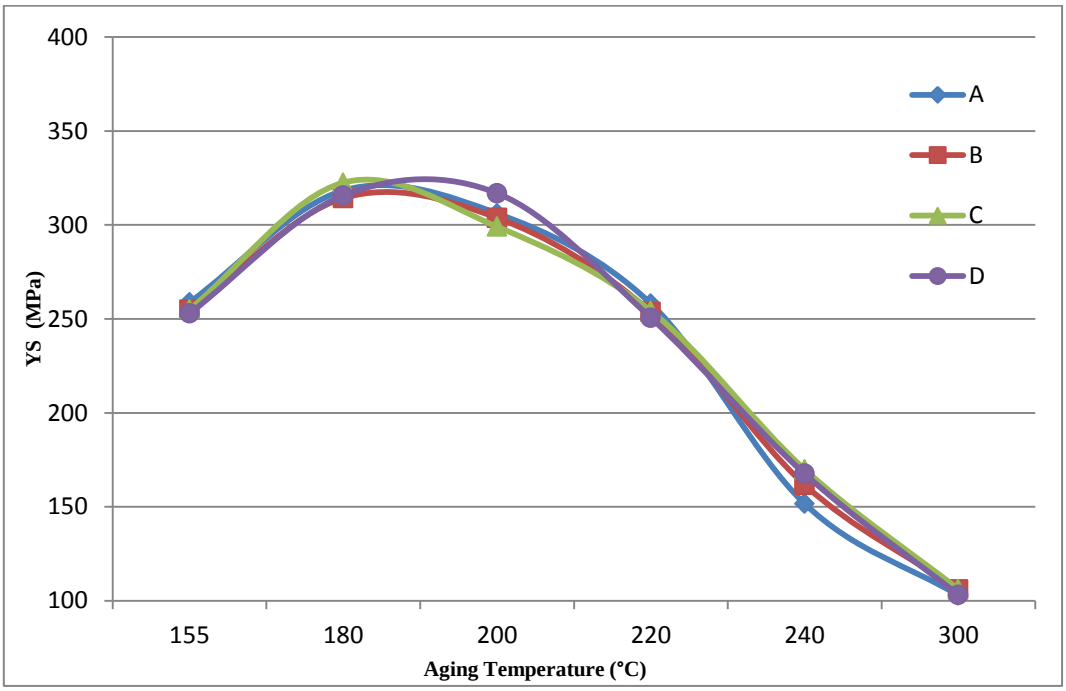

(a)

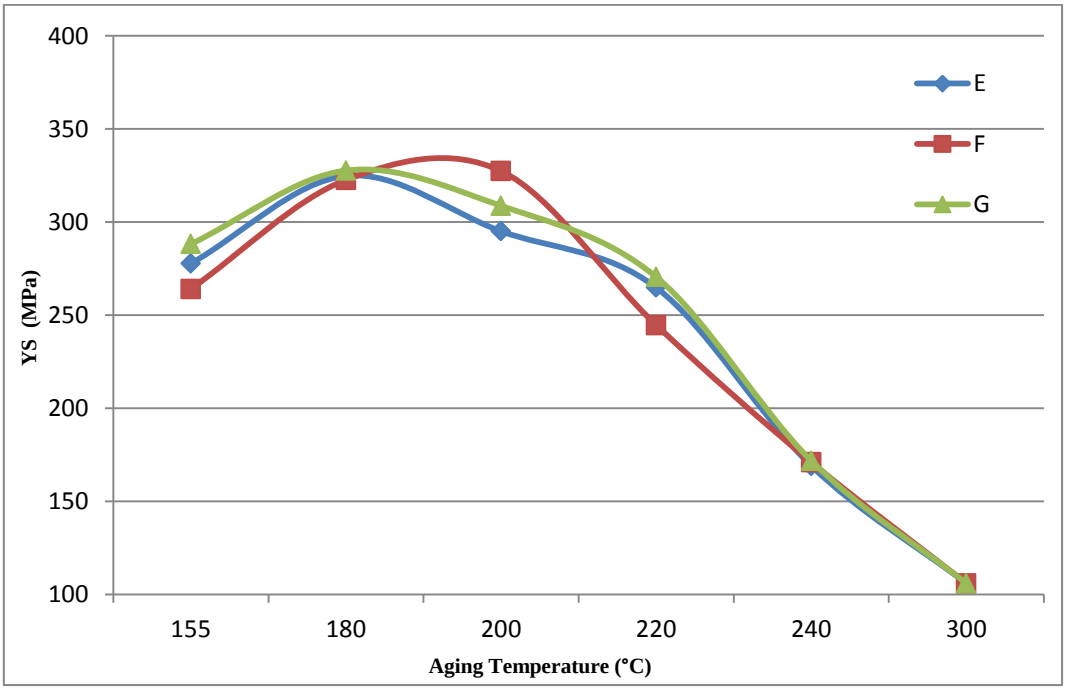

(b)

Figure 4.14

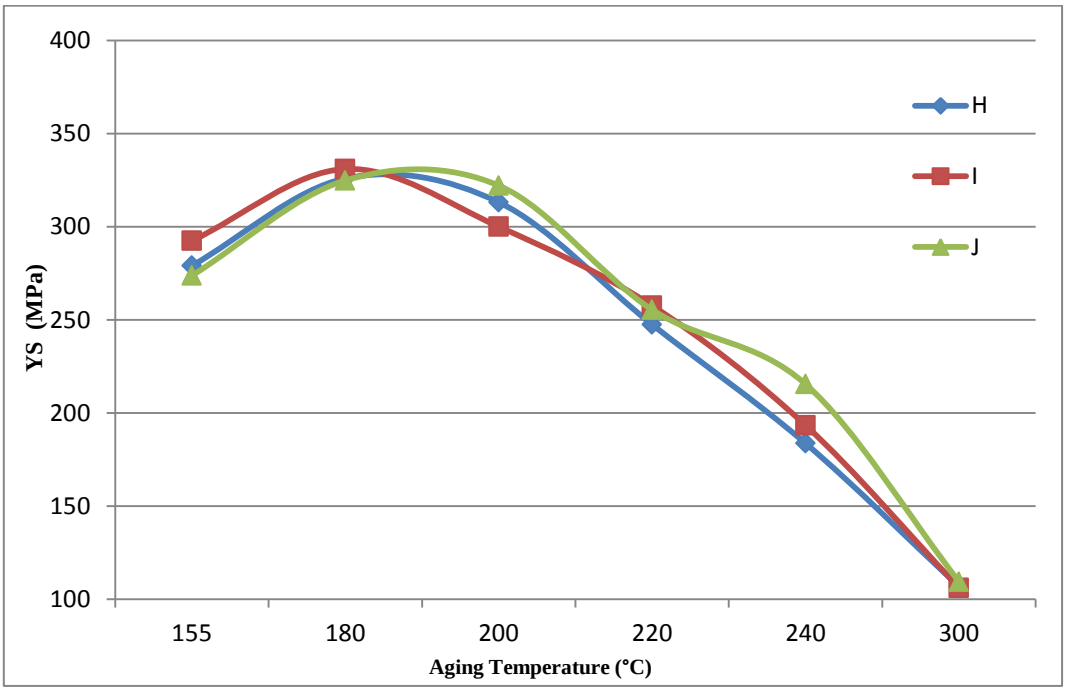

(c)

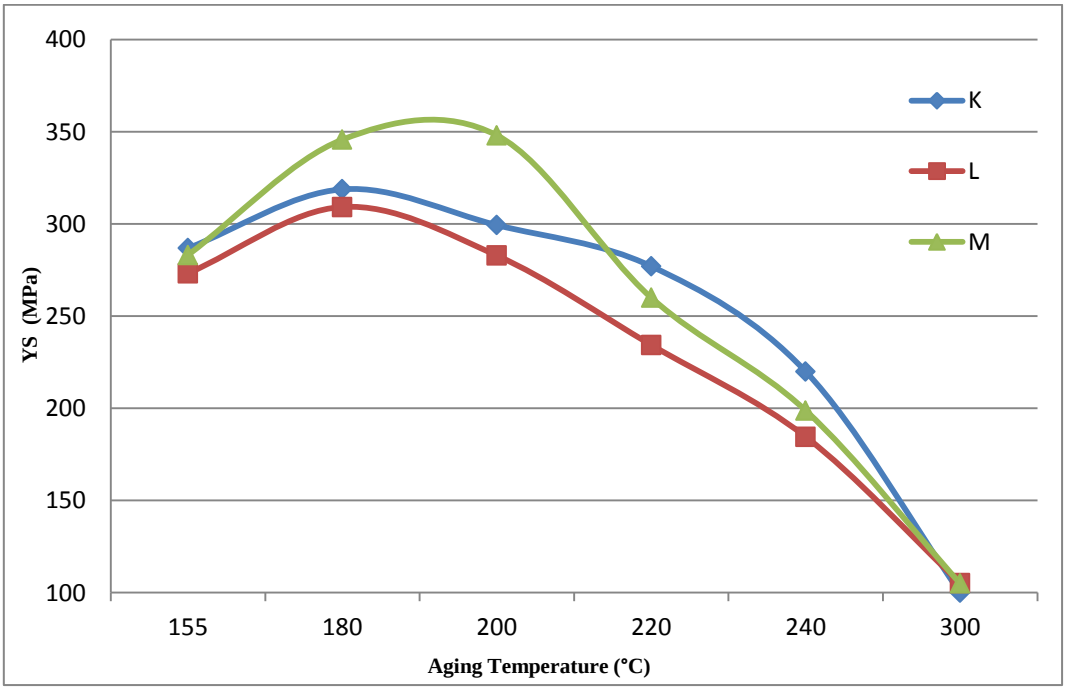

(d)

Figure 4.14 Variation in YS as a function of aging temperature for the 220 alloys studied.

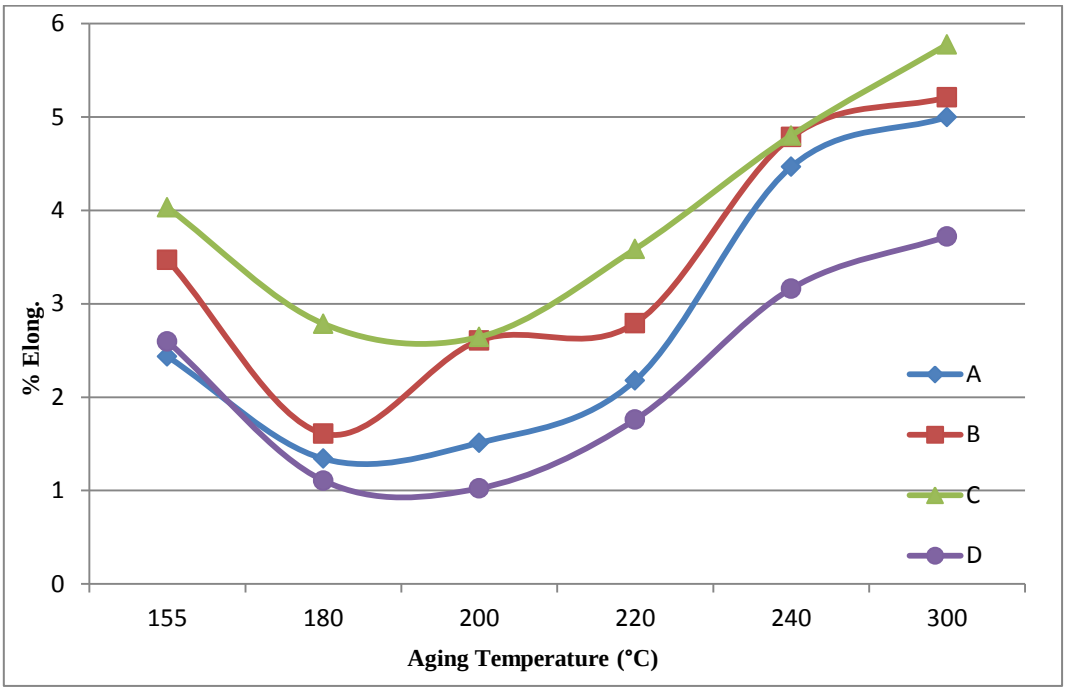

(a)

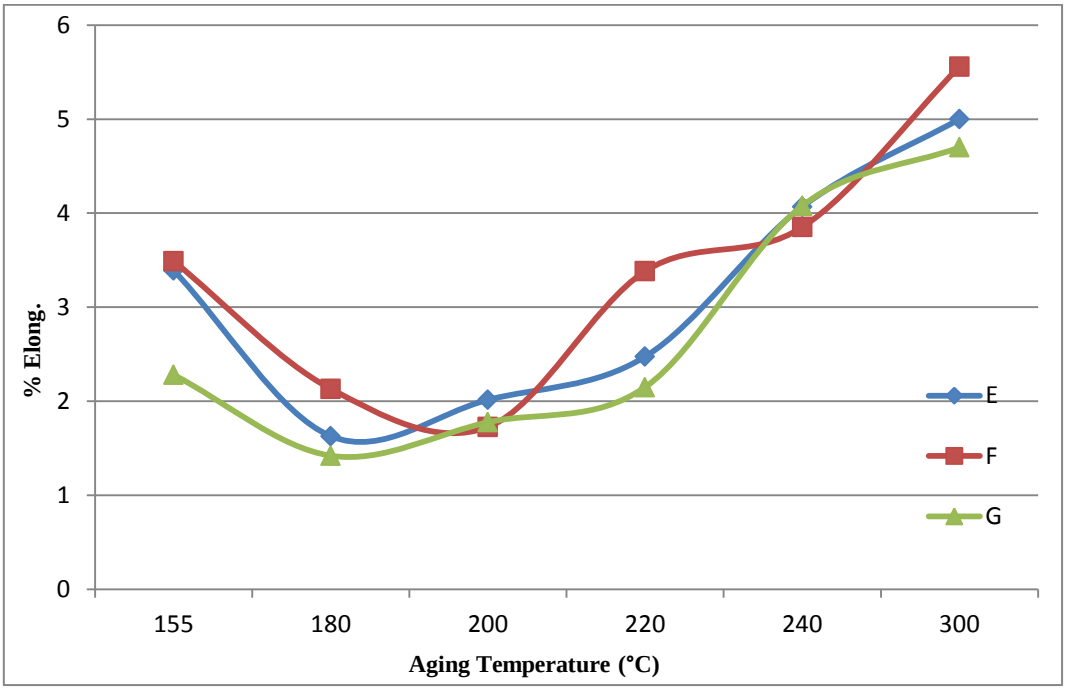

(b)

Figure 4.15

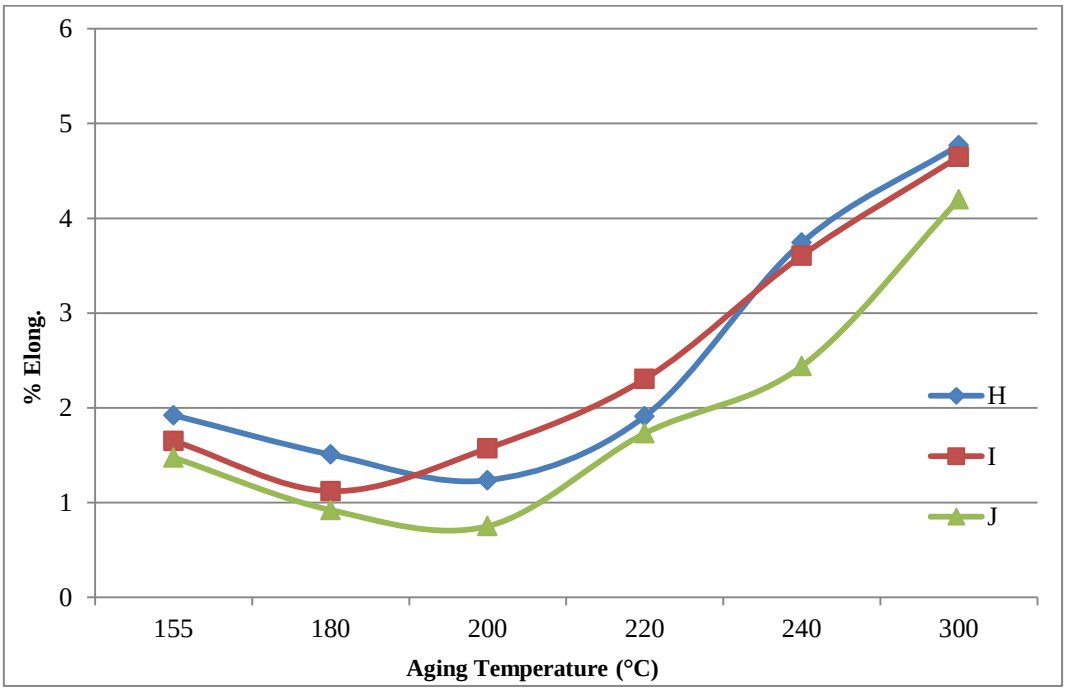

(c)

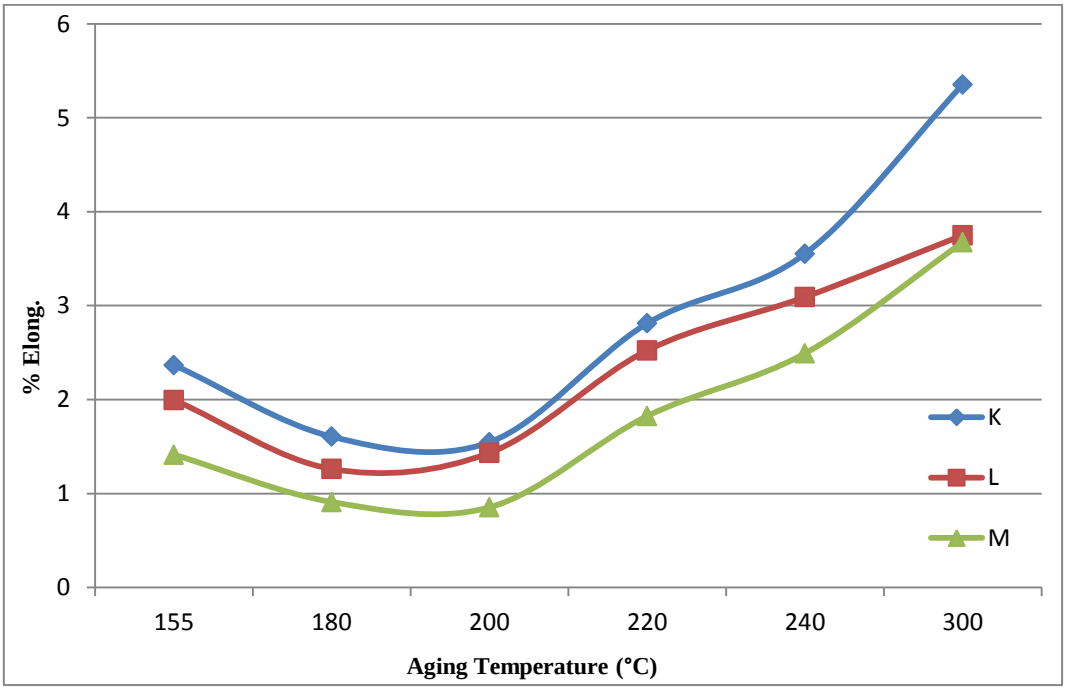

(d)

Figure 4.15 Variation in %El as a function of aging temperature for the 220 alloys studied.

4.4 ANALYSIS OF TENSILE PROPERTIES USING THE QUALITY INDEX CONCEPT

As mentioned in Chapter 2, Drouzy *et al.*[77, 78] proposed the concept of the Quality Index (Q) as a means of better expressing the tensile properties of Al-Si-Mg alloys, in terms of how variations in Mg content and the aging conditions affected the alloy "quality" or performance in their study of Al-7%Si-Mg or 356-type alloys, by the use of equations that allowed to plot charts of *iso-Q* versus *iso-YS* lines on a quality index chart such that it was easy to see how the alloy quality was affected by the heat treatment and alloy composition. This concept was later extended to include Al-Si-Cu and Al-Si-Cu-Mg alloys by Caceres,[79, 80] whose model was based on the assumption that the deformation curves of a materials may be represented by the Holloman equation, $P = KS^{n}$.[81] The methodology and the equations used by both groups of researchers were described in detail in Chapter 2 and are only referred to / reported in relation to Figures 4.16 and 4.17.

Figure 4.16 shows simple plots of the quality index Q values derived from the equations proposed by Drouzy *et al.* as a function of the aging temperature for all the 220 alloys studied. While the alloy quality shows a general tendency to decrease with increase in aging temperature, nonetheless, some alloys show a definite increase in quality at 180°C (alloys C and H) or at 220°C (alloys I and K) aging temperatures. In the Group I alloys, alloy D is lower in quality than even the base alloy A, while alloy C appears to be the most promising alloy in this group. Likewise, in Group IV, the quality of alloy K is higher than the other alloys across the entire aging temperature range.

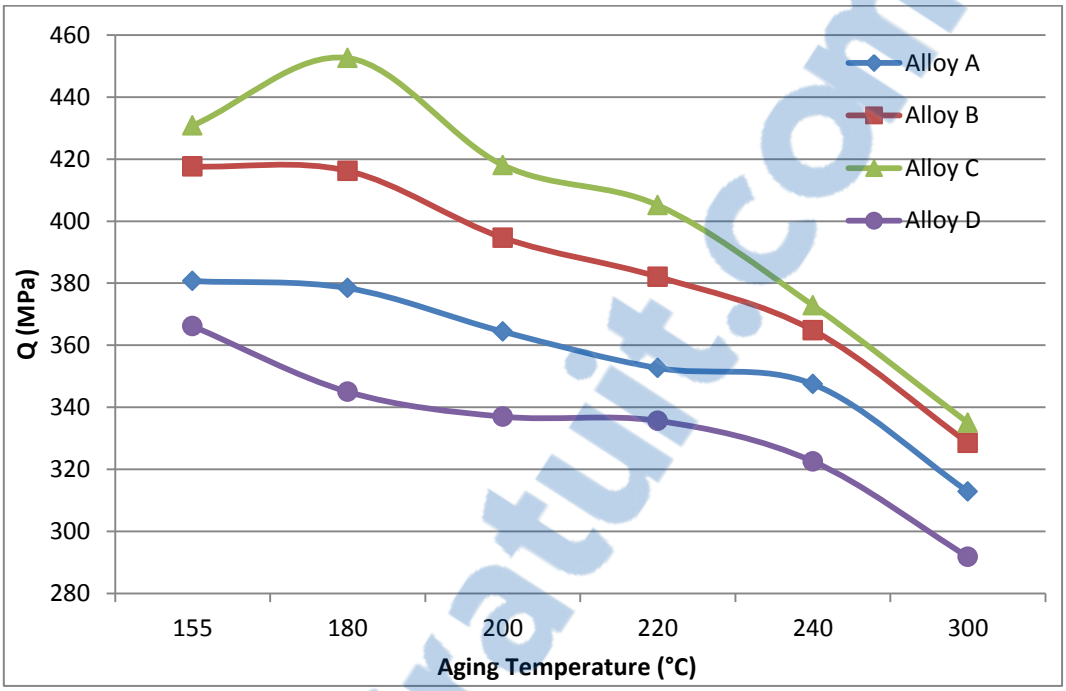

(a)

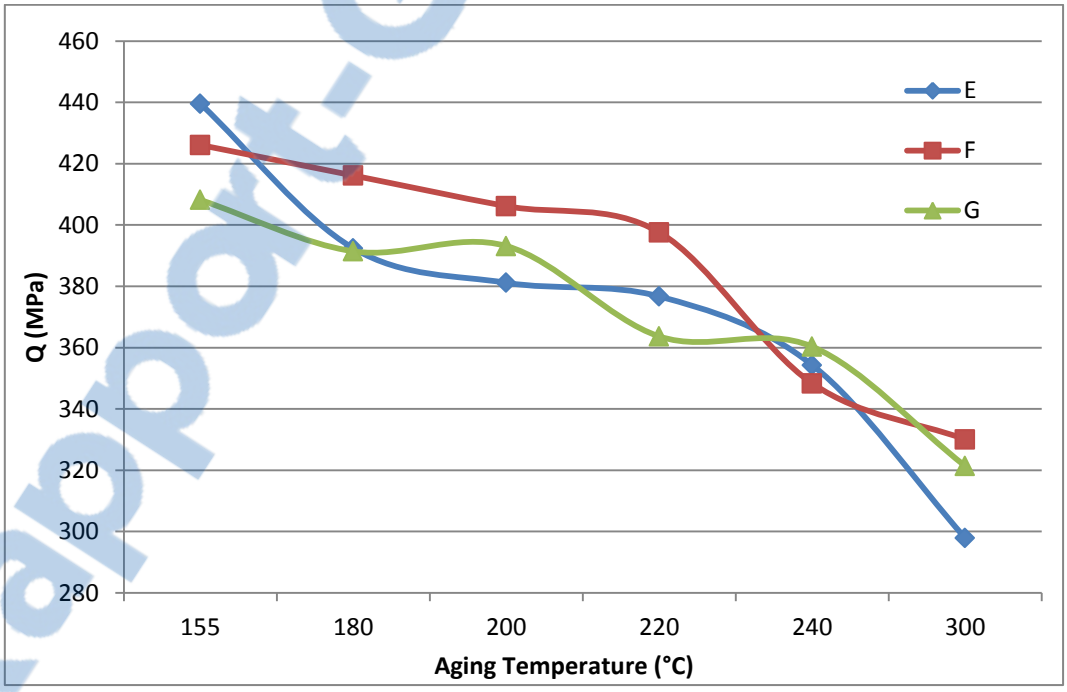

(b)

Figure 4.16

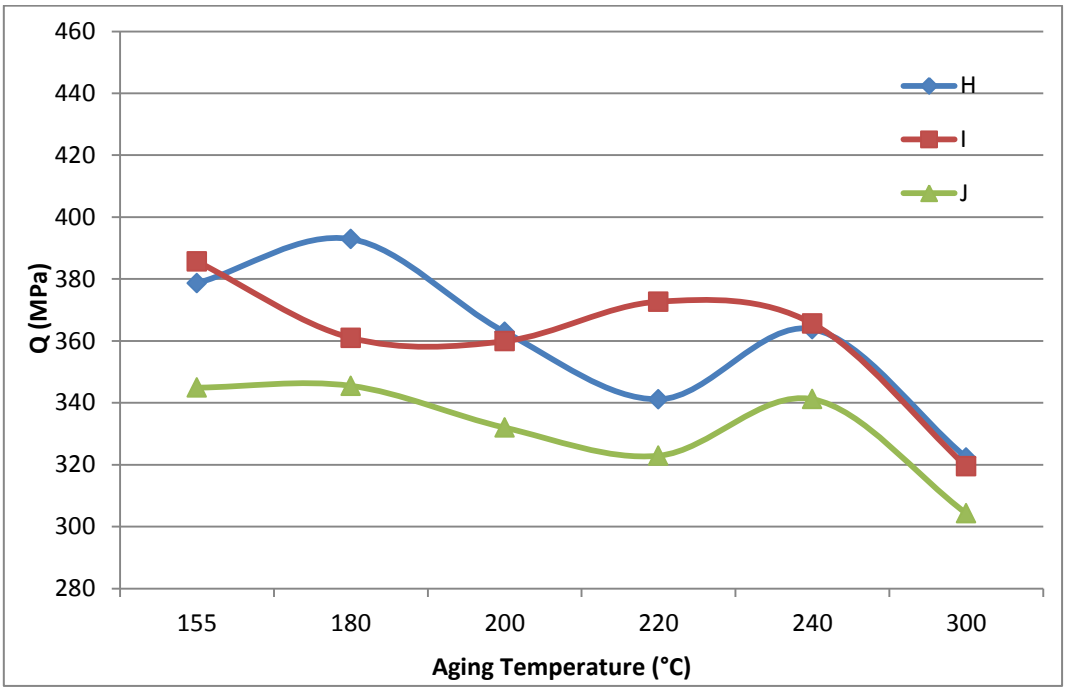

(c)

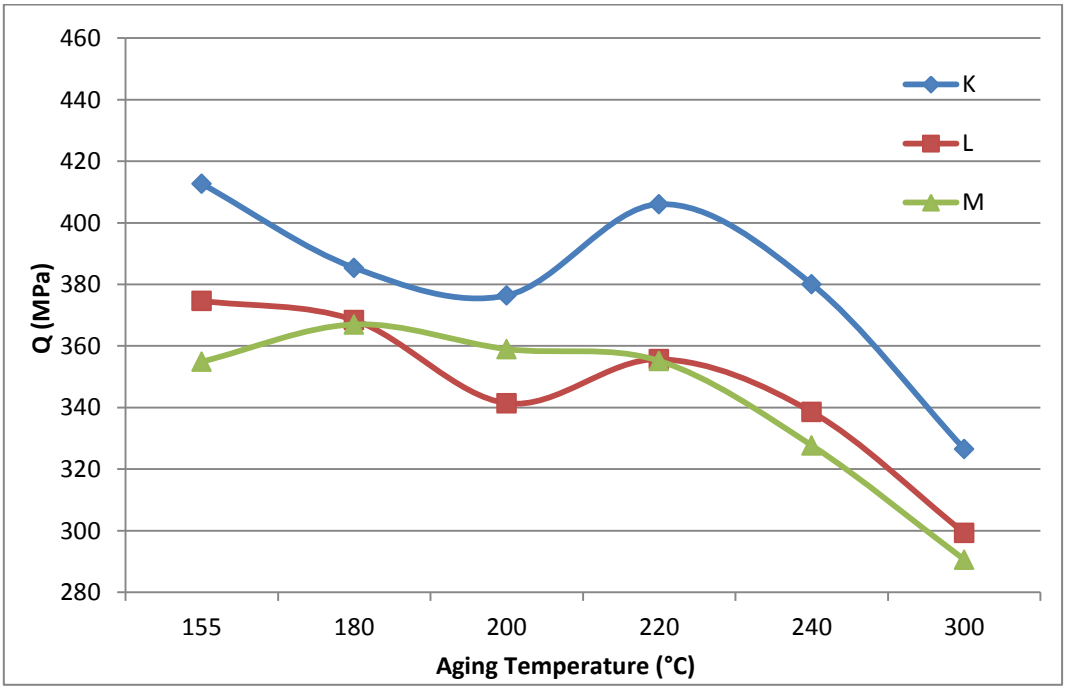

(d)

Figure 4.16 Variation in Q with aging temperature for the 220 alloys studied (using the equations for Q developed by Drouzy *et al.* [77, 78]).

The Q values plotted in Figure 4.16 are derived from the equation:

$$Q = \sigma_{UTS} + d \log (E_f) \qquad \text{Eqn. 4.1}$$

following Drouzy *et al.*'s approach, where Q is the quality index in MPa, σ_{UTS} is the ultimate tensile strength (in MPa), E_f is the percentage elongation to fracture, and d is a material constant equal to 150 MPa for Al-7Si-Mg alloys. As may be seen, Q is dependent on the ultimate tensile strength and the percent elongation values achieved by the alloy for a specified heat treatment condition. The quality index value is intrinsically related to the quality of the castings so as to obtain the best possible compromise between tensile properties and casting quality, where the latter may be improved by controlling the impurity elements, casting defects, modification, solution heat treatment and solidification conditions. The probable yield strength, $\sigma_{P(YS)}$, given by the equation:

$$\sigma_{P(YS)} = a\ \sigma_{UTS} - b \log (E_f) + c \qquad \text{Eqn. 4.2}$$

depends mainly on the hardening elements such as Mg and Cu and also on the age hardening conditions applied to the castings (constants a, b and c are in MPa units).

The strengthening mechanism results from the age-hardening treatment which depends on the interaction between moving dislocations and the precipitated phases. A precipitate in the path of a moving dislocation exerts a resistance against the dislocation. In the case of hard precipitates, the particles will not be deformed and the dislocation will bypass the precipitate by cross-slip or by Orowon looping. In the case of soft precipitates, the particles will be sheared by the moving dislocation and the dislocation will pass through

the particle itself.[81] Hard particles provide maximum hardening levels while soft particles provide lower strength and hardness values. In the former case, the strengthening which results depends on the volume fraction and size of the precipitates, that is, on the inter-particle spacing. The correlation between the yield strength and inter-particle spacing is given by the Orowon relation:

$$\triangle \tau_y = Gb/L$$

where $\triangle \tau_y$ is the increase in YS resulting from the resistance of the hard particles to the dislocation motion, G is the shear modulus of the matrix, b is the Burger's vector of the dislocation, and L is the inter-particle spacing. Thus, by increasing the volume fraction of the precipitates and decreasing their size – in other words decreasing the inter-particle spacing – maximum hardening would be achieved.

When adding hardening elements, the quality index values will be affected in accordance with the *net amount* by which the strength is increased and the ductility is reduced. For this reason, even though the alloy strength may show a high increase, if the ductility is considerably lowered, the alloy quality might not show a corresponding improvement. Broadly speaking, this would explain why the curves shown in Figure 4.16 show dips and peaks across the aging temperature range.

Figure 4.17 displays the quality charts obtained for the 220 alloys studied separated into the four groups. These charts were generated using the Caceres approach, where he proposed a relative quality index, *q*, having the form:

$$q = E_f / E_u \cong E_f / n \qquad \text{Eqn. 4.3}$$

By assuming that true strain and engineering strain are equivalent, and by correlating the true values of stress and strain with the nominal values in the Hollomon equation, $P = KS^n$ (where true stress $P = \sigma(1+E)$ and true strain $S = \ln(1+E)$, σ and E being the engineering stress and strain, n is the strain hardening exponent, and K is the strength coefficient), the equation for q could be expressed as:

$$\sigma = K\,[\ln(1+E)^n\, e^{-\ln(1+E)} \cong K\,E\,e^{-E} \qquad \text{Eqn. 4.4}$$

Substituting n from Eqn. 3 in Eqn.4, q could be expressed in terms of engineering stress and strain as follows:

$$\sigma = K\,E^{E/q}\,e^{-E} \qquad \text{Eqn. 4.5}$$

Equations 4 and 5 were then used to generate *iso-flow* and *iso-q* lines to produce the quality charts proposed by Caceres, where the line $q = 1$ represents maximum quality while the lines $q < 1$ represent lesser quality values. Caceres correlated q with Q based on the observations that the *iso-q* lines are roughly equivalent to the *iso-Q* lines generated by Drouzy *et al.* Similarly, as the *iso-flow* lines were also observed to be practically parallel to the *iso-YS* lines, *YS* values could also be calculated and allotted to the n values

corresponding to the *iso-flow* lines. Thus, in Figure 4.17, the two sets of *iso*-lines represent *n* and *YS*, and *q* and *Q*, respectively. This relative relationship provides a physical meaning to *Q* and *YS*, as they can be described in terms of *q* or relative ductility, and *iso-flow* lines, respectively.

The quality charts shown in Figure 4.17 provide several significant properties for each point located in these charts, namely, *UTS*, elongation to fracture, *YS*, *q* and *Q*, and thus allow for the selection and prediction of the appropriate metallurgical conditions to be applied to a specific alloy to obtain the properties desired for a particular application.

In general, most of the alloys show a *Q* value of 406 MPa or less with some exceptions. As may be seen from Figure 4.17(a), Alloy C exhibits a *Q* value that approaches the 522 MPa *iso-Q* line in the peak aged condition (180°C), while other alloys such as Alloys E, F and G show *Q* values that approach 472 MPa. Yield strengths in the peak aged condition generally exhibit values higher than 327 MPa, which rapidly drop down to 107 MPa at 300°C.

It is interesting to observe that the low ductility values exhibited by Alloy D in Figure 4.15(a) lower the alloy quality as well so that its curve is shifted further to the left compared to the other alloys.

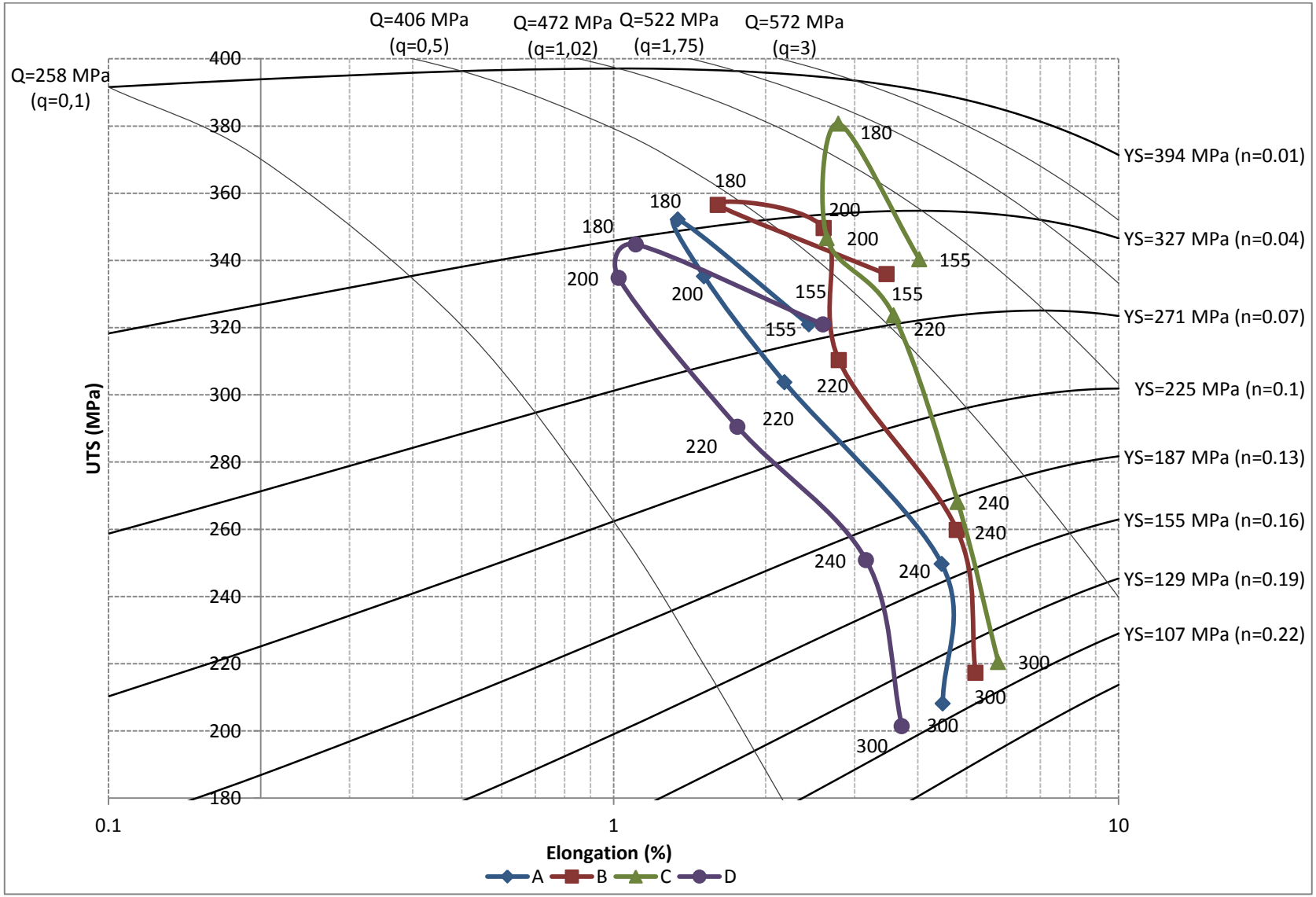
Q=258 MPa
(q=0,1)
Q=406 MPa
(q=0,5)
Q=472 MPa
(q=1,02)
Q=522 MPa
(q=1,75)
Q=572 MPa
(q=3)
YS=394 MPa (n=0.01)
YS=327 MPa (n=0.04)
YS=271 MPa (n=0.07)
YS=225 MPa (n=0.1)
YS=187 MPa (n=0.13)
YS=155 MPa (n=0.16)
YS=129 MPa (n=0.19)
YS=107 MPa (n=0.22)
UTS (MPa)
400
380
360
340
320
300
280
260
240
220
200
180
0.1
1
10
Elongation (%)
A
B
C
D

Figure 4.17 (a)

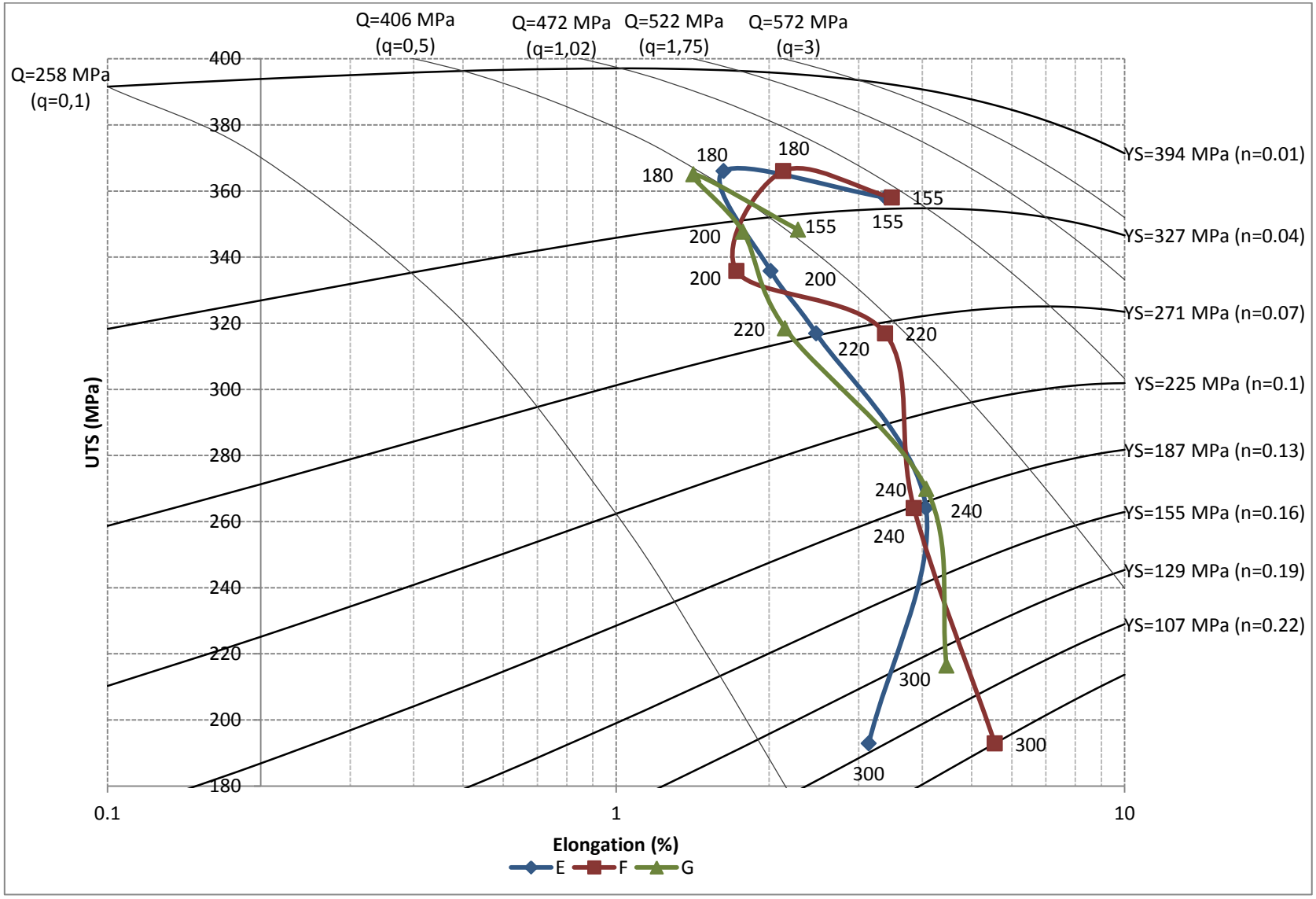
Q=406 MPa
(q=0,5)
Q=472 MPa
(q=1,02)
Q=522 MPa
(q=1,75)
Q=572 MPa
(q=3)
Q=258 MPa
(q=0,1)
YS=394 MPa (n=0.01)
YS=327 MPa (n=0.04)
YS=271 MPa (n=0.07)
YS=225 MPa (n=0.1)
YS=187 MPa (n=0.13)
YS=155 MPa (n=0.16)
YS=129 MPa (n=0.19)
YS=107 MPa (n=0.22)
UTS (MPa)
400
380
360
340
320
300
280
260
240
220
200
180
0.1
1
10
Elongation (%)
E
F
G
180
180
180
155
155
155
200
200
200
220
220
220
240
240
240
300
300
300

Figure 4.17 (b)

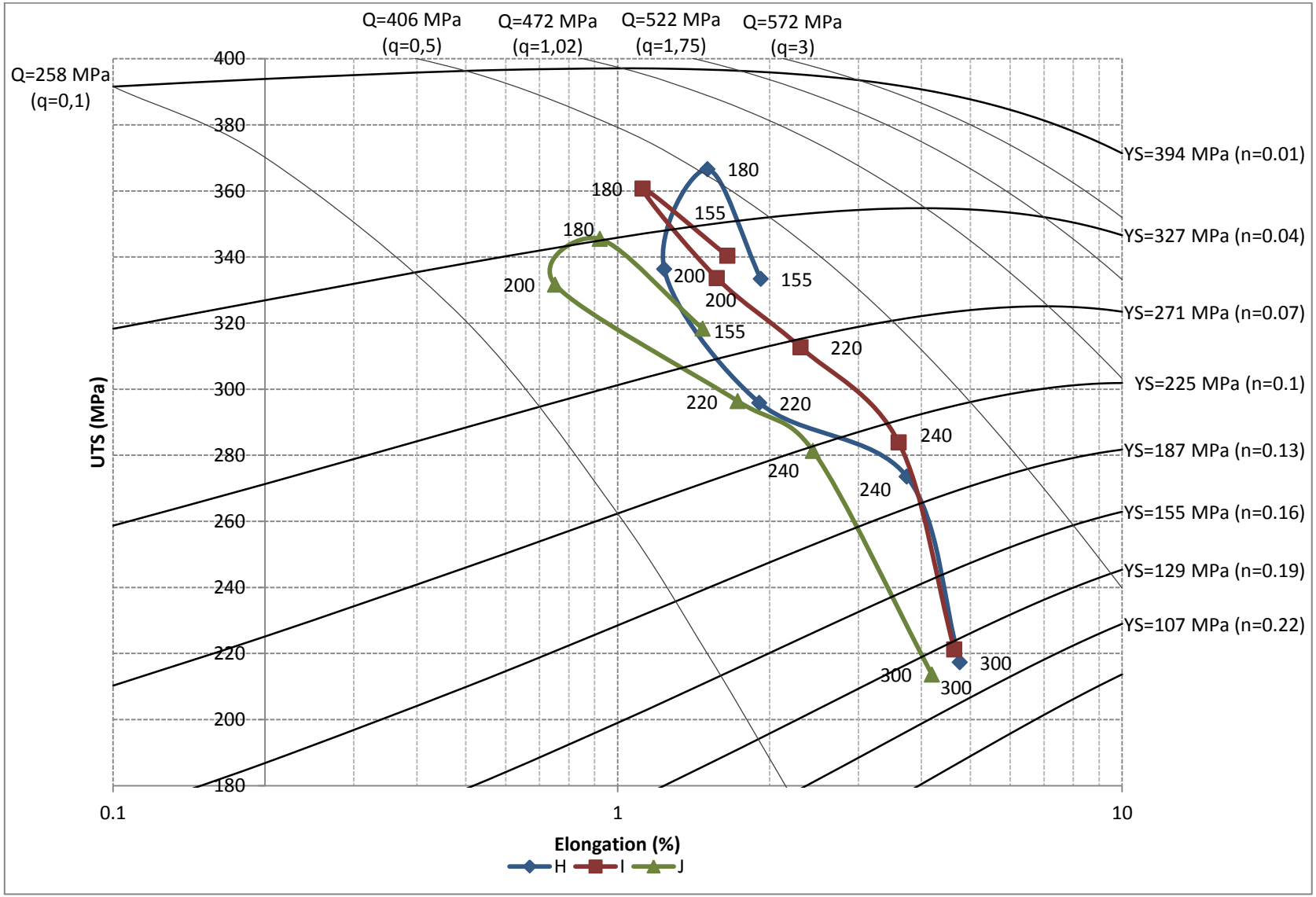
Q=406 MPa
(q=0,5)
Q=472 MPa
(q=1,02)
Q=522 MPa
(q=1,75)
Q=572 MPa
(q=3)
Q=258 MPa
(q=0,1)
YS=394 MPa (n=0.01)
YS=327 MPa (n=0.04)
YS=271 MPa (n=0.07)
YS=225 MPa (n=0.1)
YS=187 MPa (n=0.13)
YS=155 MPa (n=0.16)
YS=129 MPa (n=0.19)
YS=107 MPa (n=0.22)
UTS (MPa)
400
380
360
340
320
300
280
260
240
220
200
180
0.1
1
10
Elongation (%)
H
I
J
180
180
155
180
200
155
200
200
155
220
220
220
240
240
240
300
300
300

Figure 4.17 (c)

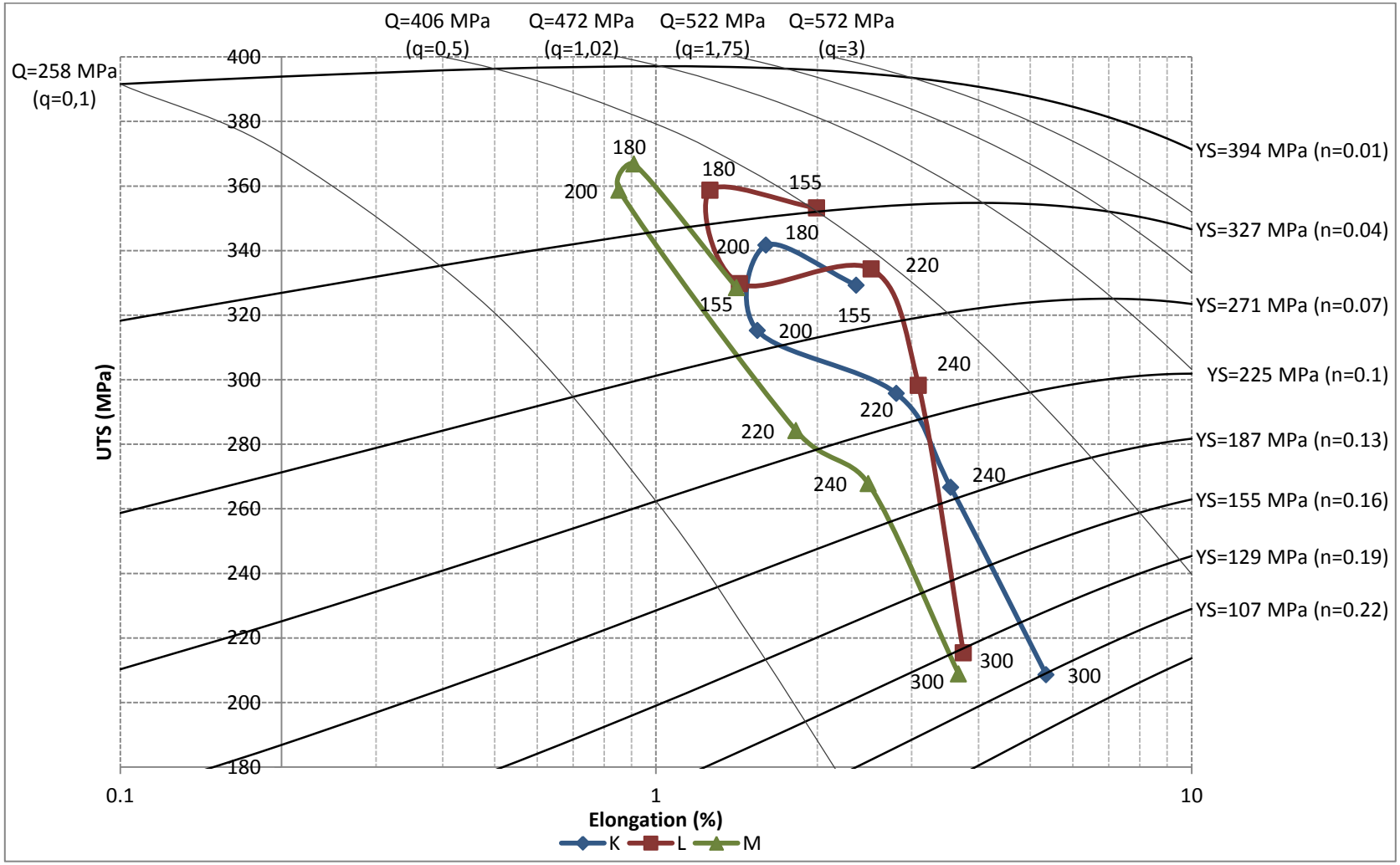

(d)

Figure 4.17 Quality charts showing the tensile properties displayed by the 220 alloy at different aging temperatures.

4.5 STATISTICAL ANALYSIS

As part of analyzing the results from the hardness and tensile tests, Minitab 16 (Minitab Inc.), a statistical software tool was used. Plots of △P were generated of the hardness, UTS, YS and percent elongation values obtained at the different aging temperatures for the thirteen 220 alloys studied, taking the base alloy A as the reference, where △P represents the difference in the value of a particular property of a specific alloy (P = property = hardness, UTS, YS, %El) and that of alloy A. This approach helped to better visualize the effects and interactions of the various additions used and the different heat treatment conditions. As will be seen from the figures presented subsequently, such △P plots instantly show how the different 220 alloys stand with respect to the reference alloy at a particular aging condition.

Figures 4.18 to 4.20 show the △P values of the 220 alloys for hardness, tensile properties and Quality index values obtained with reference to the base alloy A, represented by the 0(A) line across the aging temperature studied. As may be seen, among all the alloys, Alloy K provides the highest hardness overall. Alloys B, D and C exhibit hardness values lower than the base alloy. This is to be expected since these alloys contain only Sr and/or Ti additions. Above the 220°C, the hardness values of these alloys are improved and all alloys exhibit hardness values above that of the base alloy.

The variations in the tensile properties with respect to alloy A as shown in Figure 4.19 show that the yield strength of Alloy M is higher than the YS values of the other alloys

at most of the aging temperature, again the B, C and D alloys show YS levels below those shown by the base alloy at most aging temperature except at 240°C when all alloys show improvement in their yield strength. At this temperature, Alloy K exhibits the maximum strength (UTS and YS). In accordance with these observations, the ductility of the K alloy is reduced to that of the base alloy up to 200°C aging temperature, beyond which the ductility fluctuates from a higher to a lower and again to a higher values (approximately 1%) with respect to the base alloy. Alloy C shows the best improvement ductility that remains steady across the aging temperature range.

The variations in the quality index values observed in Figure 4.20 are controlled by the changes in tensile properties observed in Figure 4.19. In general, Alloy K shows a better alloy quality overall.

Figure 4.21 complies the strength-ductility values obtained for all the 220 alloys studied. These values fall into regions corresponding to peak aging, and underaging and overaging conditions. Using regression analysis, the UTS versus elongation relationship may be expressed as follows:

$$UTS = - (31.989) (\%Elong.) + (393.13)$$

With a fit of $R^2 = 0.8301$.

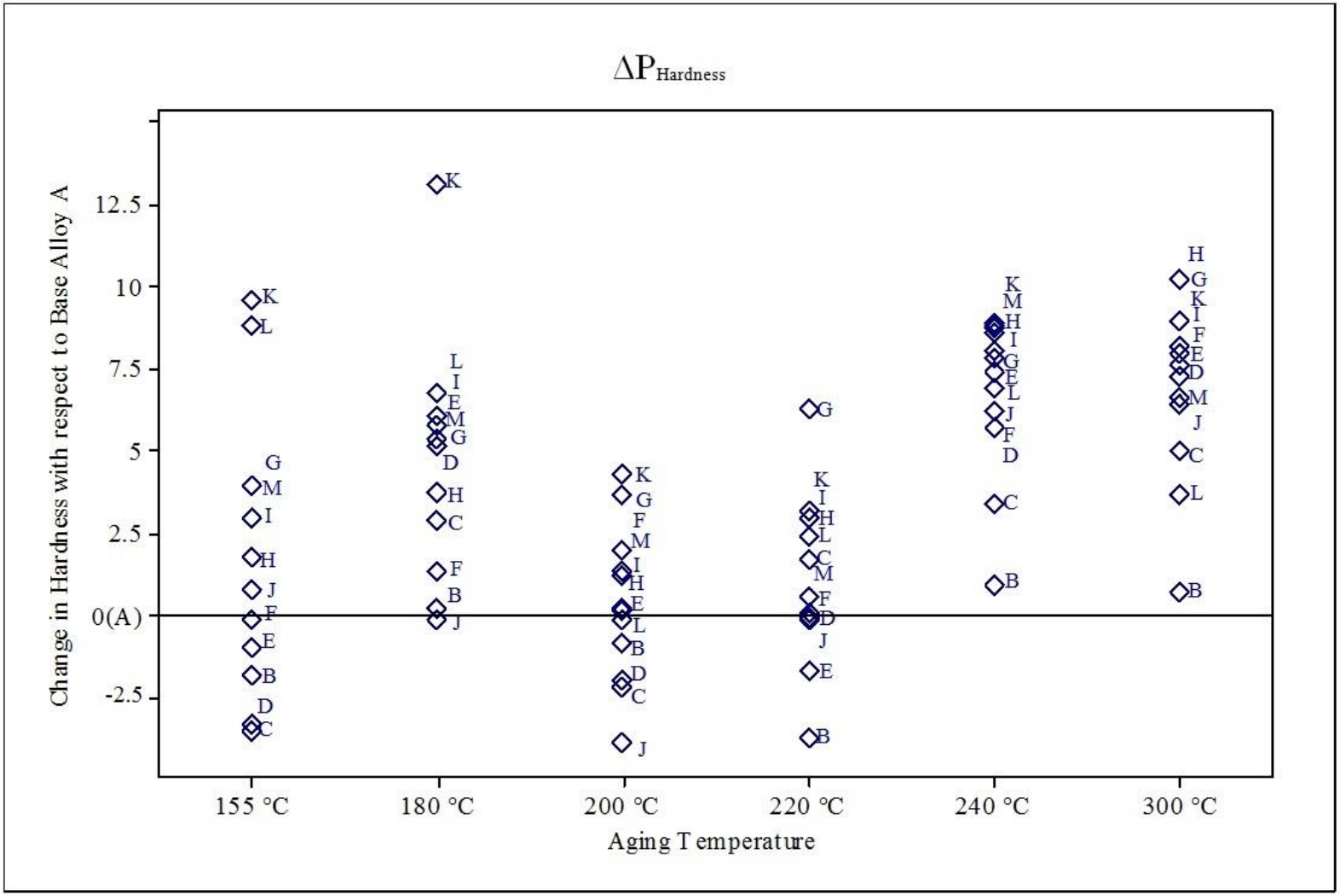

Figure 4.18 Variation in △P-Hardness as a function of aging temperature for the 220 alloys studied.

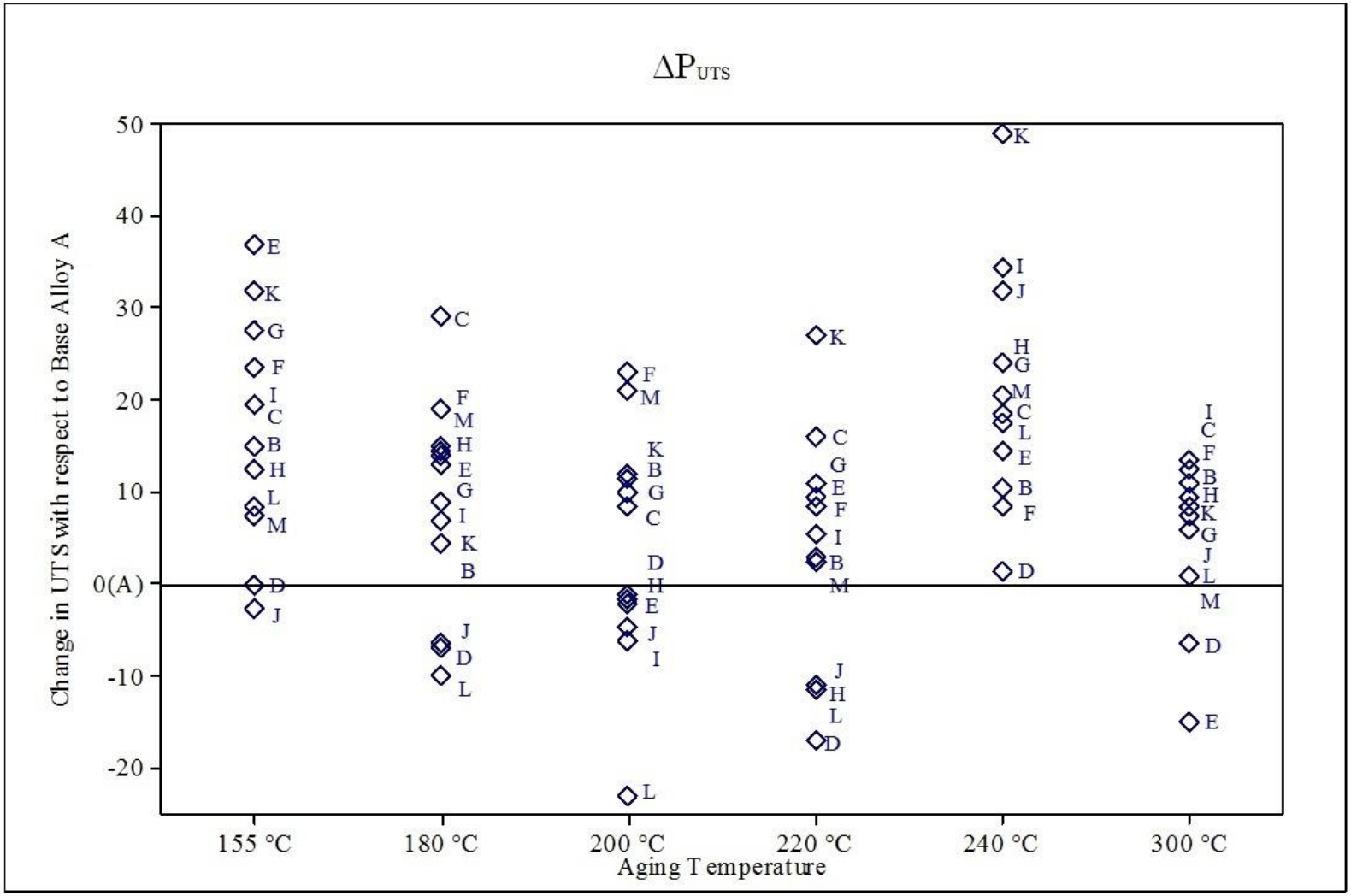
ΔP UTS
Change in UTS with respect to Base Alloy A
50
40
30
20
10
0(A)
-10
-20
155 °C
180 °C
200 °C
220 °C
240 °C
300 °C
Aging Temperature

Figure 4.19 (a)

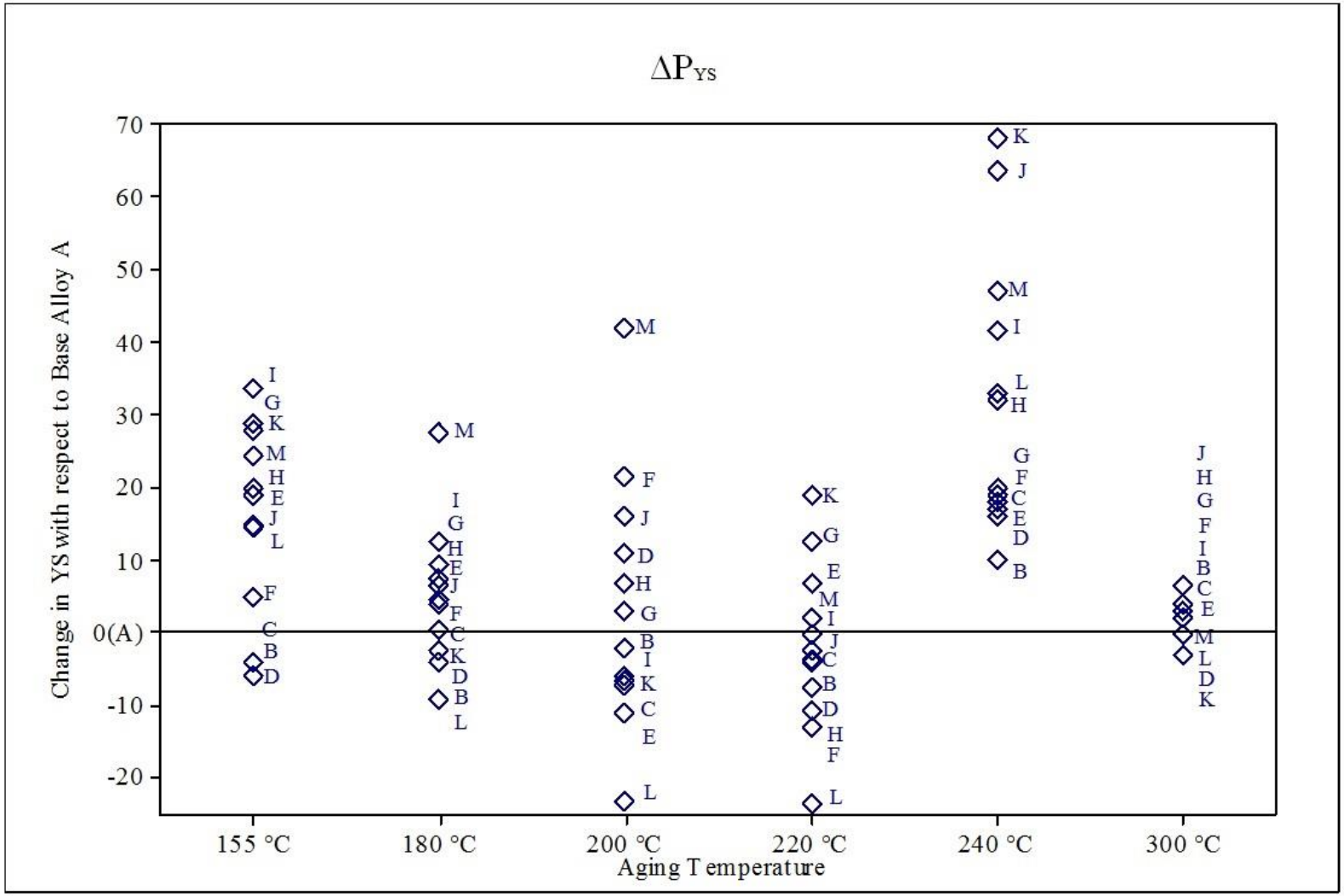
ΔPYS
Change in YS with respect to Base Alloy A
70
60
50
40
30
20
10
0(A)
-10
-20
155 °C
180 °C
200 °C
220 °C
240 °C
300 °C
Aging Temperature

Figure 4.19 (b)

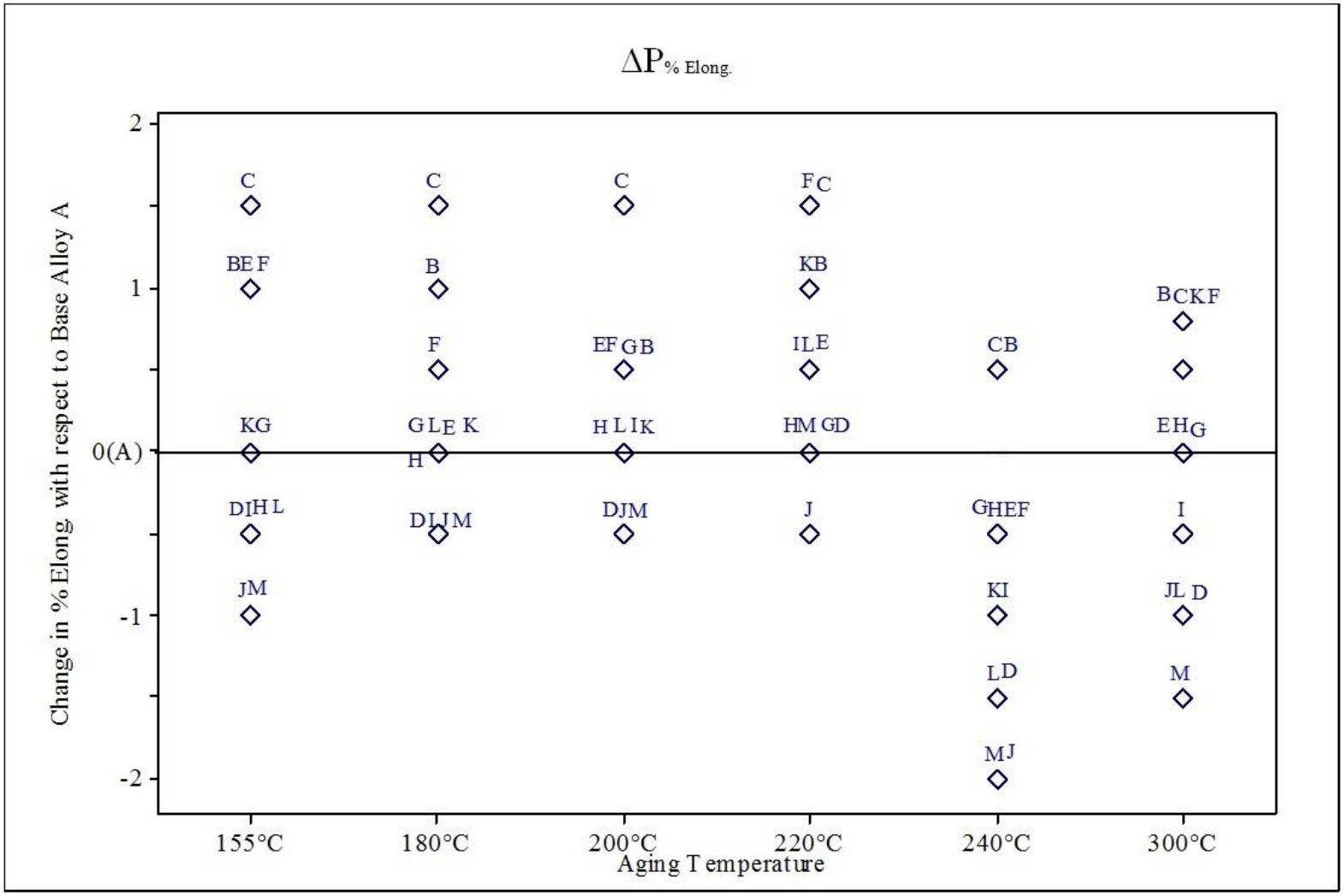

(c)

Figure 4.19 Variation in (a) △P-UTS, (b) △P-YS, and (c) △P-%Elongation as a function of aging temperature for the 220 alloys studied.

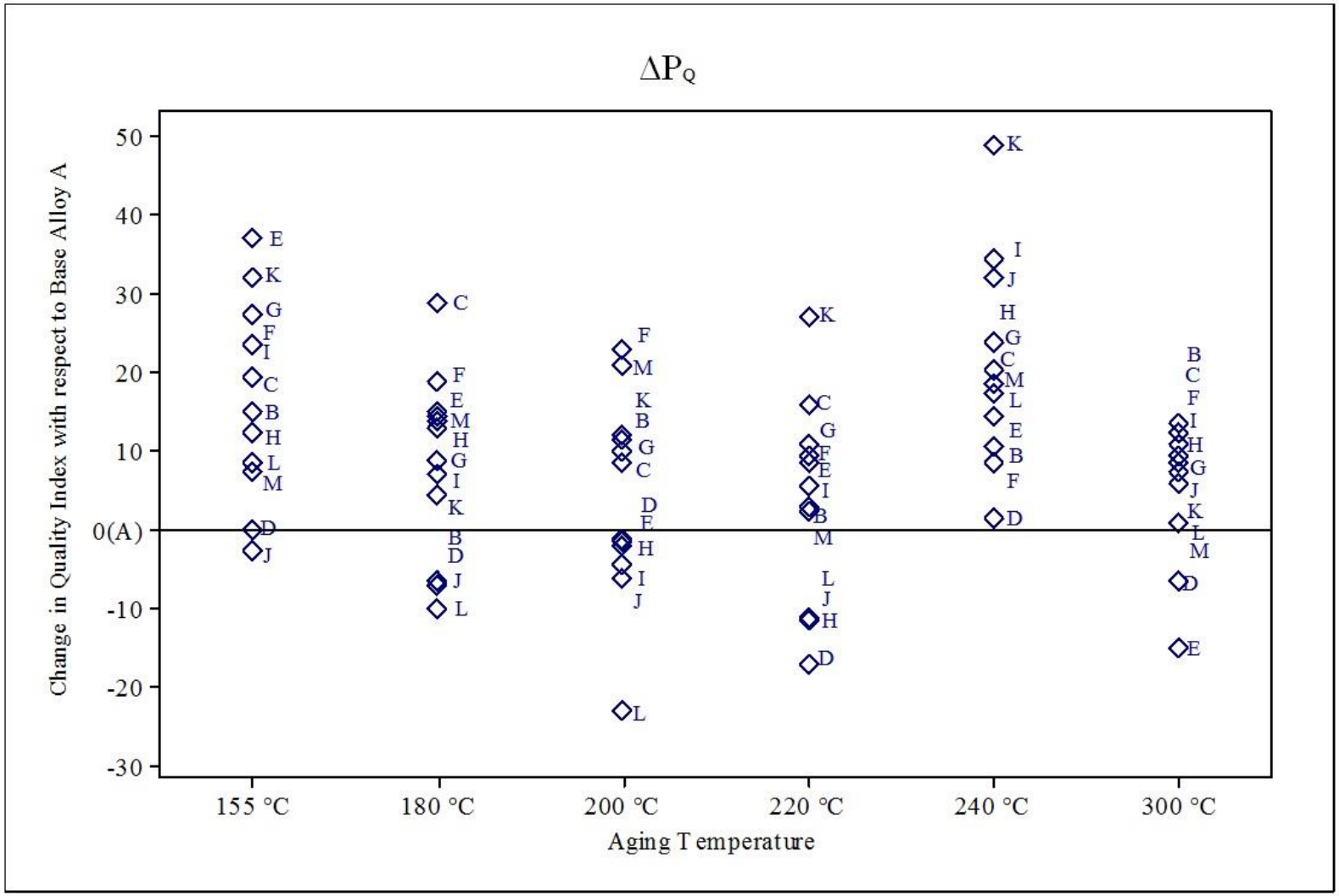

Figure 4.20 Variation in △P-Quality Index as a function of aging temperature for the 220 alloys studied.

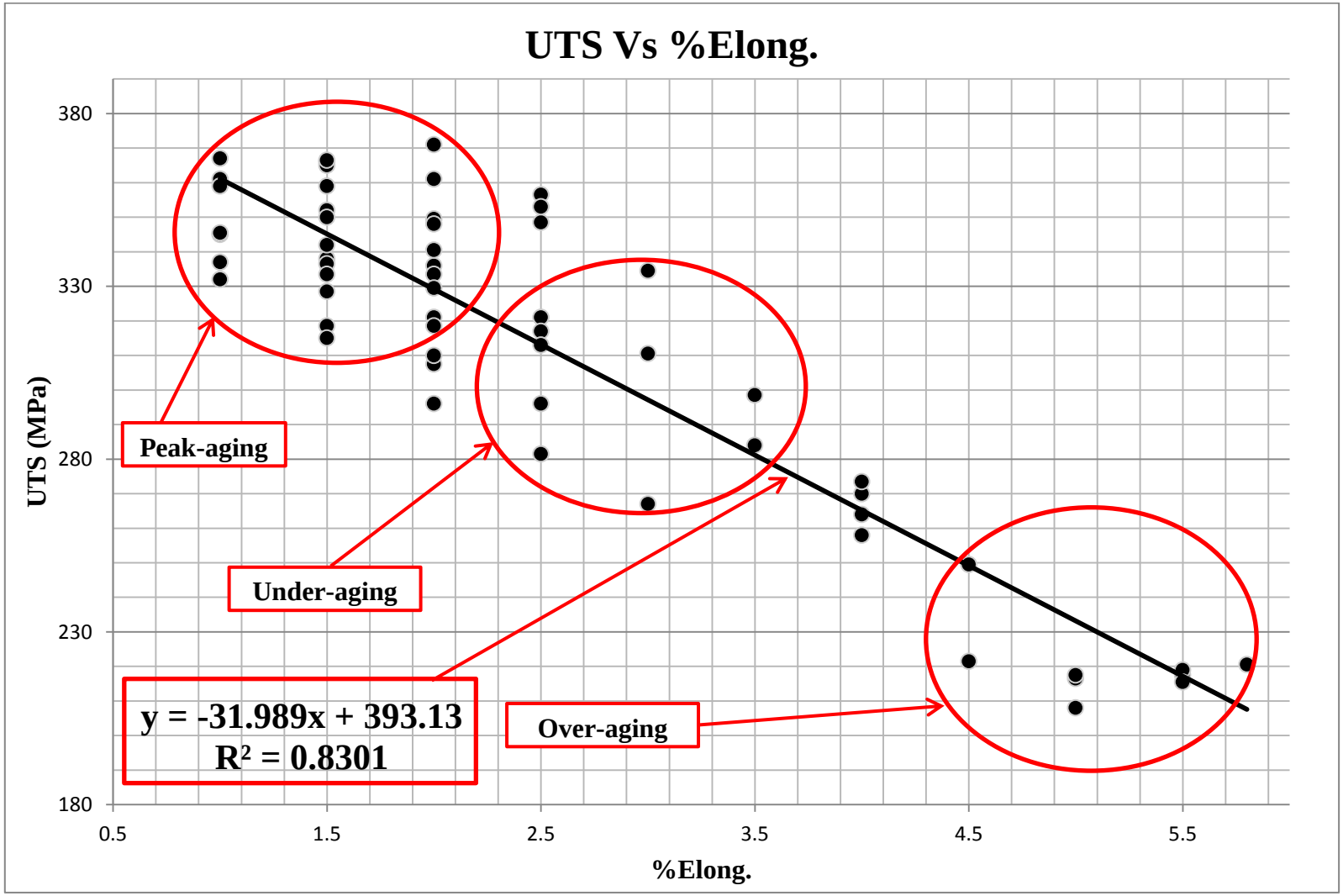

Figure 4.21 UTS Vs %Elong. for 220 alloys in age-hardened condition.

CHAPTER 5

CONCLUSIONS AND RECOMMENDATIONS

CHAPTER 5

CONCLUSIONS AND RECOMMENDATIONS

5.1 CONCLUSIONS

The present study was carried out to investigate the effects of Sr, Ti, Zr, Sc and Ag additions, individually or in combination, on the performance of an Al-2%Cu based alloy. Using different combinations/amounts of these additives, thirteen alloys were prepared (base alloy A and alloys B through M). From the microstructural observations and a statistical analysis of the hardness and tensile test data and quality charts constructed from the latter, the following conclusions may be drawn.

1. Increasing the amount of added elements increases the volume fraction of the intermetallic phases formed in the alloys which reflects on the alloy mechanical properties and quality.

2. With the exception of the Cu-rich $CuAl_2$ phase, most of these intermetallics do not dissolve upon solution heat treatment.

3. Addition of 0.15%Ti+0.30%Zr is found to be very effective in refining the grain size from 434 μm in the base alloy to 122 μm. Increasing the Zr level to 0.50% does not improve upon the refining.

4. Addition of .15%Ti+0.30%Zr+0.15%Sc, however, greatly improves the refinement, as does an individual addition of 0.50%Zr, producing grain sizes in the range of 55-75 µm.

5. The as-cast alloy hardness improves by ~18% with solution heat treatment (495°C/8h). Alloys H and M (with higher individual Zr contents) show maximum hardness. However, alloys C, F and I show maximum improvement, indicating that the addition of Ti and Zr - as 0.15%Ti alone, or in combination with Zr provides the greatest response to solution heat treatment.

6. Aging further improves the hardness to ~105 BHN. Peak hardness is observed at 180°C aging temperature.

7. The best combination for maximizing tensile strength in the as-cast alloys appears to be 0.15%Ti+0.03%Zr, followed by 0.15%Ti+0.30%Zr+0.15%Sc.

8. The UTS values improve considerably after solution heat treatment, resulting from the dissolution of the Cu-rich phase, solid solution strengthening being the main operating mechanism.

9. The yield strength values improve overall by ~8.5% after solution treatment. As yield stress is more dependent on grain size than tensile strength, the improvement in YS would be related more to grain boundary strengthening in the alloys showing reduced grain sizes.

10. The alloy ductility increases from ~2.3% to ~4.3% after solution heat treatment, with alloy B (0.02%Sr addition) exhibiting maximum ductility with an elongation of 6.8%,

attributed to the influence of Sr in the dissolution of the $CuAl_2$ phase and refining the α-Fe intermetallic phase particles.

11. Peak aging occurs mainly at 180°C, and in some cases is spread over 180°-200°C, before the onset of softening at 220°C. Alloy C shows the highest UTS at peak aging.

12. Alloys G and J show the most stability in tensile strength across the aging temperature range from 155°C to 220°C, while alloy K shows greatest resistance to softening across this range, making it a good choice for elevated temperature applications.

13. The yield strength of Alloys A, B, C and D show identical behavior over the range of aging temperatures studied, indicating that the base alloy A is not affected by Sr, Ti or Sr+Ti additions.

14. Alloy M exhibits maximum YS (346-348 MPa), showing that a high addition of Zr (0.50%), resulting in a profuse formation of Al_3Zr precipitates, greatly improves the yield strength.

15. Ductility values are reduced to below 1% at the peak aging temperature. Overall, alloy K exhibits the best ductility values across the aging temperature range studied, favoring its choice over other alloys for elevated temperature applications.

16. The variations in tensile properties in the Al-2%Cu alloys studied may be understood in terms of the contributions of different strengthening mechanisms, the grain size, the volume fraction of intermetallics produced, and the nature, evolution and growth of the hardening precipitates with respect to the aging conditions.

17. The strength-ductility relationship of the Al-2%Cu based alloys studied may be represented in the form of a linear regression equation as follows: $y = -31.98x + 393.1$, with an R^2 value of 0.830.

18. Quality charts constructed from tensile properties data may be used for the selection of the appropriate metallurgical conditions for tailoring the alloy properties to those required for a specific application.

5.2 RECOMMENDATIONS FOR FUTURE WORK

The focus of this study was on determining the mechanical properties of the Al-2%Cu based alloys. To limit the study within the time requirements of a Master's research project, aging time was not considered as a parameter in this study. Based on the results obtained in this project, it would be interesting to extend the work to investigate the effects of heat treatment in more detail and follow the precipitation behavior of the various precipitates formed using transmission electron microscopy.

REFERENCES

REFERENCES

1. C.S. Cole and A.M. Sherman, "Lightweight Materials for Automotive Applications," *Materials Characterization*, Vol. 35(1), 1995, pp. 3-9.
2. W.S. Miller, L. Zhuang, J. Botterna, A.J. Wittebrood, P. De Smet, A. Haszler and A. Vieregge, "Recent Development in Aluminum Alloys for the Automotive Industry," *Materials Science and Engineering A*, Vol. 280, 2000, pp. 37-49.
3. F. Palazzo, "The Future of Aluminum in the Automotive Industry," *Aluminio*, Vol. 46(9), 1977, pp. 323-334.
4. ASM Handbook, Powder Metal Technologies and Applications: Advanced Aluminum Powder Metallurgy Alloys and Composites, R. B. Bhagat, ASM International, Materials Park, OH, Vol. 7, 10th Edition, 1998, pp. 820-859.
5. A.T. Spada, "In Search of Lightweight Components: Automotive Cast Aluminum Conversion," *Engineered Casting Solutions*, Vol. 4(2), 2002, pp. 28-31.
6. J.P. Immarigeon, R.T. Holt, A.K. Koul, L. Zhao, W. Wallace and J.C. Beddoes, "Lightweight Materials for Aircraft Applications," *Materials Characterization*, Vol. 35(1), 1995, pp. 41-67.
7. I.N. Fridlyander, "Aluminum Alloys in Aircraft in the Periods of 1970-2000 and 2001-2015," *Metal Science and Heat Treatment*, Vol. 43(1-2), 2001, pp. 6-10.

8. G.E. Totten and D.S. MacKenzie (Eds.), *Handbook of Aluminum, Vol. 1: Physical Metallurgy and Process*, Marcel Dekker Inc., New York, 2003, pp. 114-168.

9. A.M. Samuel, F.H. Samuel and H.W. Doty, "Observations on the Formation of β-Al_5FeSi Phase in 319 Type Al-Si Alloys," *Journal of Materials Science*, Vol. 31(20), 1996, pp. 5529-5539.

10. J. Espinoza-Cuadra, P. Gallegos-Acevedo, H. Mancha-Molinar and A. Picado, "Effect of Sr and Solidification Conditions on Characteristics of Intermetallic in Al-Si 319 Industrial Alloys," *Materials and Design*, Vol. 31(1), 2010, pp. 343-356.

11. S.G. Shabestari and J.E. Gruzleski, "Modification of Iron Containing Precipitates in $AlSi_2$ Alloys with Strontium," *Giesserei-Praxis*, Vol. 17, 1997, pp. 385-394.

12. L. Reich, M. Murayama and K. Hono, "Evolution of Ω Phase in an Al-Cu-Mg-Ag Alloy-A Three-Dimensional Atom Probe Study," *Acta Materialia*, Vol. 46, 1998, pp. 6053-6062.

13. B.M. Gable, G.J. Shiflet and E.A. Starke, "Alloy Development for the Enhanced Stability of Q Precipitates in Al-Cu-Mg-Ag Alloys," *Metallurgical and Materials Transactions A*, Vol. 37A, 2006, pp. 1091-1105.

14. A.K. Mukhopadhyay, G. Eggeler and B. Skrotzki, "Nucleation of θ Phase in an Al-Cu-Mg-Mn-Ag Alloy Aged at Temperatures Below 200°C," *Scripta Materialia*, Vol. 44, 2001, pp. 545-551.

15. N. Ryum, "Precipitation and Recrystallization in an Al-0.5wt Percent Zr Alloy," *Acta Metallurgica*, Vol. 17, 1969, pp. 269-278.

16. S. Rystad and R. Ryum, "A Metallographical Investigation of the Precipitation and Recrystallization Process in an Al-Zr Alloy," *Aluminium*, Vol. 53(3), 1977, pp. 193-195.

17. J.G. Kaufman, "Introduction to Aluminum Alloys and Tempers: Surface Treatments and Coatings," *Materials Park*, OH: ASM International, 2000, p. 25.

18. I.J. Polmear, *Light Alloys: Metallurgy of the Light Metals*, 3rd Edition, Hodder & Arnold, London, 1995, pp. 4-28.

19. J.R. Davis, *ASM Speciality Handbook: Aluminum and Aluminum Alloys*, ASM International, Materials Park, OH, 1993. pp. 3-6.

20. J.R. Davis, *Aluminum and Aluminum Alloys*, Metals Park, Ohio, 1994, p. 547.

21. G.E. Totten and D.S. Mackenzie (Eds.), *Handbook of Aluminum, Vol. 1: Physical Metallurgy and Process,* Marcel Dekker Inc., New York, 2003, p. 1296.

22. H. Sehitoglu, T. Foglesong and H.J. Maier, "Precipitation Effects on the Mechanical Behaviour of Aluminum Copper Alloys: Part I. Experiments," *Metallurgical and Materials Transactions A*, Vol. 36A, 2005, pp. 749-761.

23. R.N. Lumley, J. Bufaa, I.J. Polmear, A.J. Morton and A.G. Crosky, "Secondary Precipitation in Aluminum Alloys and Its Role in Modern Heat Treatment," *Materials Science Forum*, Vol. 519, 2006, pp. 283-290.

24. J.E. Hatch, *Aluminum: Properties and Physical Metallurgy,* American Society for Metals, Materials Park, OH, 1984, p. 135.

25. *ASM Handbook, Properties and Selection: Nonferrous Alloys and Special-Purpose Materials,* L.A. Abel, R.T. Kiepura, P. Thomas, H.F. Lampman and N.D. Wheaton (Eds.), ASM International, Materials Park, OH, Vol. 2, 1990, p. 1328.

26. D. Askeland, P. Fulay and W. Wright, *The Science and Engineering of Materials,* 6th Edition, Cengage Learning (Pub.), Stamford, 2011, pp. 458-484.

27. J. Gauthier, P.R. Louchez and F.H. Samuel, "Heat Treatment of 319.2 Aluminum Automotive Alloy: Part 2, Aging Behaviour," *Cast Metals,* Vol. 8, 1995, pp. 108-114.

28. N. Crowell and S. Shivkumar, "Solution Treatment Effects in Cast Al-Si-Cu Alloys," *AFS Transactions,* Vol. 103, 1995, pp. 721-726.

29. D. Apelian, S. Shivkumar and G. Sigworth, "Fundamental Aspects of Heat Treatment of Cast Al-Si-Mg Alloys," *AFS Transactions,* Vol. 137, 1989, pp. 727-742.

30. D.L. Zhang and L. Zheng, "The Quench Sensitivity of Cast Al-7 Wt Pct Si-0.4 Wt Pct Mg Alloy", *Metallurgical and Materials Transactions A,* Vol. 27A, 1996, pp. 3983-3991.

31. W. Reif, S. Yu, J. Dutkiewicz, R. Ciach and J. Krol, "Pre-Ageing of AlSiCuMg Alloys in Relation to Structure and Mechanical Properties," *Materials and Design,* Vol. 18(4), 1997, pp. 253-256.

32. R.K. Mishra, G.W. Smith, W.J. Baxter, A.K. Sachdev and V. Franetovic, "The Sequence of Precipitation in 339 Aluminum Castings," *Journal of Materials Science,* Vol. 36(2), 2001, pp. 461-468.

33. G.E. Dieter, *Mechanical Metallurgy*, SI Metric Edition, McGraw-Hill, London, UK, 1988, pp. 62-114.

34. http://www.cmse.ed.ac.uk, Non-ferrous Alloys and Al-alloys, J. Blackford.

35. A.J. Ardel, "Precipitation Hardening", *Metallurgical Transactions A*, Vol. 16A, 1985, pp. 2132-65.

36. S. Kumai, "Hardness Characteristics in Aged Particulate", *Scripta Metallurgica et Materialia*, Vol. 27, 1992, pp. 107-110.

37. A.D. Porter and K.E. Easterling, *Phase Transformations in Metals and Alloys*, Van Nostrand Reinhold, Berkshire, England, 1981.

38. J.D. Verhoeven, *Fundamentals of Physical Metallurgy*, J. Wiley and Sons, New York, 1975.

39. W.F. Smith, Structure and Properties of Engineering Alloys, McGraw-Hill, New York, 1981.

40. M.A. van Huis, J.H. Chen, M.H.F. Sluiter and H.W. Zandbergen, "Phase Stability and Structural Features of Matrix-embedded Hardening Precipitates in Al–Mg–Si Alloys in The Early Stages of Evolution," *Acta Materialia*, Vol. 55, 2007, pp. 2183-2199.

41. R. Vissers, M.A. van Huis, J. Jansen, H.W. Zandbergen, C.D. Marioara and S.J. Andersen," The Crystal Structure of The β′ Phase in Al–Mg–Si Alloys," *Acta Materialia*, Vol. 55, 2007, pp. 3815-3823.

42. X. Wang, S. Esmaeili and D.J. Lloyd, *Metallurgical and Materials Transactions A*, Vol. 37A, 2006, pp. 2691-2699.

43. D.G. Eskin and L. Katgemian, "A Quest for a New Hot Tearing Criterion," *Metallurgical and Materials Transactions A*, Vol. 38A, 2007, pp. 1511-1519.

44. P.H. Jennings, A.R.E Singer and W.I. Pumphrey, "Hot Shortness of Some High-purity Alloys in The Systems Aluminum-Coper-Silicon and Aluminum-Magnesium-Silicon," *the Journal of Institute of Metals*, Vol. 74, 1948, pp. 15-52.

45. W.S. Pellini, "Strain theory of hot tearing," *The Foundry*, Vol. 80, 1952, pp. 125-199.

46. H.F. Bishop, C.G. Ackerlind and W.S. Pellini, "Metallurgy and mechanics of hot tearing," *Transactions of the American Foundrymen's Society*, Vol. 60, 1952, pp. 818-833.

47. S. Li, "Hot Tearing in Cast Aluminum Alloys: Measures and Effects of Process Variables," PhD Thesis, Worcester Polytechnic Institute, USA, 2010, p. 43.

48. N.A. Belov, A.N. Alabin, D.G. Eskin and V.V. Istomin-Kastrovskii, "Optimization of Hardening of Al-Zr-Sc Cast Alloys," *Journal of Materials Science,* Vol. 41, 2006, pp. 5890-5899.

49. D. Srinivasan and K. Chattopadhyay, "Non-equilibrium Transformations Involving LI_2-Al_3Zr in Ternary Al-X-Zr Alloys," *Metallurgical and Materials Transactions A*, Vol. 36A, 2005, pp. 311-320.

50. http://www.himikatus.ru, Aluminum Alloys Binary Phase Diagrams.

51. K.E. Knipling, "Development of a nanoscale precipitation-strengthened creep resistant aluminum alloy containing trialuminide precipitates," Ph.D. Thesis, Northwestern University, Evanston, IL, 2006, pp. 9-15.

52. B. Forbord, H. Hallem and K. Martbinsen, "The Effect of Alloying Elements on Precipitation and Recrystallisation in Al-Zr Alloys," *Proceedings of the 9th International Conference on Aluminum Alloys*, Brisbane, Australia, 2004, pp. 1179-1185.

53. Z. Jia and G. Hu, "Effect of Homogenization and Alloying Elements on Resistance of Al-Zr-Mn Alloys," *Materials Science and Engineering A*, Vol. 444A, 2007, pp. 284-290.

54. P. Sepehrband, R. Mahmudi and F. Khomamizadeh, "Effect of Zr Addition on the Aging Behavior of A319 Aluminum Cast Alloy," *Scripta Materialia*, Vol. 52, 2005, pp. 253-257.

55. J.D. Robson and P.B. Prangnell, "Dispersoid Precipitation and Process Modelling in Zirconium Containing Commercial Aluminum Alloys," *Acta Materialia*, Vol. 49, 2001, pp. 599-613.

56. J.D. Robson, "Optimizing the Homogenization of Zirconium Containing Commercial Aluminum Alloys Using a Novel Process Model," *Materials Science and Engineering A*, Vol. 338A, 2002, pp. 219-229.

57. N.A. Belov, D.G. Eskin and A.A. Aksenov, *Multicomponent Phase Diagrams: Application for Commercial Aluminum Alloys*, Elsevier, Boston, 2005, p. 413.

58. L.S. Toropova, D.G. Eskin, M.L. Kharaktrova and T.V. Dobakina, *Advanced Aluminum Alloys Containing Scandium: Structure and Properties*, Gordon and Breach Science Publishers, Canada, 1998, p. 175.

59. D.N. Seidman, E.A. Marquis and D.C. Dunand, "Precipitation Strengthening at Ambient and Elevated Temperatures of Heat-Treatable Al(Sc) Alloys," *Acta Materialia,* Vol. 50, 2002, pp. 4021-4035.

60. V.G. Davydov, T.D. Rostova and V.I. Yelagin, "Scientific Principles of Making an Alloying Addition of Scandium to Aluminum Alloys," *Materials Science and Engineering A*, Vol. 280A, 2000, pp. 30-36.

61. S. Iwamura and Y. Miura, "Loss in Coherency and Coarsening Behaviour of Al_3Sc Precipitates," *Acta Materialia*, Vol. 52, 2004, pp. 591-600.

62. E.A. Marquis and D.N. Seidman, "Nanoscale Structural Evolution of Al_3Sc Precipitates in Al(Sc) Alloys," *Acta Materialia*, Vol. 49, 2001, pp. 1909-1919.

63. V.V. Zakharov, "Effect of Scandium on the Structure and Properties of Aluminum Alloys," *Metal Science and Heat Treatment*, Vol. 45, 2003, pp. 246-253.

64. K.B. Hyde, A.F. Norman and P.B. Prangnell, "The Effect of Cooling Rate on the Morphology of Primary Al_3Sc Intermetallic Particles in Al-Sc Alloy," *Acta Materialia,* Vol. 49, 2001, pp. 1327-1337.

65. O.N. Senkov, M.R. Shagiev, S.V. Senkova and D.B. Miracle, "Precipitation of Al_3(Sc,Zr) Particles in an Al-Zn-Mg-Cu-Sc-Zr Alloy during Conventional Heat Treatment and its Effect on Tensile Properties," *Acta Materialia*, Vol. 56, 2008, pp. 3723-3738.

66. C.B. Fuller, J.L. Murray and D.N. Seidman, "Temporal Evolution of the Nanostructure of Al(Sc,Zr) Alloys: Part I-Chemical Compositions of $Al_3(Sc_{1-x}\ Zr_x)$ Precipitates," *Acta Materialia*, Vol. 53, 2005, pp. 5401-5413.

67. E. Clouet, M. Nastar, A. Barbu, C. Sigli and G. Martin, "Precipitation in Al-Zr-Sc Alloys: a Comparison between Kinetic Monte Carlo, Cluster Dynamics and Classical Nucleation Theory," in *Solid-Solid Phase Transformations in Inorganic Materials*, The Minerals, Metals & Materials Society, Warrendale, PA, 2005, pp. 1-21.

68. B. Forbord, W. Lefebvre, F. Danoix, H. Haliem and K. Marthinsen, "Three Dimensional Atom Probe Investigation on the Formation of Al_3(Sc,Zr)-Dispersoids in Aluminum Alloys," *Acta Materialia*, Vol. 51, 2004, pp. 333-337.

69. Z. Ahmad, "The Properties and Application of Scandium-Reinforced Aluminum," *JOM*, Vol. 55, 2003, pp. 35-37.

70. http://www.calphad.com, Aluminum Alloys and Alloying Elements, Computational Thermodynamics Inc. Consultant Business.

71. A. Garg, Y.C. Chang and J.M. Howe, "Precipitation of the Omega Phase in an Al-4.0Cu-0.5Mg Alloy," *Scripta Metallugica et Materialia,* Vol. 24(4), 1990, pp. 677-680.

72. I.J. Polmear, "The Effects of Small Additions of Silver on the Ageing of Some Aluminium Alloys," *Transactions of Metals Society,* Vol. A230, 1964, pp. 1331-1339.

73. K. Matsuda, K. Fukaya, Z. Young, T. Kawabata, Y. Uetani and S. Ikeno, "Effect of Copper, Silver and Gold on Tensile Behavior in Al-Mg-Si Alloy," *Materials Forum*, Vol. 28, 2004, pp. 424-428.

74. R.X. Li, R.D. Li, Y.H. Zhao, L.Z. He, C.X. Li, H.R. Guan and Z.Q. Hu, "Age-Hardening Behavior of Cast Al-Si Base Alloy," *Materials Letters*, Vol. 58(15), 2004, pp. 2096-2101.

75. J. Gobrecht, "Ségrégation par Gravité du Fer, du Manganèse et du Chrome dans les Alliages Al-Si de Fonderie," *Fonderie*, No. 367, 1977, pp. 171-173.

76. J.L. Jorstad, Understanding "Sludge", *Die Casting Engineer*, Nov-Dec 1986, pp. 30-36.

77. M. Drouzy, S. Jacob and M. Richard, "Interpretation of Tensile Results by Means of Quality Index and Probable Yield Strength," *AFS International Cast Metals Journal*, Vol. 5, 1980, pp. 43-50.

78. S. Jacob, "Quality Index in Predicting of Properties of Aluminum Castings-A Review," *AFS Transactions*, Vol. 108, 2000, pp. 811-818.

79. C.H. Câceres, "A Rationale for the Quality Index of AI-Si-Mg Casting Alloys," *International Journal of Cast Metals Research*, Vol. 10, 1998, pp. 293-299.

80. C.H. Câceres, "A Phenomenological Approach to the Quality Index of AI-Si-Mg Casting Alloys," *International Journal of Cast Metals Research*, Vol. 12, 2000, pp. 367-375.

81. J.R. Davis, *Tensile Testing,* 2nd Edition, ASM International, Materials Park, OH, U.S.A., 2004.

82. S. Storen, "Understanding Aluminium as a Material," TALAT Lecture 2101, The Norwegian Institute of Technology, Trondheim and by Skanaluminium, Oslo, 1994, p. 12.

83. M.M. Makhlouf, D. Apelian and L. Wang, "Microstructure and Properties of Aluminum Die Casting Alloys," *NADCA Transactions*, Paper No. DOE/ID/13320-2, 1998, pp. 16-132.

84. Y.L. Chu, P.S. Cheng and R. Shivpuri, "Soldering Phenomenon in Aluminum Die Casting: Possible Causes and Cures", *NADCA Transactions,* Paper No. T93–124, 1993, pp. 361-371.

85. Y.L. Chu, P.S. Cheng and R. Shivpuri, "A Study of Erosive Wear in Die Casting Dies: Surface Treatments and Coatings", *NADCA Transactions,* Paper No. Cleveland-T93-073, 1993, pp. 199-208.

86. R. Shivpuri, S.I. Chang, Y.I. Chu and M. Kuthirakulathu, "An Evaluation of H-13 Die Steel, Surface Treatments and Coatings for Wear in Die Casting Dies", *NADCA Transactions,* Paper No. Detroit-T91-OC3, 1991, pp. 391-397.

87. F. Bonollo, J. Urban, B. Bonatto and M. Botter, "Gravity and low pressure die casting of aluminium alloys: a technical & economical benchmark," *La Metallurgia Italiana*, Vol. 97(6), 2005, pp. 23-25.

88. A.C. Street, *The Die Casting Book,* 2nd Edition, Portcullis Press, Red Hill, England, 1990, pp. 611-658.

89. *ASM Metals Handbook*: *Casting*, Vol. 9(15), 2008, ASM - Metals Park, Ohio, pp. 52-189.

90. J. Campbell and R.A. Harding, "The Freezing of Castings", TALAT Lecture 3204, The University of Birmingham, England, 1994, pp. 7-22.

91. J. Campbell, *Castings*, Butterworth, Oxford, 1991.

92. A. Perrone, F. Bonollo and V. Wagner, *Aluminio Magazine*, Vol. 6, 1998, pp. 32-41.

93. S. Schleg and D.P. Kanicki, "Guide to casting and moulding processes", *Engineered casting solutions*, Technical articles, Vol. 2(3), 2000, pp. 9-15.

94. J.R. Brown, *Non-Ferrous Foundryman's Handbook*, Butterworth, Oxford, 1999.

95. G.S. Cole and A.M. Sherman, "Materials Characterization," *Metallography*, Vol. 35, 1995, pp. 3-9.

96. F. Bonollo and S. Odorizzi, "*Numerical Simulation of Foundry Processes*," Servizi Grafici Editoriali, Padova, Italy, 2001.

97. http://www.gordonengland.co.uk/hardness/brinell.htm, The Brinell Hardness Test Method and The Brinell Hardness Number Calculator, Gordon England Thermal Spray Coating Consultant Business.

98. H.-L. Zhao, J.-S. Yue, Y. Gao and K. R. Weng, "Grain and dendrite refinement of A356 alloy with Al-Ti-C-RE master alloy," *Rare Metals*, Vol. 32(1), 2013, pp. 12-17.

99. C. Villeneuve and F. H. Samuel, "Fragmentation and dissolution of beta-Al_5FeSi phase during solution heat treatment of Al-13wt%Si-Fe alloys," *International Journal of Cast Metals Research*, Vol. 12(3), 1999, pp. 145-160.

100. S. Seifeddine and I. L. Svensson, "The Influence of Fe and Mn Content and Cooling Rate on The Microstructure and Mechanical Properties of A380-Die Casting Alloys," *Metallurgical Science and Technology*, Vol. 27(1), 2009, pp. 11-20.

101. W. D. Callister, *Fundamentals of Materials Science and Engineering*, 2nd edition, J. Wiley and sons, p. 252.

102. D. G. Eskin, "Decomposition of Supersaturated Solid Solution in Al-Cu-Mg-Si Alloys," *Journal of Materials Science*, 2003, Vol. 38, pp. 279-290.

103. E. M. Elgallad, " Effect of Additives on the Mechanical Properties and Machinability of a New Aluminum-Copper Base Alloy," PhD Thesis, Université du Québec à Chicoutimi, Chicoutimi, Quebec, Canada, June2010.

104. H. Liao, Y. Sun and G. Sun, "Effect of Al-5Ti-1B on the microstructure of Near-Eutectic Al-13%Si Alloys Modified with Sr," *Materials Science*, Vol. 37, 2002, pp. 3489-3495.

105. K. Yu, W. Li, S. Li and J. Zhao, "Mechanical Properties and Microstructure of Aluminum Alloy 2618 with $Al_3(Sc,Zr)$ Phases," *Materials Science and Engineering A*, Vol. A368, 2004, pp. 88-93.

106. C.N.J. Tite and P.J. Gregson, "Further Precipitation Reactions Associated with S' in Al-Li-Cu-Mg-Zr Alloys," *Scripta Metallurgica*, Vol. 22, 1988, pp. 1005-1010.

107. S. Qzbilen and H.M. Flower, “Zirconium-Vacancy Binding and Its Influence on S'-Precipitation in an Al-Cu-Mg Alloy,” *Acta Metallurgica*, Vol. 37, 1989, pp. 2993-3000.

108. G.E. Dieter, *Mechanical Metallurgy*, Third Ed., McGraw-Hill, Boston, 1986.

109. R. Mahmudi, P. Sepehrband and H.M. Ghasemi, “Improved properties of A319 aluminum casting alloy modified with Zr,” *Materials Letters*, Vol. 60, 2006, pp. 2606-2610.